SUPERCONDUCTING CIRCUITS WITH METALLIC AND SEMICONDUCTING WEAK-LINKS

ANDREA IORIO

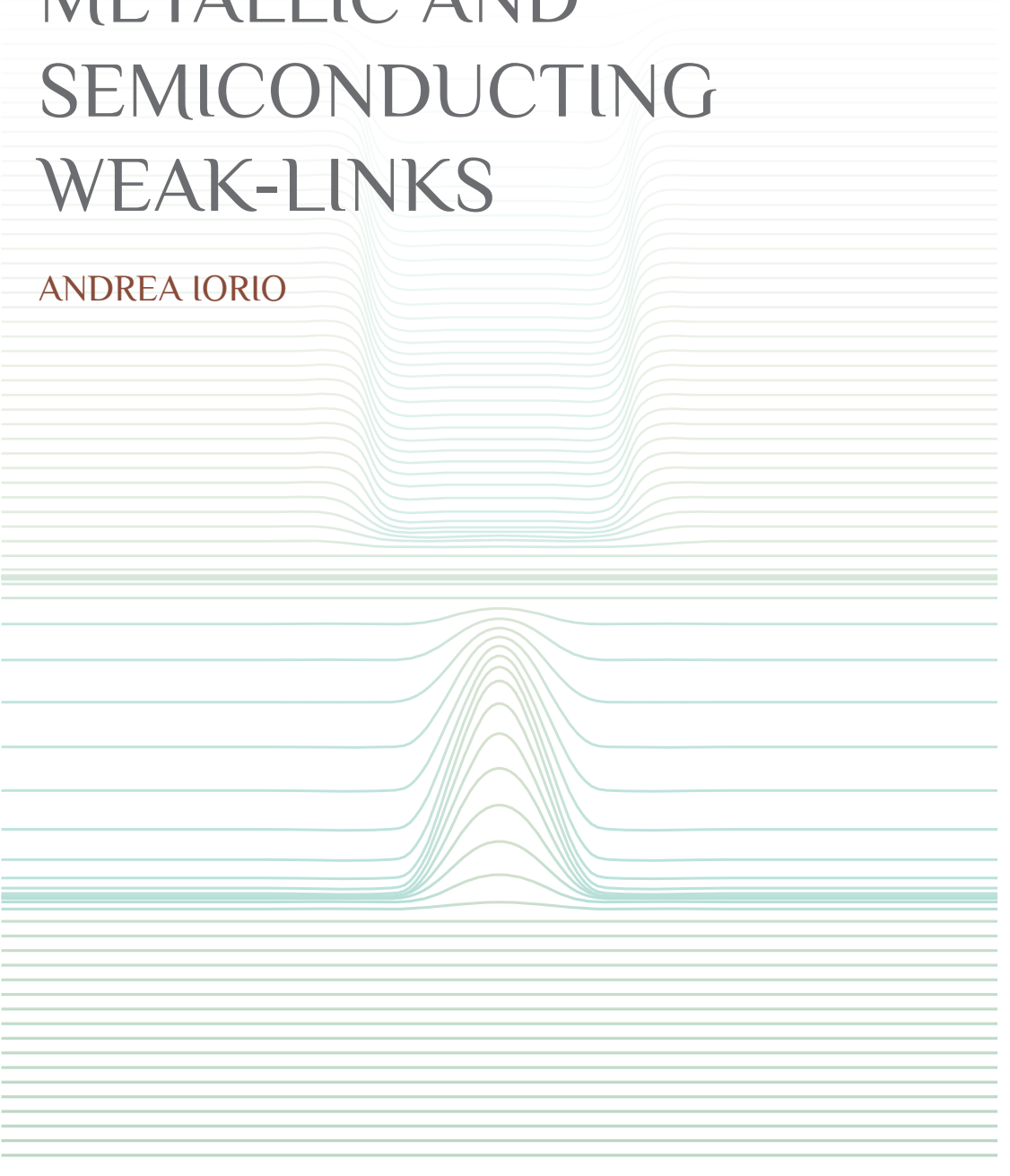

SCUOLA
NORMALE
SUPERIORE

Faculty of Sciences
PhD in Nanoscience

Superconducting circuits with metallic and semiconducting weak-links

A thesis presented for the degree of
Doctor of Philosophy

by

Andrea Iorio

Advisors:

Dott. Francesco Giazotto
Dott. Elia Strambini

Prof. Fabio Beltram

Academic Year 2022/2023
XXXIV cycle, SSD FIS/03
Scuola Normale Superiore

Contents

Acknowledgments

Completing this PhD thesis has been a challenging but rewarding journey, and I could not have done it without the support and guidance of many people who have helped me along the way. I would like to express my deepest gratitude to them all.

First and foremost, I would like to express my appreciation to my supervisor, Dr. Francesco Giazotto, for his invaluable advice, encouragement, and inspiration. He gave me the independence, responsibility, and freedom to explore research without compromise.

I am also indebted to Elia Strambini, who has been my experimental physics father, teaching me to never seek easy explanations and encouraging me to overcome difficulties and learn from mistakes.

I am thankful to Alessandro Crippa, who joined the group later on but who quickly became a trusted and supportive researcher and friend. He was always ready to discuss physics, no matter the time, and to support me inside and outside the lab.

I would also like to acknowledge Dr. Stefan Heun, with whom the experimental collaborations intensified in the last year of my research. He shared his expertise, feedback, and support with me with outstanding generosity.

I am indebted to many other colleagues without whom many of the works carried on wouldn't be possible. Among others, I would like to mention Lucia Sorba, Matteo Carrega, Michele Campisi, Luca Chirolli, Géraldine Haack, Sebastian Bergeret and Simone Gasparinetti.

I am in debt and gratitude with Arkady Fedorov and the SQD Lab who allowed my stay in Brisbane, even though for a short time. It was a great opportunity to learn from their lab activity and collaborate with them.

I would like to thank the managers and technicians at NEST laboratory who practically supported my activity: Daniele, Franco, Claudio and Pietro. They assisted me in debugging many challenging tasks in the cleanroom and handcrafting many workshop pieces. My gratitude goes to the Scuola Normale Superiore,

I would also like to thank all the friends and colleagues who came and left who created an enjoyable environment in the office and lab: Lennart, who is more than a colleague a lifetime friend; Giampiero, who I can always count on when talking about superconductors; Gaia, for being a sincere supporting friend; and Nico, Vittorio, Maria, Claudio, Daniel.

I don't want to forget the friends outside of the group who enriched my life beyond work. Thank you Giulia (you're a saint for dealing with me), Salvatore, Didi, Madhi; and my friends back home Simone, Mauro, Dario, Lorenzo, Marika.

Last but not least, I would like to express my heartfelt thanks to my family: my parents Paolo and Teresa; and my brother Daniele for their unconditional love and support. They have always been there for me through the ups and downs of this journey. Thank you nonno Michele, my everlasting supporter. And Sonia; thank you for being my soul-

mate; for joining me in any part of the world; for your love. I dedicate this thesis to them.

List of Publications

1. **Iorio, A.**, Rocci, M., Bours, L., Carrega, M., Zannier, V., ... Strambini, E. (2018). *Vectorial control of the spin-orbit interaction in suspended InAs nanowires.* Nano Letters.

2. Carrega, M., Guiducci, S., **Iorio, A.**, Bours, L., Strambini, E., ... Heun, S. (2019). *Investigation of InAs based devices for topological applications.* Spintronics XII, 144.

3. Strambini, E., **Iorio, A.**, Durante, O., Citro, R., Sanz-Fernández, C., ... Giazotto, F. (2020). *A Josephson phase battery.* Nature Nanotechnology, 15, 656–660.

4. Guarcello, C., Citro, R., Durante, O., Bergeret, F. S., **Iorio, A.**, ... Braggio, A. (2020). *rf-SQUID measurements of anomalous Josephson effect.* Physical Review Research, 2(2), 023165.

5. **Iorio, A.**, Strambini, E., Haack, G., Campisi, M., & Giazotto, F. (2021). *Photonic Heat Rectification in a System of Coupled Qubits.* Physical Review Applied, 15(5), 054050.

6. Turini, B., Salimian, S., Carrega, M., **Iorio, A.**, Strambini, E., ... Heun, S. (2022). *Josephson Diode Effect in High Mobility InSb Nanoflags.* Nano Letters, 22(21), 8502–8508.

7. Telesio, F., Carrega, M., Cappelli, G., **Iorio, A.**, Crippa, A., ... Heun, S. (2022). *Evidence of Josephson coupling in a few-layer black phosphorus planar Josephson junction.* ACS Nano, 16(3), 3538–3545.

8. **Iorio, A.**, Crippa, A., Turini, B., Salimian, S., Carrega, M., ... Heun, S. (2023). *Half-integer Shapiro steps in highly transmissive InSb nanoflag Josephson junctions.* Preprint arXiv. Accepted for publication on Physical Review Research.

9. Ruf, L., Elalaily, T., Puglia, C., Ivanov, Y. P., Joint, F., Berke, M., **Iorio, A.**, ... Di Bernardo, A. (2023). *Effects of fabrication routes on the control of superconducting currents by gate voltage.* Preprint arXiv.

10. Kaufman, R., White, T., Dykman, M. I., **Iorio, A.**, ... Naaman, O. (2023). *Josephson parametric amplifier with Chebyshev gain profile and high saturation.* Preprint arXiv.

1

Introduction

In the last few decades, we have been witnessing an explosive development of superconducting circuits which has reached a point where quantum effects and phase coherence are routinely exploited in many areas of quantum technologies, from quantum computing and simulation to standards for fundamental metrology. Underlying this development is the Josephson effect, the most famous phenomenon in mesoscopic superconductivity, in which a dissipation-free current flows through an oxide barrier between two superconducting electrodes even in the absence of a voltage bias. Despite the predominance of tunnel junctions in the history of Josephson effect studies, since the late 1960s considerable attention has been paid to junctions with non-tunnel conductivity, generally known as *weak-links*, consisting of metals, semiconductors, two-dimensional materials or geometric constrictions of a homogeneous superconductor. Although it took nearly 30 years to develop a microscopic transport theory able to treat these various weak-links in a unified way, even today many open questions remain and the application of non-tunnel weak-links to superconducting circuits is still in its infancy.

This thesis investigates both fundamental aspects and applications of superconducting circuits employing Josephson weak-links made up of semiconducting and metallic materials. The thesis is structured as follows:

- Chapter 2 serves as an introduction to the fundamental theoretical concepts that are crucial to comprehend the subsequent works in the context of superconducting circuits. We provide an overview of the concepts of mesoscopic superconductivity and Josephson weak-links. We strive to avoid deep formalism in favor of a more readable work, which highlights the most important aspects and the great variety and richness that the field can offer.

- Chapter 3 focus on the experimental methods that have contributed to all the experimental activity presented in this thesis. We will introduce low-noise and low-temperature electronic measurements and guide the reader through the experimental workflow necessary for working with superconducting quantum devices. Using my first-hand experience and the guidance of my senior coworkers, we will

motivate the choices we have made and highlight the advantages and potential areas for improvement.

- In Chapter 4, we present the first experimental work on the realization of a Josephson phase battery, a device that provides a persistent phase shift to the superconducting order parameter similarly to what a classical battery does with the voltage in an electronic circuit. The phase battery consisted of a single InAs nanowire embedded in an aluminum superconducting quantum interference device in which it was possible to induce an anomalous Josephson phase. The amplitude of the shift is consistent with the theoretical predictions and we revealed the odd parity with respect to the magnetic field for the first time.

- In Chapter 5, we investigate the half-integer Shapiro steps in an InSb nanoflag junction. The ballistic transport and low dimensionality of these nanoflags show some peculiar transport features, with the coexistence of short and long conducting channels. We investigated the device response under microwave irradiation, and unexpectedly observed strong half-integer Shapiro steps. We attribute our findings to a non-equilibrium quasiparticle distribution in the nanoflag, which is responsible for the double-periodic Josephson relation.

- Chapter 6 explores the impact of strong electric fields on superconducting constrictions, such as Dayem-bridges, in the context of the ongoing debate on gate-induced suppression of superconductivity. We measure the change in impedance of metallic weak-links embedded in coplanar based microwave resonators in the presence of intense electric fields. Our results can be understood in terms of a gate leakage-related mechanism, with hints suggesting the propagation of phonons extending throughout the chip area. We also conduct a systematic review of new and published results on similar wires in a meta-analysis, which highlights various aspects of the gating phenomenon.

- Chapter 7 explores potential applications of superconducting circuits for thermal transport, especially photonic heat rectification. We present a theoretical model of a quantum heat diode composed of two entangled flux qubits and two heat baths, and show how the rectification factor can be manipulated by tuning the qubits interaction and the baths couplings. Our work belongs to the emerging field of superconducting circuit quantum thermodynamics, with the potential to explore quantum heat transport with high accuracy and tunability.

2

Theoretical background

2.1. Weak-links

Superconducting weak-links are critical components in superconducting circuits. In the broadest sense, a weak-link is a portion of a superconducting circuit where the critical current is locally suppressed compared to neighboring regions, which allows for the accumulation of a phase gradient between the two ends. There are several physical implementations of weak-links, such as insulating barriers, point contacts, geometric constrictions, and hybrid structures based on normal metals, ferromagnets, semiconductors, quantum dots, and more (as depicted in Fig. 2.1a).

The supercurrent I_J flowing across a weak link is a function of the macroscopic and gauge-invariant phase difference φ across its boundaries. This functional dependence is called the Current-Phase Relation, denoted as CPR [1, 2] .

Josephson's original prediction was that a sinusoidal supercurrent of maximal amplitude I_c would result from the phase difference φ across the superconducting electrodes of a superconductor-insulator-superconductor (SIS) junction, represented as $I_J(\varphi) = I_c \sin(\varphi)$ [3]. In general, the shape of the CPR for a weak-link made of non-insulating materials depends on its specific implementation and is expressed as a sum of multiple harmonics with different weights $I_{c,n}$ and phase shifts $\varphi_{0,n}$, as given by

$$I_J(\varphi) = \sum_n I_{c,n} \sin(n\varphi + \varphi_{0,n}), \tag{2.1}$$

where the phase terms $\varphi_{0,n}$ vanishes in the presence of time-reversal symmetry (and will be discussed in the following).

While the specific form of the weak-link may impact the functional dependence of the CPR, the voltage drop across the junction is expressed as:

$$V = \frac{\hbar}{2e} \frac{d\varphi}{dt} \tag{2.2}$$

This expression arises from the temporal evolution of the phase difference between two Cooper condensates at different chemical potentials and is commonly referred to as the AC Josephson effect.

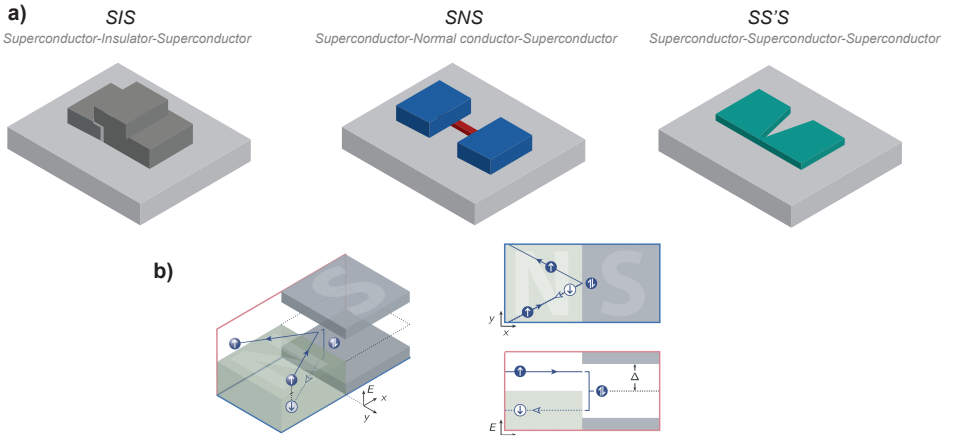

Figure 2.1: a) Illustrations of different implementations of weak-links. b) Schematic representation of the Andreev reflection process.

The free energy of the weak-link, $E(\varphi)$, can be determined by integrating the CPR with respect to phase, and conversely, the supercurrent corresponds to the slope of the phase-dependent free energy:

$$E(\varphi) = \int IV dt = \frac{\hbar}{2e} \int d\varphi I_J(\varphi) \qquad I_J(\varphi) = \frac{2e}{\hbar} \frac{\partial E(\varphi)}{\partial \varphi} \tag{2.3}$$

For a sinusoidal CPR, $E(\varphi)$ has the simple form $E(\varphi) = -E_J \cos(\varphi)$ with $E_J = \hbar I_c / 2e$ the Josephson energy. The standard junction has an energy minimum at $\varphi = 0$, when there is no current flowing across the junction.

The modern description of the Josephson effect relies on the existence of bound states in the weak-link, called Andreev bound states (ABSs). Reflections of quasiparticles at the superconductor-interfaces lead to the formation of spatially localized electronic states. [2, 4, 5] These quasiparticle states transfer Cooper pairs across the junction in form of counter-propagating electron-hole pairs, as illustrate in Fig. 2.1b. Due to the electron-hole symmetry, the ABSs come in pairs, one state has negative energy E_n^- and the other has positive energy E_n^+, where the specific transport channel is denoted by n. Each occupied state carries current proportional to the slope of its energy spectrum and the sum over the set of all channels defines the total supercurrent:

$$I_J(\varphi) = \frac{2e}{\hbar} \sum_n f(E_n^\pm) \frac{\partial E_n^\pm}{\partial \varphi}, \tag{2.4}$$

where the functional $f(E_n^\pm)$ describes the occupation of the nth Andreev bound state and, at equilibrium, is given by the Fermi-Dirac distribution. At zero temperature and in absence of perturbations, all ABSs with negative energies are occupied ($f(E_n^-) = 1$), while all ABSs with positive energies are empty ($f(E_n^+) = 0$), resulting in a constant occupation of the ABS spectrum in the ground state.

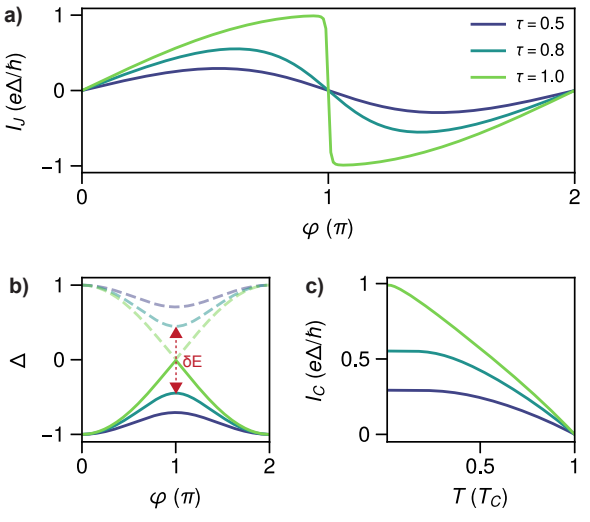

Figure 2.2: a) CPRs at $T = 0$ for a single channel ABS for different values of transparency τ. b) Phase-dependent energy spectrum for the same values of τ. At $T = 0$, only states at negative energies are occupied. The amplitude δE quantifies the minimum transition energy, which vanishes at $\tau = 1$. c) Temperature dependence of the critical current, extracted as $I_c = \max_\varphi I_J$, for the same values of τ.

2.2. SNS JUNCTIONS

The phase-dependent behavior of the ABS spectrum in a superconductor-normal conductor-superconductor (SNS) junction is intricately influenced by various factors, like its geometry, the specific material properties, or the presence of external fields. Of particular significance is the regime in which the junction operates, i.e., short or long with respect to the superconducting coherence length, as well as the nature of transport, whether it is ballistic or diffusive. In SNS junctions, the key energy scales that come into play are the superconducting gap Δ in the leads and Thouless energy E_{Th} of the normal region, representing the inverse of the average transition time through the junction. For ballistic transport, E_{Th} is given by $E_{Th} = \hbar v_F/L$, where v_F is the Fermi velocity and L is the junction length, whereas for diffusive transport in d dimensions, it is $E_{Th} = \sqrt{\hbar D/L^2}$, where $D = v_F l_e/d$ is the diffusion coefficient and l_e the electron mean free path. The relative amplitude of Δ and E_{Th} is determining the junction behavior, whether it behaves as a short junction ($L \ll \xi$, or equivalently, $E_{Th} \gg \Delta$) or a long junction ($L \gg \xi$, or $\Delta \gg E_{Th}$), where ξ is the superconducting coherence length given by $\xi = \hbar v_F/\Delta$ for ballistic transport and $\xi = \sqrt{\hbar D/\Delta}$ for diffusive transport.

2.2.1. SHORT JUNCTION LIMIT

In the short junction limit ($E_{Th} \gg \Delta$), the ABS energies have the well-known expression $E_n^{\pm}(\varphi) = \pm\Delta\sqrt{1-\tau_n \sin^2(\varphi/2)}$, where τ_n is the transmission probability of the nth channel. [4, 5] Thus, the ABS spectrum strongly depends on the transparency dis-

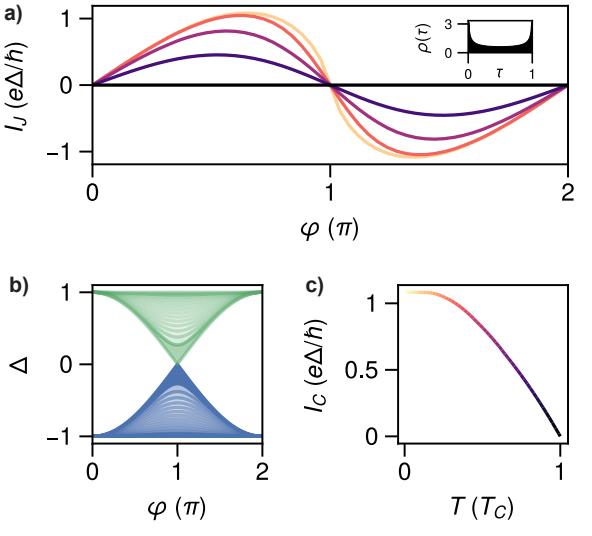

Figure 2.3: a) CPR calculated for a diffusive point contact at various temperatures using Dorokhov's distribution function shown in the top right inset. b) Energy distribution of the phase-modulated spectrum of the ensemble of ABSs contributing to the supercurrent, with denser spectra for $\tau = 0$ and $\tau = 1$. c) Temperature dependence of I_C is shown, with the individual traces in (a) color-coded based on the gradient shown.

tribution, which further defines the transport regime. Applying Equation 2.4 and using the Fermi-Dirac distribution $f(E_n^{\pm}) = \frac{1}{e^{E_n^{\pm}/k_BT}+1}$, it is straightforward to arrive at the expression:

$$I_J(\varphi) = \frac{e\Delta^2}{2\hbar} \sum_n \frac{\tau_n \sin\varphi}{E_n(\varphi)} \tanh \frac{E_n(\varphi)}{2k_BT}. \tag{2.5}$$

Figure 2.2 shows the energy dispersion, the corresponding CPRs at $T = 0$ and the temperature dependence of the critical current $I_C = \max_\varphi I_J$ for a single ($n = 1$) ABS of different transparency values τ.

In the tunnel regime ($\tau \ll 1$), the CPR reduces to the Josephson sinusoidal CPR given by the Ambegaokar-Baratoff formula $I_J(\varphi) = I_C \sin\varphi$, with $I_C = (e\Delta\tau/2\hbar)\tanh(\Delta/2k_BT)$. At perfect transparency ($\tau = 1$), it reproduces the Kulik-Omelyanchuk expression $I_J(\varphi) = I_0 \sin(\varphi/2)\tanh(\Delta\cos(\varphi/2)/2k_BT)$, where $I_0 = e\Delta/\hbar$ is the zero-temperature critical current for $\tau = 1$. The spectral gap $\delta E = E^+(\pi) - E^-(\pi) = 2\Delta\sqrt{1-\tau}$ quantifies the minimal transition energy between states with negative and states with positive energies and is vanishing at $\varphi = \pi$ and unitary transparency.

In the short diffusive limit, the junction exhibits an ensemble of electron propagation paths, each characterized by a specific length and transparency [2]. The effect of the diffusion is then to scramble the direction of electronic momenta and can be described as a collection of ABSs whose transmission coefficients are continuously distributed following Dorokhov's bimodal distribution $\rho(\tau)$, shown in the inset of Fig. 2.3a, describing many channels with low transmission ($\tau_n \to 0$) and many with high transmission prob-

abilities ($\tau_n \to 1$) [2]. This results in a dense ABS spectrum, as illustrated in Figure 2.3b. The corresponding CPR and temperature evolution of the critical current are plotted in panel a and c.

2.2.2. LONG JUNCTION LIMIT

In the long junction limit ($E_{Th} \ll \Delta$), the phase shifts due to the traversal time inside the weak link need to be considered, with the number of valid ABS solutions for each possible channel increasing as the junction length increases. In general, the treatment is more involved, so we will just briefly outline some main characteristics.

In the ballistic limit, even at $\varphi = 0$, Andreev bound states with energies that are much lower than the gap can be possible, and they exhibit a linear energy-phase dispersion [6, 7]. In the diffusive limit, the junction develops a phase-dependent minigap that evolves linearly at $\varphi = \pi$ with a maximum amplitude of $3.12\ E_{Th}$, following the expression $3.12E_{Th}|\cos(\varphi/2)|$ [8, 9]. In this case, the harmonic components of the current-phase relationship can be approximated at zero temperature as: [10]

$$I_{c,n} = -(-1)^n \frac{10.82E_{Th}}{eR_N} \frac{3}{(2n+1)(2n-1)}, \tag{2.6}$$

while this expression can be derived analytically in the short diffusive limit with the substitution $3 \times 10.82E_{Th} \to \Delta$.

An important feature that distinguishes the long-junction limit from the short-junction limit is the temperature dependence of the critical current. This has been calculated and experimentally measured by [11] which feature a crossover to an exponential decay with temperature on a scale given by the Thouless energy as the junction length increases.

2.3. SS'S JUNCTIONS

A Josephson junction formed by a constricted region separating two superconducting banks in a single superconducting film is known as an SS'S junction [2, 14, 15]. These structures can range from mesoscopic metallic microbridges to atomic-scale break junctions, where the distance between the two banks is only a few atoms thick. They are also referred to by various names, such as nanobridges, constrictions, Dayem-bridges, variable-thickness bridges, and so on, with each name highlighting a specific geometrical aspect of the weak-link type. In this study, we will focus on investigating Dayem-bridges, which are planar structures with the same film thickness (although bridges with varying thicknesses are also possible), with length being of the order of the zero-temperature coherence length ξ (as sketched in the inset of Fig. 2.4b).

Similar to SNS weak links, diffusive SS'S weak links can be categorized based on their normalized length, but the skewness of the CPR increases with the length unlike the former. Figure 2.4a illustrates the CPR of a one-dimensional SS'S weak link of different lengths. In the short limit, the superconducting properties resemble those of a standard Josephson junction, with a distorted $\sin(\varphi)$ dependence. However, as the junction length increases (i.e. for $L/\xi > 3.4$ [15, 16]), a multi-valued CPR develops corresponding to different windings of the superconducting phase along the superconducting wire (as shown by the blue trace in Fig. 2.4a).

The calculated CPR for the 2D geometry presented in the inset is shown in Fig. 2.4b,

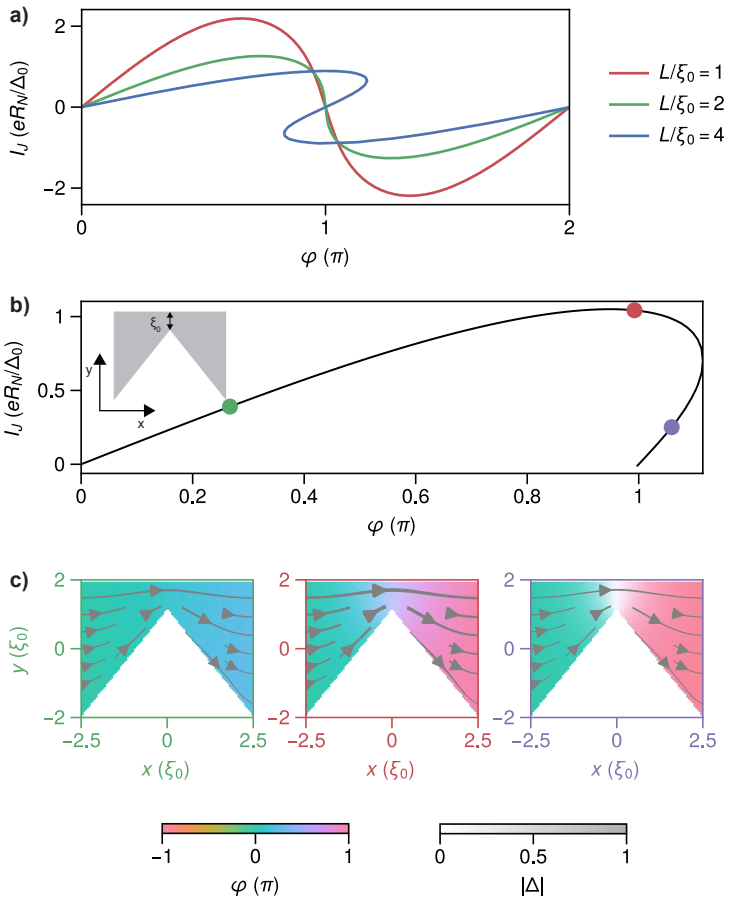

Figure 2.4: a) CPR for a metallic SS'S junction in the one-dimensional limit for different values of the normalized length L/ξ. In the long junction limit, the CPR becomes multi-valued. b) The CPR calculated for a planar 2D geometry shown in the inset. c) Evolution of the phase drop and pairing amplitude on the 2D geometry for different values of φ, corresponding to the dots in panel b). The colorbar $|\Delta|$ indicates the transparency of the data. Note that the unstable reverse branch (violet panel) features the nucleation of a *phase-slip center* in middle of the weak-link, where the superconducting order parameter $\propto |\Delta|$ is locally suppressed. These simulations were obtained by numerically solving the Usadel equation in 1D and 2D using the open-source packages `usadel1` [12] and `usadelnd` [13].

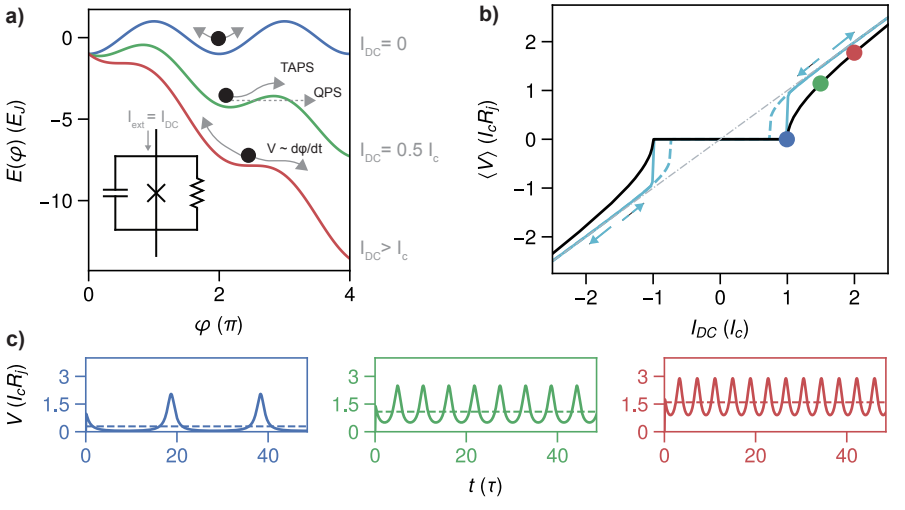

Figure 2.5: a) The junction's free energy for various values of DC current bias, characterized by a tilted washboard potential. Thermally activated phase slips (TAPS) or quantum phase slips (QPS) processes are also indicated. The inset depicts the circuit representation of the RCSJ model. b) Simulated $V(I)$ curves, with negligibly small (black line) and finite (cyan line) C_j. Here, $\langle V \rangle$ represents the time-averaged DC junction voltage. The solid/dashed cyan line corresponds to the current sweep direction shown by the arrows. c) The junction voltage $V(t)$ is displayed for the bias points presented in (b), in units of normalized time $\tau = 2eI_cR_j/\hbar$. The dashed lines indicate their average $\langle V \rangle$ value. All the simulations are done by numerically solving the time dynamics of the phase described by Eq. 2.8 using a Runge-Kutta method.

which describes the type of weak-links discussed in Chapter 6. Here, the channel width W is on the order of the coherence length ξ. The phase distribution across the junction geometry is shown in panel (c) for different values of φ.

2.4. PHASE DYNAMICS

So far, we have described the equilibrium CPR of different types of weak-links with respect to their geometrical properties and material, without any external bias. If the junction is biased with an external current $I_{ext} = I_{DC}$, the junction phase difference φ^* adjusts such that $I_{DC} = I_J(\varphi^*)$, as long as $I_{DC} < I_C$. For currents larger than the critical one, a zero-voltage solution does not exist, and the dissipative transport channels need to be taken into account. An accurate phenomenological model to describe the electrical characteristics of a junction under a current bias is the resistively and capacitively shunted junction (RCSJ) model, which can capture the main physical features of the device despite its microscopic details. [1, 17] Here, the physical junction is schematized as the parallel combination of an ideal Josephson weak-link of given $I_J(\varphi) = \mathrm{CPR}(\varphi)$, a resistor R accounting for the quasiparticle current, and a capacitor C_j accounting for the junction capacitance:

$$I_{ext} = I_J(\varphi) + \frac{V_J}{R_j} + C_j \frac{dV_J}{dt} \tag{2.7}$$

By substituting $V_J = \frac{\hbar}{2e}\frac{d\varphi}{dt}$, we can rewrite the above expression as:

$$I_{ext} = I_J(\varphi) + \frac{\hbar}{2eR_j}\dot{\varphi} + \frac{\hbar C_j}{2e}\ddot{\varphi}. \tag{2.8}$$

These equations describe a dynamics analogous to a *phase* particle of mass $M = (\hbar/2e)^2 C_j$ and damping $\eta = (\hbar/2e)^2/R_j$ moving in the so called *tilted washboard potential* $U(\varphi)$:

$$M\ddot{\varphi} + \eta\dot{\varphi} + \nabla U(\varphi) = 0, \qquad U(\varphi) = E_J\left(1 - \cos(\varphi) + \frac{I_{ext}}{I_c}\varphi\right), \tag{2.9}$$

where we assumed a sinusoidal dependence for the CPR $I_J(\varphi) = I_c \sin(\varphi)$. The generalization to the case of an arbitrary current-phase relation, which has higher-order terms, $\mathrm{CPR}(\varphi) = \sum_n I_{c,n}\sin(n\varphi)$, is straightforward.

When the external current is given by a DC current $I_{ext} = I_{DC}$, the potential will start to tilt. As long as $I_{DC} < I_c$, the phase difference is trapped in a local minimum corresponding to a dissipationless state. For $I_{DC} > I_c$, the phase particle will slide down, resulting in a running state with a finite DC voltage drop $\langle V\rangle = \frac{\hbar}{2e}\langle\dot{\varphi}\rangle \neq 0$, where the average is calculated over serval cycles of the normalized time $\tau = 2eI_cR_j/\hbar$. In the limit of small junction capacitance $C_j \sim 0$, the DC voltage drop can be derived analytically and is given by $\langle V\rangle = R_j\sqrt{I_{DC}^2 - I_c^2}$ (black line in Fig. 2.5).

Damping can cause capacitive hysteresis in the $V(I)$ curve for SIS junctions with non-negligible C_j (cyan line in Fig. 2.5b). Meanwhile, SNS junctions are immune to capacitive hysteresis but may experience thermal hysteresis, leading to overheating of the proximized metal's quasiparticles during the switch from the supercurrent branch to the dissipative voltage state (which is not accounted for in the RCSJ model) [18].

Although the RCSJ model provides a meaningful description of the dynamics of Josephson junctions, it has some limitations, some of which will be addressed in the following. Firstly, the phase variable is considered a classical variable, which neglects any effects associated with its quantum mechanical quantization [19, 20]. This means that the model does not account for the discrete energy levels that can exist in the minima of the washboard potential, which form the basis of superconducting qubits. At low temperatures, phase diffusion can be altered by quantum tunneling, whereas at high temperatures, it can be dominated by thermal activation, as depicted in the green line in Fig. 2.5a [1]. The quasiparticle transport in the junction is approximated by a normal resistance R_j, which fails to capture the non-linear dependence $R_j(V)$ or coherent higher-order processes such as multiple Andreev reflections [21, 22]. Finally, a nontrivial phase dynamics can result from a non-equilibrium quasiparticle population, which is particularly relevant in the presence of additional AC driving for highly transmissive junctions [23–25]. Therefore, while the RCSJ model provides a useful framework for understanding the basic behavior of Josephson junctions, it is crucial to understand its limitations when analyzing the behavior of real-world devices.

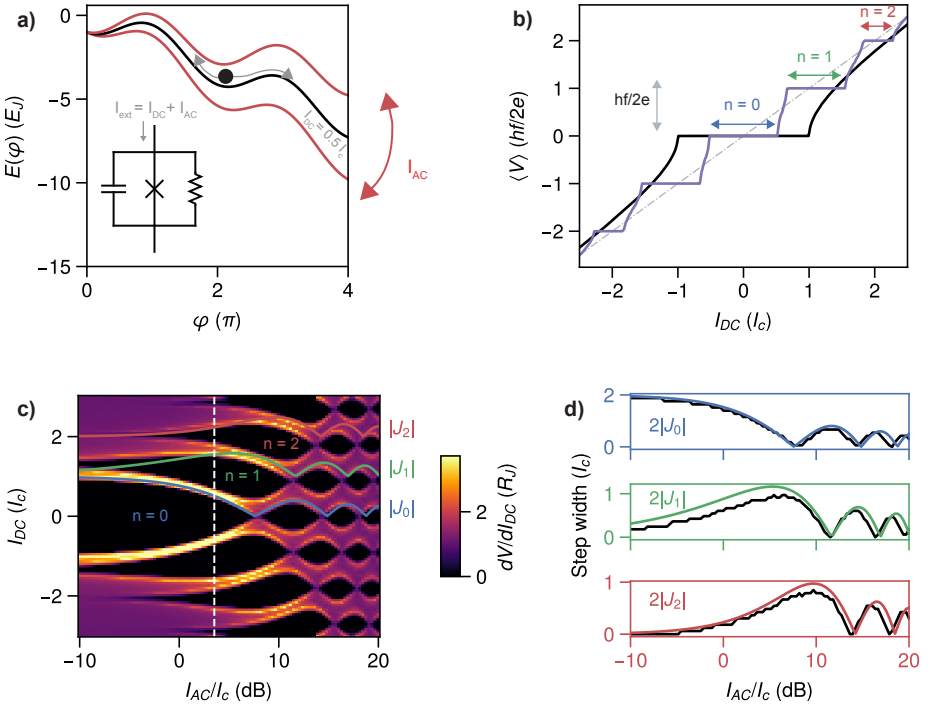

Figure 2.6: a) In the presence of a finite AC amplitude, the washboard potential changes the tilt angle by $\sim I_{AC}$ around the average tilt I_{DC}. b) The numerically simulated $V(I)$ curves are shown in violet in the presence of an AC current bias, while the black line corresponds to the case without AC bias. The voltage step amplitude is quantized in units of the driving frequency $hf/2e$. The colored arrows depict the step amplitude. c) The full evolution of the $V(I)$ curves as a function of I_{AC}. The dashed white line indicates the violet curve shown in (b). d) The step widths are shown as a function of I_{AC} and follow Bessel behavior when $f/\tau \sim 1$, with τ being the normalized time unit $\tau = 2eI_cR_j/\hbar$.

2.5. EFFECTS OF MICROWAVE IRRADIATION

When an external bias contains an AC component $I_{ext} = I_{DC} + I_{AC}\sin(2\pi ft)$ at frequency f, the washboard potential oscillates with an amplitude of I_{AC} around the average tilt I_{DC}. During a portion of the AC cycle, when $I_{DC} + I_{AC} > I_c$, the phase particle can move, while for the remainder of the cycle, it is trapped again in a local minimum. Because the synchronization of the particle movement and oscillatory tilt of the potential is possible for a range of DC current values, a voltage step appears in the $V(I)$ characteristic, as illustrated in Figure 2.6b. The motion of the phase particle is said to be *phase-locked* to the external drive. For instance, if the phase particle jumps one minimum for each period of the AC cycle, there is a phase change of $\dot{\varphi} = 2\pi f$ for a given I_{AC}. Increasing I_{AC} can result in the phase particle jumping two minima in one cycle, which corresponds to $\dot{\varphi} = 2 \times 2\pi f$. It is clear that if the phase jumps n minima,

then $\dot{\varphi} = n \times 2\pi f$, and this corresponds to an average voltage given by:

$$\langle V \rangle = \frac{\hbar}{2e}\langle \dot{\varphi} \rangle = n\frac{hf}{2e}, \tag{2.10}$$

where n is an integer, if the CPR is purely sinusoidal. This remarkable relation gives rise to quantized voltage plateaus, known as *Shapiro steps*, and is now widely used as a metrological voltage standard [26, 27]. Whenever the phase φ advances by $2\pi p$ in q AC cycles, *fractional steps* of number $n = p/q$ will result. This is particularly relevant when the junction potential $U(\varphi)$ has additional minima, for example in the case of a non-harmonic CPR. The step width has a non-trivial dependence on the drive amplitude and depends both on the bias scheme (i.e., whether the radiation couples via an AC voltage bias or current bias) and on the circuit environment surrounding the junction [28, 29]. It can be shown that for current biased, for $f/\tau \sim 1$ (where $\tau = 2eI_cR_j/\hbar$ is the normalized time unit), the step width is approximately described by the Bessel function of nth order:

$$\Delta I_n = 2I_c|J_n(I_{AC}/I_c)|, \tag{2.11}$$

while this expression is exact for the AC voltage bias case. The effect of the electromagnetic environment in which the junction is embedded can be accounted for appropriately by extending the RCSJ model. A particularly relevant case for our setup involves the additional AC shunting and dissipation formed by the device bonding pads and backgate when irradiated by the microwave drive using a coaxial antenna. This circuit is extensively discussed in [30–32], and will be employed in Chapter 5.

2.5.1. CPR UNDER MICROWAVE DRIVE

If the CPR contains higher order harmonics, additional fractional steps appear in the $V(I)$ curves. It is instructive to observe their evolution with the microwave irradiation in the voltage-biased case, since simple analytical results can be derived [1, 24]. The easiest approach is the so-called adiabatic approximation, where the phase-particle follows adiabatically the Josephson potential under AC drive without changing the occupancy of the ABSs that realize it. In this case $\varphi(t) = \varphi_0 + 2w\sin(2\pi ft)$, where $w = eV_{ac}/hf$ is the normalized oscillating AC voltage on the junction, and

$$I_J(\varphi) = \sum_n I_{c,n}J_0(2nw)\sin(n\varphi). \tag{2.12}$$

We illustrate the results of this approximation in Figure 2.7 for the zero-temperature case. In particular, the two upper panels show the CPRs for two different transparencies and values of the AC amplitude w. Panel a corresponds to the tunnel limit ($\tau = 0.1$) where the CPR is sinusoidal irrespective of the radiation power, while in panel (b), we show the results for a high transmission ($\tau = 0.99$). The panels in the bottom row show the current amplitudes of the first ($n = 1$) and second ($n = 2$) harmonic $I_{c,n}$ in the supercurrent. Notice that, independent of the value of driving w, only in the highly transmissive case it is possible to obtain a range of distorted CPRs with different values of higher harmonic components. For instance, for values of ac driving close to the first zero of the Bessel function $w \sim 1.2$, we observe a transition to double periodic CPR, where the Josephson supercurrent has a $\sin(2\varphi)$ dependence. The results of the

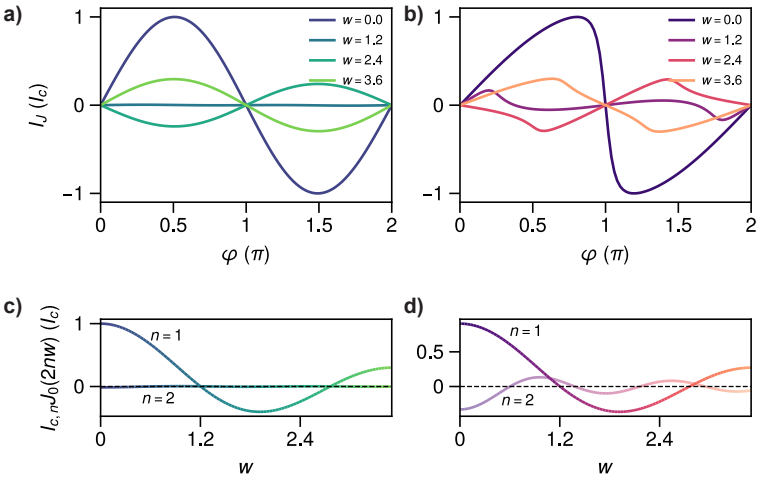

Figure 2.7: a) and b) CPRs for different values of the normalized microwave drive w for a sinusoidal and skewed CPR (obtained with Eq. 2.5 and a single channel of transparency $\tau = 0.99$), respectively, in the absence of driving. c) and d) Show the magnitude of the first and second harmonic components in the CPRs.

adiabatic approximation have been experimentally verified by Fuechsle et al. [33] and Dou et al. [34].

2.5.2. NON-EQUILIBRIUM EFFECTS

Non-equilibrium effects arise when the occupation $f(E,T)$ of the Andreev bound states contributing to the supercurrent in Eq. 2.4 deviates from the equilibrium one given by the Fermi-Dirac distribution [23–25, 35]. These effects become significant in highly transmissive SNS and metallic junctions, where even small energy differences near $\varphi \sim \pi$ can excite a considerable number of quasiparticles out of equilibrium.

When considering the non-equilibrium effects related to a microwave drive, transitions can occur between different ABSs as well as between ABSs and the continuum due to the absorption of (multiple) microwave photons resonant with the respective transition energies. This absorption leads to the promotion of a quasiparticle into an excited state, resulting in a negative contribution to the supercurrent and, therefore, a dip in the CPR. [24]

Although the understanding of non-equilibrium dynamics has gradually improved over time, many questions remain unanswered. For example, the Dayem-Wyatt effect, which refers to the enhancement of critical currents in metallic microbridges upon exposure to microwaves, has only recently received a satisfactory microscopic description [23, 36].

However the applicability of non-equilibrium theories is limited to diffusive SNS junctions or zero-length quantum point contacts, and there is still a gap between these predictions and some experimental observations, such as the observation of strong half-integer Shapiro steps discussed in Chapter 5.

In Chapter 6, we will discuss the gate-induced supercurrent suppression, which drives the superconducting condensate into a non-equilibrium state. Although this state is not induced by microwave radiation, the hypothesis regarding its origin will be discussed in greater detail in that chapter.

2.6. ANOMALOUS SUPERCURRENTS

All CPRs discussed so far share the property that, in the absence of a phase gradient, no supercurrent can flow, i.e., $I_J(\varphi) = 0$ when $\varphi = 0$. This property reflects the symmetry of the junction free energy under time-reversal and spatial inversion symmetries, which constraints $I_J(\varphi) = -I_J(-\varphi)$ [2]. However, in superconductors in which these two symmetries are broken, this feature can be violated, leading to spontaneous supercurrents even in the absence of a phase difference. In this case, the CPR can have an arbitrary phase shift φ_0 and in its simplest form takes the expression:

$$I(\varphi) = I_c \sin(\varphi + \varphi_0) \tag{2.13}$$

The Josephson energy is given by $E(\varphi) = -E_J \cos(\varphi + \varphi_0)$, and the ground state corresponds to $\varphi = -\varphi_0$, where a finite supercurrent at zero phase difference $I_{an} = I_c \sin(\varphi_0)$ flows, known as the anomalous supercurrent.

2.6.1. $0 - \pi$ PHASES

When a Zeeman field breaks time-reversal symmetry, the possible values for φ_0 are limited to either 0 or π. This is referred to as a Zeeman-induced $0-\pi$ transition. Historically, this transition has been studied in junctions with ferromagnetic layers. [38–43] However, the same effect can also occur in semiconductors with a spin-splitting field generated by either an external Zeeman field or a local exchange interaction, which is described by the Hamiltonian

$$H_Z = g\mu_B \mathbf{h} \cdot \boldsymbol{\sigma}. \tag{2.14}$$

Due to the spin splitting of the semiconducting bands induced by Eq. 2.14, as depicted in Fig. 2.8a, electrons with opposite spin at the Fermi level will acquire different momenta, $\mathbf{k}_\mathbf{F}^\uparrow = \mathbf{k}_\mathbf{F} + \mathbf{Q}/2$ and $\mathbf{k}_\mathbf{F}^\downarrow = \mathbf{k}_\mathbf{F} - \mathbf{Q}/2$. Thus, a Cooper pair, made up of two electrons with opposite spin and momentum, will acquire a finite center-of-mass momentum $\mathbf{Q}$. In turn, this translates to a spatial modulation of the superconducting order parameter, given by

$$\Delta(\mathbf{r}) = |\Delta| \cos(\mathbf{Q} \cdot \mathbf{r}). \tag{2.15}$$

Depending on the length of the electrons' trajectories $|\mathbf{r}|$, the order parameter is either positive or negative, corresponding to the ground state of the junction being at 0 or π superconducting phase difference. This spatially modulated superconducting state is widely known as the Fulde-Ferrel-Larkin-Ovchinnikov (FFLO) phase. [44, 45] The $0-\pi$ transition has been experimentally reported in SFS and SNS junctions. [41–43, 46, 47]

2.6.2. φ_0 PHASE

To observe anomalous phase shifts of arbitrary value, the weak-link energy must also lack parity-reversal symmetry. One typical example of a system that lacks inversion

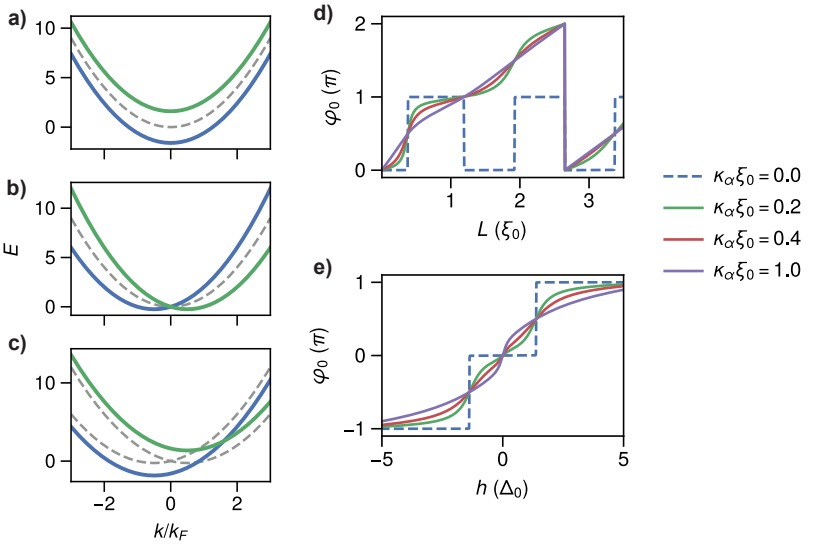

Figure 2.8: a) Energy of a single band in the presence of a Zeeman field. b) Energy of a single band in the presence of spin-orbit coupling without a Zeeman field. c) Energy of a single band with spin-orbit coupling and a Zeeman field in the $x - y$ plane. d) Anomalous phase φ_0 as a function of the junction length L for a diffusive junction in the presence of a Zeeman field $h = 5\Delta$, where Δ is the superconducting gap. e) Anomalous phase as a function of the Zeeman field h for $L = \xi_0$, with ξ_0 being the zero-temperature coherence length. The different traces in (d) and (e) represent varying strengths of κ_α, related to the spin-orbit coupling strength. For more detailed information, see [37].

symmetry is the widely-known Rashba Hamiltonian, which describes spin-orbit coupling (SOC): [48]

$$H_{SO} = \frac{\alpha_R}{\hbar}(\boldsymbol{\sigma} \times \mathbf{p}) \cdot \mathbf{z} \tag{2.16}$$

where α_R is the Rashba spin–orbit coupling strength, $\mathbf{p}$ and $\boldsymbol{\sigma}$ are the momentum and spin of the electron, respectively, and $\mathbf{z}$ is the unit vector along which inversion symmetry is broken [1]

The Rashba Hamiltonian produces single-particle states known as helicity states, which are depicted in Fig. 2.8b. The energy spectrum of these states is referred to as helical because they create circular bands in momentum space with fermion spins locked tangential to the momentum. [50]

When a Zeeman field in the $x-y$ plane is applied, the spin states shift asymmetrically, resulting in an asymmetric energy spectrum as shown in Fig. 2.8c. This same asymmetry is also reflected in the Andreev bound state energies of an SNS junction featuring such material, leading to $E(\varphi) \neq E(-\varphi)$, which is already indicative of the presence of an anomalous phase. [51]

Also in this case, the order parameter will become spatially modulated, with

$$\Delta(\mathbf{r}) = |\Delta| e^{i\mathbf{q}_0\mathbf{r}}, \tag{2.17}$$

where $\mathbf{q_0}$ is the helical modulation vector, which in the ballistic limit at strong SOC and weak magnetic field is given as $\mathbf{q}_0 = \frac{2\alpha}{v_F^2}(\mathbf{h} \times \hat{\mathbf{z}})$, with v_F the Fermi velocity. [50]

The presence of the SOC Hamiltonian in the junction free energy is shown through the Lifshitz invariant [37, 52, 53], which is proportional to the gradient of the superconducting order parameter and has the general expression

$$F_L = f(\alpha)\, \mathbf{T} \cdot \vec{\nabla}\varphi \tag{2.18}$$

where $f(\alpha)$ is a function of the spin-orbit strength and $\mathbf{T}$ is a polar vector odd under time reversal symmetry ($\mathbf{T} = \mathbf{h} \times \hat{\mathbf{z}}$ for Rashba SOC). Including the Lifshitz invariant in a minimal Ginzburg-Landau treatment for a ballistic junction close to T_c leads to the emergence of an anomalous phase φ_0, which has a simple expression: [53]

$$\varphi_0 = \frac{4\alpha h L}{v_F^2}, \tag{2.19}$$

where v_F is the Fermi velocity and L the junction length.

A deeper connection between the functional in Eq. 2.18 and magneto-electric effects in superconductors can be established [37, 54]. These effects are reminiscent of the widely studied spin Hall and Edelstein effects in normal conductors [55, 56]. The spin Hall and Edelstein effects describe the generation of a spin current or spin density, respectively, by a charge current. The inverse Edelstein effect, also known as the spin-galvanic effect, describes the generation of an electric current via a spin density.

[1] In planar low-dimensional systems, the breaking of inversion symmetry in the Rashba Hamiltonian is always perpendicular to the current transport, although the direction of the Rashba generating electric field can depend on the confinement, dimensionality, and local potential asymmetries. There are still unsolved questions about how the spin-orbit interaction arises in semiconducting nanowires, which we partially tried to explore in [49].

These effects exist in the superconducting state and were first studied by Edelstein himself [57]. The flow of a supercurrent can generate a spin polarization in the normal region (the Edelstein effect). A Zeeman field then can induce an anomalous supercurrent through the junction, even if the phase difference between the electrodes vanishes (inverse Edelstein effect).

To deal with magneto-electric effects, Bergeret and Tokatly [37] adopted the $SU(2)$-covariant formalism, which enables easy inclusion of magneto-electric Hamiltonians in superconducting systems and provides a direct method for determining the conditions for the emergence of anomalous currents. An extensive calculation of anomalous supercurrents has been performed in [37]. We summarize some central results in Figure 2.8d, where we plot the predicted φ_0 as a function of the junction length L (top) and the Zeeman field h (bottom). The factor κ_α is the spin-charge inverse length and depends on the strength of the Rashba spin-orbit coupling. As we can see, in the absence of spin-orbit coupling, only $0 - \pi$ values are possible. A finite κ_α breaks this phase rigidity, allowing for a continuum of φ_0 values. Moreover, the anomalous phase φ_0 is an even function of the Zeeman field h, a feature that we will experimentally probe in Chapter 3.

Finally, intrinsic phase shifts are challenging to measure because the phase difference adjusts itself such that $\varphi = \varphi_0$ to prevent a single junction from conducting any current. Nonetheless, we can create interference experiments to detect anomalous phases and their changes with spin-splitting fields, as we will further discuss in Chapter 3.

2.7. PHASE BIASING

By applying an external magnetic field, it is possible to externally control the gauge-invariant phase difference of Josephson junctions. [1, 58] In the case of a single junction, the field generates a phase gradient along the width of the junction, which can lead to interference effects and the well-known Fraunhofer pattern under uniform current density. In the case of two junctions connected in a loop in a superconducting quantum interference device (SQUID), the two junction phase differences become constrained to the external flux, enabling control of the supercurrent and detection of anomalous phases.

2.7.1. SINGLE JUNCTION

In the presence of an external magnetic field, the gauge-invariant phase difference φ of Josephson junctions becomes spatially modulated [58]. For example, in the geometry shown in Fig.2.9a, with a junction of length L and width W, in the gauge $\mathbf{A} = (0, Bx, 0)$, we have:

$$\varphi'(x) = \varphi - \frac{2\pi}{\Phi_0}\int_C \mathbf{A}\cdot d\mathbf{l} = \varphi - \frac{2\pi}{\Phi_0}\int_{-L/2}^{L/2} A_y dy = \varphi - \frac{2\pi}{\Phi_0} BxL, \tag{2.20}$$

where we integrated the vector potential $\mathbf{A}$ along the contour C shwon in Fig. 2.9a. The current through the junction is given by:

$$I_J(\varphi) = \int j(x,y) I_J(\varphi') dxdy = \int_{-W/2}^{W/2} J(x) I_J(\varphi - \frac{2\pi}{\Phi_0} BxL) dx, \tag{2.21}$$

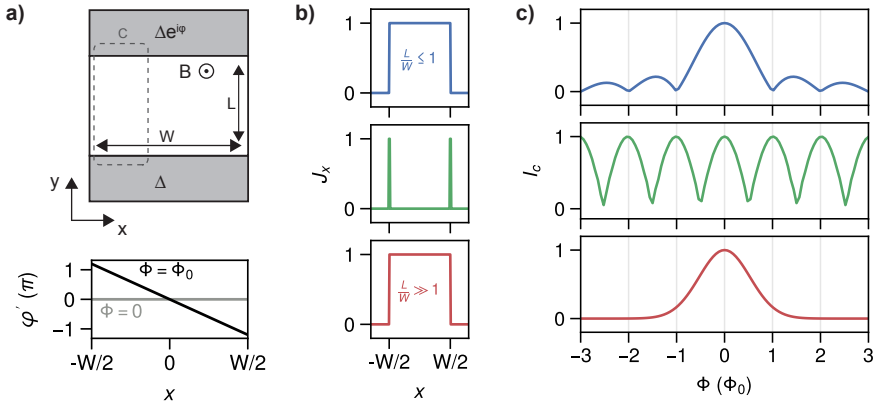

Figure 2.9: a) Top: Top view of the junction schematic indicating the junction length L, width W, magnetic field B, and the integration contour C. Bottom: Local phase difference occurring at magnetic flux values of $\Phi_e = 0$ and Φ_0. b) Current distribution J_x in three cases: homogeneous short (top), along the edges (center), and homogeneous long (bottom). c) Resulting magnetic interference patterns displaying Fraunhofer modulation (top), SQUID (center), and monotonic decay (bottom).

where we assume the current density distribution per unit length in y to be dependent on x only, $J(x)$.

For a uniform $J(x) = I_c/W$ current density, the critical current as a function of the flux through the junction $\Phi_e = BWL$ is $I_c(\Phi_e) = \max_\varphi I_J(\varphi)$ and results in the well-known Fraunhofer pattern:

$$I_c(\Phi_e) = I_c \left| \frac{\sin(\pi\Phi_e/\Phi_0)}{(\pi\Phi_e/\Phi_0)} \right| \tag{2.22}$$

When the current flows along the edges of the junction, $J(x) = I_c[\delta(-W/2)+\delta(+W/2)]$, it gives rise to an equivalent SQUID behavior. In this case, the phase difference is determined by the spatial modulation of the phases at the edges, and there is no phase gradient accumulated in the junction areas (assumed as delta functions δ), see Fig.2.9b (center row). The critical current I_c can be similarly derived as:

$$I_c(\Phi_e) = I_c |\cos(\pi\Phi_e/\Phi_0)| \tag{2.23}$$

Thus, magnetic interference allows for investigation of the homogeneity of the supercurrent density and the presence of possible edge states. However, the junction should be in the short junction limit for the trajectories to be straight, and the CPR should be sinusoidal. For long and narrow junctions ($L/W \gg 1$), the interference pattern deviates from the Fraunhofer pattern and exhibits a monotonous decay of the critical current with field (Fig. 2.9b, bottom row) [59, 60]. In the infinitely long junction limit the decay is approximately Gaussian:

$$I_c(\Phi_e) = I_c \exp\left(-\Phi_e^2/(2\sigma)^2\right) \tag{2.24}$$

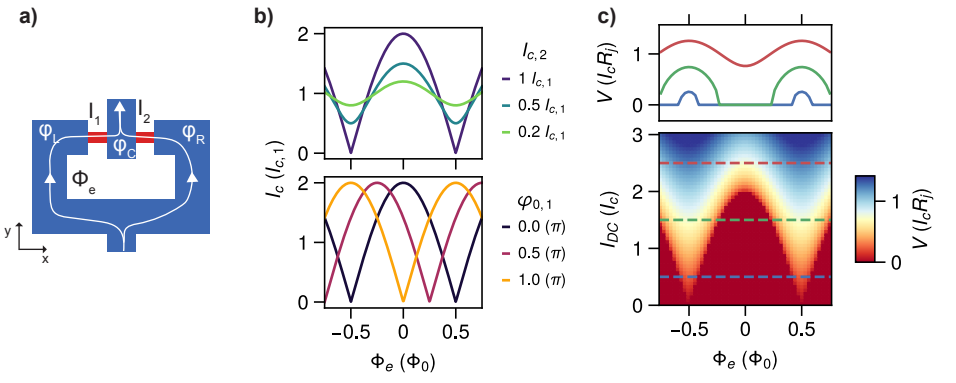

Figure 2.10: a) Schematic of a SQUID interferometer with the corresponding junctions' phase polarities. b) SQUID critical current I_c as a function of the external magnetic flux in the limit of low ring inductance. Top: for different values of junction critical current asymmetry. Bottom: for different values of anomalous phase present in one of the junctions in the symmetric current case. c) Complete $V(I)$ evolution for a SQUID with negligible loop inductance and symmetric critical currents. The top panel shows horizontal cuts (indicated in the map by dashed lines) highlighting the periodicity of the interference pattern even in the dissipative state.

with the value of σ depending on the exact geometry of the junction. The decay can be understood as dephasing caused by the magnetic field, where different Andreev paths in the normal region accumulate different phases. When the junction is short and wide, as discussed previously, the phase gradient along the NS boundary dominates with negligible phase accumulated along the junction length L. However, this is no longer true in the opposite limit. This behavior remains qualitatively similar for ballistic and diffusive transport, has been experimentally verified [60, 61], and will be relevant in Chapter 4.

2.7.2. SQUID

The superconducting quantum interference device (SQUID) is a system comprised of two Josephson junctions connected in parallel within a loop. The SQUID behaves as an effective single junction, whose critical current periodically depends on the external applied magnetic flux Φ_e piercing the loop area, making it a highly sensitive magnetometer [17]. Additionally, the SQUID can be used to obtain information about one of the junction's CPR or to detect anomalous phases.

When the phase polarities are taken as shown in Figure 2.10a, the flux quantization inside the loop constrains the difference of the junction phases, $\varphi_{1,2}$, to be proportional to the total magnetic flux, Φ, as given by:

$$\varphi_1 - \varphi_2 = 2\pi \frac{\Phi}{\Phi_0} \tag{2.25}$$

where $\varphi_1 = \varphi_C - \varphi_L$ and $\varphi_2 = \varphi_C - \varphi_R$. The total flux inside the loop is given by both the external flux Φ_e and the circulating screening current I_L in the case of a

non-negligible ring inductance L:

$$\Phi = \Phi_e + LI_L, \tag{2.26}$$

where we assumed for simplicity symmetric inductances between the two arms. The total supercurrent passing through the SQUID is given by

$$I_{SQUID}(\varphi_1, \varphi_2) = I_1(\varphi_1) + I_2(\varphi_2), \tag{2.27}$$

where $I_{1,2}(\varphi_{1,2})$ are the junctions' CPRs. The system of three equations above completely determines the interferometer's behavior in the superconducting state ($\dot{\varphi}_{1,2} = 0$).

In the limit of low loop inductance $L \sim 0$, the flux inside the loop equals the external flux $\Phi = \Phi_e$. Assuming sinusoidal CPRs, the SQUID supercurrent can be rewritten in terms of the external magnetic flux as

$$I_{SQUID}(\Phi_e, \psi) = I_c(\Phi_e)\sin(\psi), \tag{2.28}$$

where $I_c(\Phi_e) = \sqrt{I_{c,1}^2 + I_{c,2}^2 + 2I_{c,1}I_{c,2}\cos(\Phi_e)}$, and the average phase is introduced as $\psi = \varphi_1 + \eta = \varphi_2 + \eta - \Phi_e$, where $\tan\eta = -2I_{c,1} = \tan(\Phi_e/2)(I_{c,+} + I_{c,-}\tan^2(\Phi_e/2))^{-1}$, and $I_{c,\pm} = I_{c,1} \pm I_{c,2}$. In Fig. 2.10b (top), the SQUID's critical current is shown for different values of the critical current asymmetry between the two junctions, where the maximum current varies between $|I_{c,1} + I_{c,2}|$ and $|I_{c,1} - I_{c,2}|$. For symmetric junctions $I_{c,1} = I_{c,2}$, one recovers the expression of Eq. 2.23.

In Chapter 4, we use SQUIDs to detect anomalous phases, for which the CPR has the form $I_i = \sin(\varphi_i + \varphi_{0,i})$ with $i = 1, 2$. In this case, the interference pattern will be shifted by $\varphi_{0,i}/2$ with respect to the zero-phase value as a result of the self-generated flux due to the anomalous current, as shown in Fig. 2.10b (bottom).

The SQUID equations can be straightforwardly included in an RCSJ-like model to account for the dynamical evolution of the phase when in the presence of an external current I, and to describe the dissipative state $\langle V \rangle \neq 0$. This is demonstrated in Fig. 2.10c, which shows the full evolution of the $V(I)$ curves in the case of symmetric junctions and negligible ring inductance. The traces in the top panel show how the voltage drop in the dissipative state still reflects the periodicity of the interference, which is given by $V(\Phi_e) = \frac{R_j}{2}\sqrt{I_{DC}^2 - I_c(\Phi_e)^2}$, with R_j being the junction resistance.

2.8. JOSEPHSON INDUCTANCE

Although not explicitly expressed thus far, Josephson junctions behaves like (non-linear) inductors. By taking the time derivative of the CPR and making use of the AC Josephson relation, we can express

$$L_J(\varphi) = \frac{V}{\partial I_J(\varphi)/\partial t} = \frac{\hbar}{2e}\frac{\partial\varphi/\partial t}{\partial I_J(\varphi)/\partial t} = \frac{\hbar}{2e}\left(\frac{\partial I_J(\varphi)}{\partial\varphi}\right)^{-1}. \tag{2.29}$$

Thus, the Josephson inductance is proportional to the inverse of the slope of the junction CPR. In the case of a sinusoidal CPR, it takes the simple expression:

$$L_J(\varphi) = \frac{L_{J,0}}{\cos\varphi} \qquad \text{or} \qquad L_J(I) = \frac{L_{J,0}}{\sqrt{1 - (I/I_c)^2}}, \tag{2.30}$$

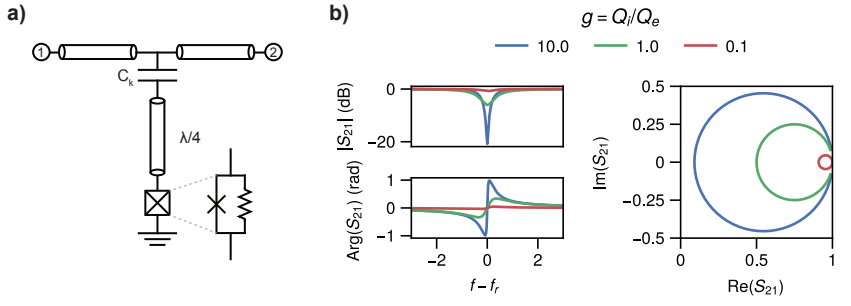

Figure 2.11: a) Circuit schematic of a $\lambda/4$ resonator coupled to a feedline and shorted to ground via a weak-link. b) Transmission coefficient S_{21} for different coupling regimes.

where $L_{J,0} = \frac{\hbar}{2eI_c}$ is the linear part of the inductance, which is inversely proportional to the junction critical current I_c. The latter expression also shows the nonlinear dependence of the inductance with respect to the supercurrent flowing through it, an important feature used for amplification processes, since it allows four-wave mixing parametric interaction.

In Chapter 6, we will probe the inductive component of metallic weak-links by embedding them in superconducting microwave resonators based on coplanar waveguides. Such resonators have been extensively used in the field of microwave detectors and circuit quantum electrodynamics [62, 63]. Our design will focus on hanging $\lambda/4$ resonators capacitively coupled to a feedline, as schematically depicted in Fig. 2.11a, which allows for easy multiplexing of several weak-links. The transmission coefficient S_{21} for this design can be derived as: [64]

$$S_{21} = 1 - \frac{\kappa_e}{\kappa_i + \kappa_e + 2i\delta} = 1 - \frac{1/Q_e}{1/Q_l + 2i(f/f_r - 1)} \tag{2.31}$$

where the internal and external loss rates are given by $\kappa_{i,e} = 2\pi f_r/Q_{i,e}$, the detuning by $\delta = 2\pi(f - f_r)$, and the loaded quality factor by $1/Q_l = 1/Q_e + 1/Q_i$. Figure 2.11b shows the evolution of S_{21} in magnitude, phase and polar plot for different values of the coupling factor $g = Q_i/Q_e$. The resonator frequency $f_r \propto 1/\sqrt{LC}$ allows to detect small changes in the weak-link critical current as a shift of the resonator frequency:

$$\frac{\delta f}{f_r} = -\frac{\delta L}{L}. \tag{2.32}$$

3

Experimental methods

In this Chapter, we outline the procedures and techniques used to investigate the properties of quantum nanoscale devices. The experiments were conducted in a newly installed dilution refrigerator, which provided the low-temperature environment suitable for low-noise quantum measurements. The experimental setup included both a DC and microwave setup, with the former assembled according to well-established practices in our group, while the latter was constructed from scratch to extend the range of frequencies investigated to the radiofrequency regime. The measurement techniques employed careful signal filtering, which will be extensively described for both the DC and RF setups. In addition, the fabrication process of the devices under study will be discussed, with a particular focus on the challenges associated with creating hybrid superconductor-semiconductor structures and metallic thin-film structures on highly insulating substrates.

3.1. Cryogenics

The cryostat used in our experiments is a 3He-4He dilution refrigerator that operates based on the low-temperature properties of a 3He-4He mixture. A more detailed explanation of the working principle can be found in [65]. This type of refrigerator is widely used and allows continuous cooling of large masses to ultracold temperatures as low as ~ 10 mK. A picture of the cooling unit is shown in Figure 3.1a. The cryostat itself consists of two vacuum chambers: the inner vacuum chamber (IVC), which houses the Still, the 50 mK, and the mixing chamber (MC) plate, and the outer vacuum chamber (OVC), which isolates the cryostat from room temperature. The OVC contains the 50 K and 4 K plates that are cooled by a two-stage pulse tube refrigerator, eliminating the need for liquid helium. During the cooling process to 4K, a small amount of helium exchange gas is inserted into the IVC (of the order of 3-4 mbar at room temperature) for thermal coupling of the remaining plates to the pulse-tube cooled 4 K plate. The cooling process to 4K takes approximately 2-3 days. The mixing chamber plate can reach temperatures as low as 35 mK for our machine. The 3He-4He circulation process is maintained by a series of pumps housed in the gas handling system (GHS), which can be remotely controlled

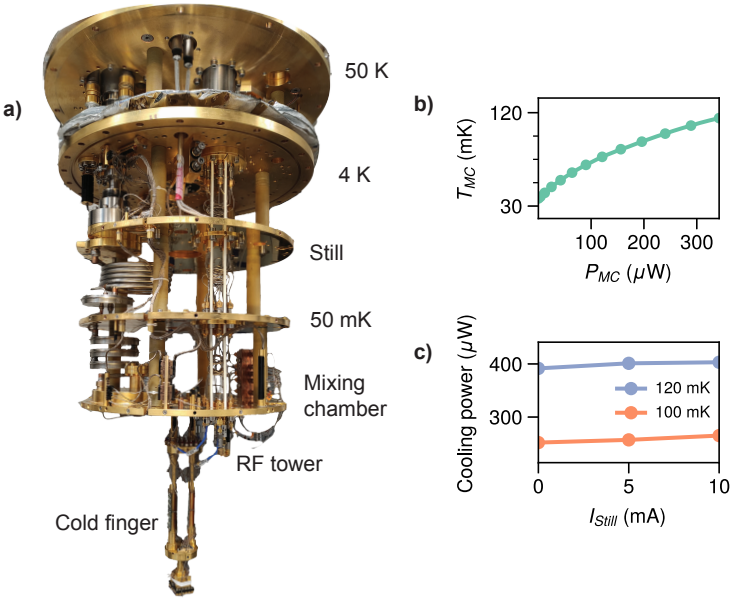

Figure 3.1: a) Picture of the dilution refrigerator with the various thermal stages. At the mixing chamber, a cold finger and an RF sample holder arae thermally anchored. b) Temperature of the mixing chamber plate is measured as a function of the power delivered to a 100 Ω resistor, which is anchored on the plate. c) Cooling power at the mixing chamber at 100 mK (in orange) and 120 mK (in violet), as a function of the current delivered to an heater on the Still.

via a front panel. The cryostat features a superconducting magnet that can provide magnetic fields up to 2T. For the experiments discussed in Chapter 3, a similar cryostat with a 3-axis vectorial magnet was used, with magnetic fields up to 1-1-5 T in the x-y-z plane. The sample stage of the cryostat has a cooling power of 250 µW at 100 mK and 400 µW at 120 mK, as shown in Figure 3.1b and 3.1c. The dilution fridge features 48 DC twisted pairs line, 14 high-frequency semi-rigid coaxial lines (13 CuNi and one superconducting NbTi), and up to 12 flexible coax lines that extend down to the mixing chamber stage. These lines are thermally anchored at various stages and filtered accordingly, as will be discussed later in the text. At the mixing chamber, a custom-made cold finger allocates two sample sockets, each with up to 24 pins, which can be inserted into the magnet and provided with a microwave antenna to irradiate the samples. A microwave sample holder featuring up to 8 lines is also directly anchored to the mixing chamber plate. Additional details on the filtering of the two setups will be given in the following.

3.2. DC TRANSPORT MEASUREMENTS

3.2.1. MEASUREMENT SETUP

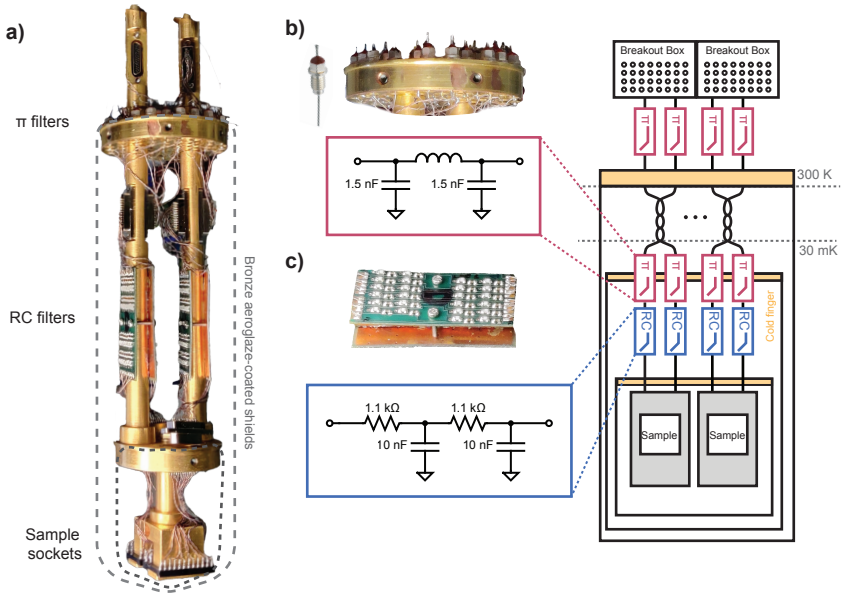

Figure 3.2: a) Cold finger featuring both π and RC filters, with two sample sockets located at the bottom. b) Detailed view of the π filters, along with corresponding circuit. c) Detailed view of the PCB with the RC filters, along with corresponding circuit.

To accurately measure Josephson junctions with small switching currents in the nA range, careful noise filtering is necessary. Our DC measurement setup, schematically depicted in Fig. 3.2, includes cascaded low-pass filters, both at room temperature and cryogenic temperatures, to achieve this. The circuit outside of the dilution refrigerator

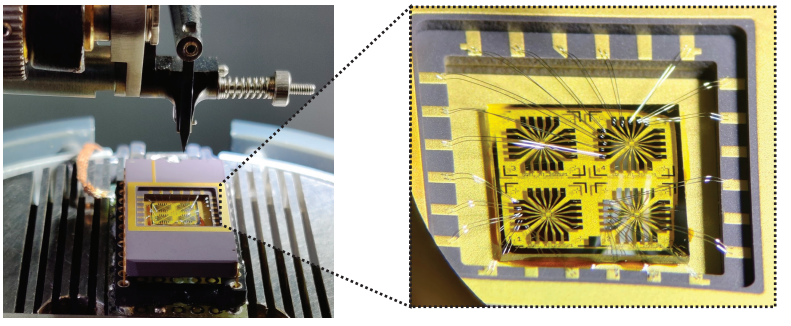

Figure 3.3: Typical device with aluminum wire bondings connecting the metal pads to the dual inline package.

includes breakout boxes with π-filters, which have a cutoff frequency of approximately 100 MHz. Inside the dilution fridge, a series of Oxley π filters and two-pole RC filters are used to heavily low-pass the lines (Fig. 3.2b and 3.2c). The RC filter consists of a 1.1 kΩ surface mount metal-film resistor and 10 nF capacitances, corresponding to a cutoff frequency of $\sim$ 6 kHz and 40 dB/decade isolation. Care needs to be taken on the resistor type, and thick film resistors must be avoided as they typically use oxide compounds (like ruthenium oxide) as the resistive film showing a strong temperature dependence below 1 K which makes the filters unreliable. Above $\sim$ 100 MHz, radiation starts to leak through again due to stray capacitances and parasitic inductances, so we further use π-filters (FLTM/P/1500) which guarantee 70 dB isolation up to 10 GHz. To prevent any stray microwave radiation, the sample and the cold finger are enclosed within both an outer and inner bronze shield. The inner surface of both shields is coated with commercially available Aeroglaze Z306 paint, which absorbs far-infrared stray radiation.

The connections are made by wire bonding the sample to a commercially available 24-pin ceramic dual inline package from NTK Ceramics. The sample is glued to the package using a small drop of cryogenic glue and the dual-inline is thermalized to the cold finger with Apiezon cryogenic grease. During the bonding process, the sample is inserted into a socket and electrically shorted and grounded to minimize the risk of damage from electrical discharge. A typical device is shown in Figure 3.3.

3.2.2. Four-wire measurements

The DC transport measurements are a crucial aspect of the experiments, as they involve the measurement of the $V(I)$ characteristics of small Josephson junctions. To ensure accurate measurements, a four-point measurement configuration is utilized, which eliminates the resistance introduced by wiring, filtering, and leads. As illustrated in Fig. 3.4a, the device under test (DUT) is biased through one set of leads using either a current source or a voltage source in series with a resistor. Another pair of leads is used to measure the voltage drop across the DUT. A preamplifier and a voltmeter with a high input resistance are employed, which ensures that negligible current flows through the second

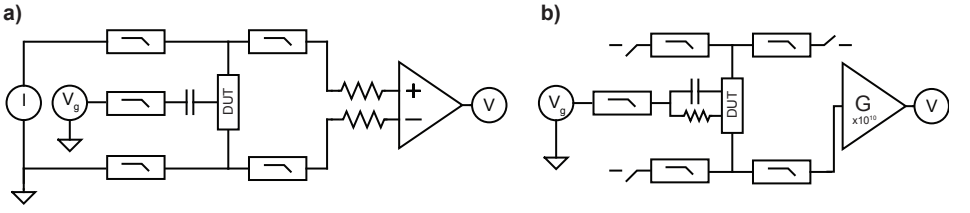

Figure 3.4: a) Example schematic of a four-wire measurement setup. b) Example circuit used to measure the leakage current discussed in Chapter 6.

pair of leads, and improve the signal-to-noise ratio, thus enabling an accurate measurement of the voltage drop across the DUT. Additional gate voltages are applied with low noise voltage sources on capacitive-coupled gate lines that are either fabricated on the chip or on the backgate of heavily doped Si/SiO_2 substrates.

In Chapter 5, the experiments on Shapiro steps involve coupling the microwave excitation to the junction using an open-ended coaxial cable that has been transformed into a monopole antenna with a center frequency of approximately 1.5 GHz. The antenna is positioned about 1 cm above the surface of the sample, and when aligned, the metallic sample leads act as a receiver of the environmental RF radiation.

3.2.3. LEAKAGE CURRENT MEASUREMENTS

In Chapter 6, the impact of leakage currents when applying high voltages to electrostatic gates will be discussed. We will carefully measure it by applying a voltage to the gate line and amplifying the small current (typically 10 fA - 100 pA) flowing into the device using a room temperature current preamplifier, while leaving all other lines floating, as shown schematically in Fig. 3.4b. The DL instruments 1211 current preamplifier, operated in battery mode, is used with a sensitivity of around 10^9 – 10^{10} V/A to convert the small current into a sizable voltage signal.

While the above method is the most accurate way to measure small leakage currents, it does not allow for monitoring them during standard four-wire measurements or for other device designs (like weak-links embedded in microwave resonators). As an alternative, we monitored the amount of current flowing directly at the voltage source. However, this method may include spurious current paths that flow to other grounds in the setup, resulting in additional contributions to the estimated leakage current value and thus an overestimation of the leakage current.

3.3. RF MEASUREMENTS

3.3.1. MEASUREMENT SETUP

Extending the capabilities of experimental setups to the microwave frequency range poses significant challenges in terms of noise reduction and signal amplification. Microwave filtering requires attenuation at multiple stages to reduce noise and ensure proper thermalization. [66] Excessive attenuation can overload the cooling power of the mixing chamber, so the CuNi microwave lines are attenuated with 20 dB, 10 dB, and

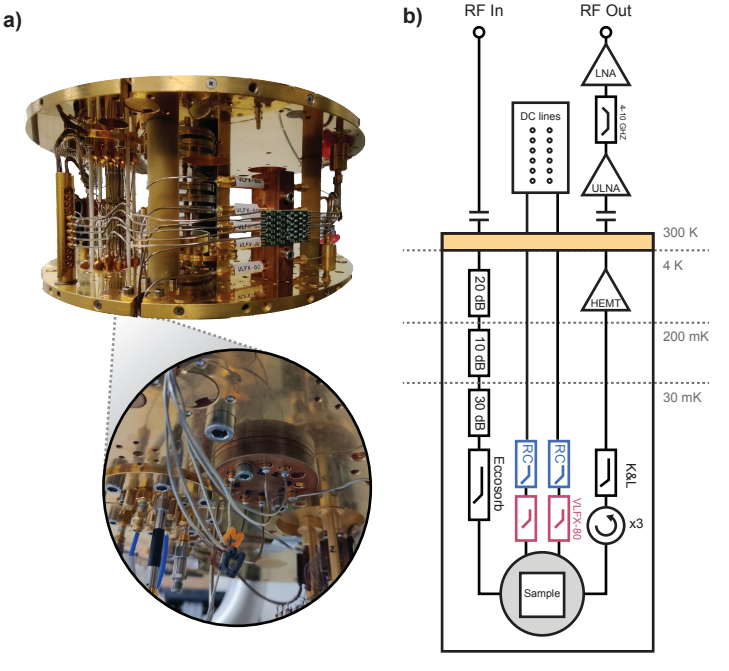

Figure 3.5: a) Mixing chamber plate featuring the microwave lines tower and the flexible DC-filtered coaxial lines. Below is a zoomed-in view of the mounted microwave sample holder with connected cabling. b) Full schematic of the microwave setup lines and filters.

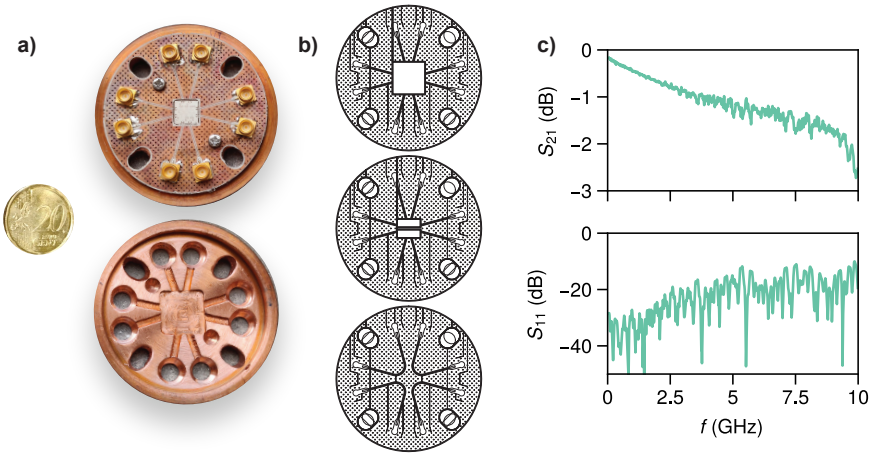

Figure 3.6: a) Microwave sample holder with its own copper lid hosting a prototypical device. A 20 cent coin is displayed as a length metric. b) Examples of fabricated PCBs. c) The S_{21} and S_{11} parameters of the PCB shown in (b) (third row) measured using a VNA. Two SMP connectors were soldered onto two shorted CPWs for the measurements.

30 dB at 4K, 50 mK, and the MC plate, respectively, using cryogenic XMA attenuators. To suppress stray far-infrared radiation, custom-made Eccosorb filters provided by KIT are used at the MC. The output line is made of superconducting NbTi up to 4K to reduce signal losses and is amplified at 4K using a commercial HEMT amplifier from Low Noise Factory with 4-8 GHz bandwidth. To prevent noise from the amplifier reaching the sample, a cryogenic triple junction circulator from Quinstar is used at the MC, ensuring 60 dB isolation. At room temperature, two MITEQ low-noise amplifiers are used to further boost the signal strength and improve the signal-to-noise ratio. At the mixing chamber, we use 5 flexible coax lines to bring filtered DC signals to the microwave sample holder. The lines are heavily low-pass filtered and feature VLFX-80 DC-80 MHz low-pass filters with 40 dB isolation up to 20 GHz and RC filters as discussed earlier. To combine DC and RF signals at low temperatures, additional cryogenic bias tees can be used. A full schematic of the setup lines and filtering is shown in Figure 3.5.

The microwave sample holder, shown in Figure 3.6a, features a practical *Octobox* design [67] that can accommodate samples up to 10×10 mm, 7×7 mm, or two 7×2 mm (as shown in Fig. 3.6b). The holder is completely shielded by a copper lid and can accommodate up to eight microwave lines. These lines are connected via SMP connectors to a 48 mm circular PCB based on high-frequency Rogers 3010 dielectric. The dielectric has a relative dielectric constant of $\epsilon_r \simeq 11$ at 10 GHz, which is similar to the Sapphire substrate employed for the devices. This helps to minimize impedance mismatch at the interface between the chip and PCB, since the waveguide launchers have similar dimensions.

The PCB is coated with 18 µm thick copper (front and back) and has vias with a spacing of approximately 1 mm to suppress any resonance modes between these two plates.

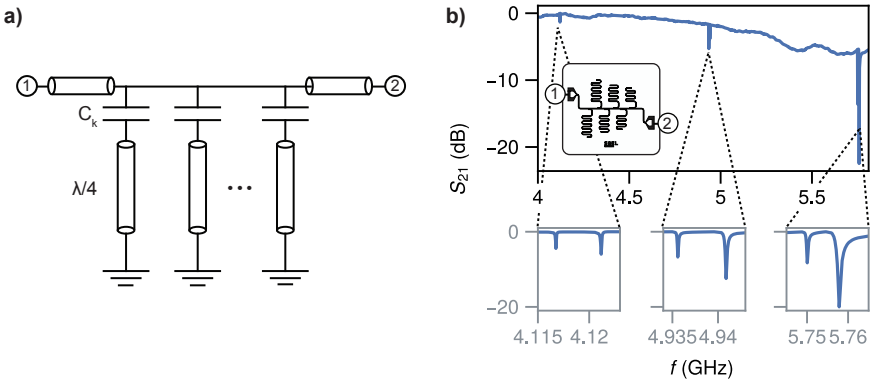

Figure 3.7: a) Circuit schematic of a typical transmission measurement. b) Transmission spectrum of $\lambda/4$ thin film microwave resonators with different coupling factors. The inset shows a CAD design of the device.

Additionally, there are 50 Ω coplanar waveguides (CPWs) for signal routing. Figure 3.6c shows the transmission and reflection of an identical PCB with shorted CPWs. It exhibits a reflection below 20 dB at 5 GHz and a nearly flat transmission band.

3.3.2. Spectrum analyzer measurements

Chapter 6 presents the results of our investigation into changes in the impedance of Dayem-Bridge weak-links, which we achieved by embedding the constrictions into a microwave resonant network. To measure the $S-$parameter of the device, we used a standard Vector Network Analyzer (VNA). Figure 3.7a shows a typical circuit schematic, which consists of $\lambda/4$ resonators coupled to a common feedline. When the resonators are on resonance, they load the feedline and produce a dip in the transmission spectrum, allowing for easy testing of multiple devices in parallel.

Figure 3.7b shows a typical transmission spectrum of a testing chip that comprises six Ti/Nb thin film (5/50 nm) microwave resonators without any weak-link embedded. We can easily distinguish different coupling factors over a wide, flat band.

3.4. Device design and fabrication

This thesis presents the results of two different device designs: superconductor-semiconductor Josephson junctions (Chapter 4 and 5) and planar metallic Dayem-bridges (Chapter 6). The former were fabricated by our collaborators, and we will provide only a brief outline of their fabrication process.

The devices involving semiconductor-superconducting Josephson junctions require generally a two-steps fabrication process. In the first, Ti/Au pads and markers are patterned via electron-beam lithography and are thermally evaporated on a Si-doped/SiO_2 substrate. The semiconductors are then dropcasted on the substrate via IPA droplets and are inspected under scanning electron microscope (SEM) to determine their location with respect to the marker positions. A CAD is produced to realize four-wire contacts

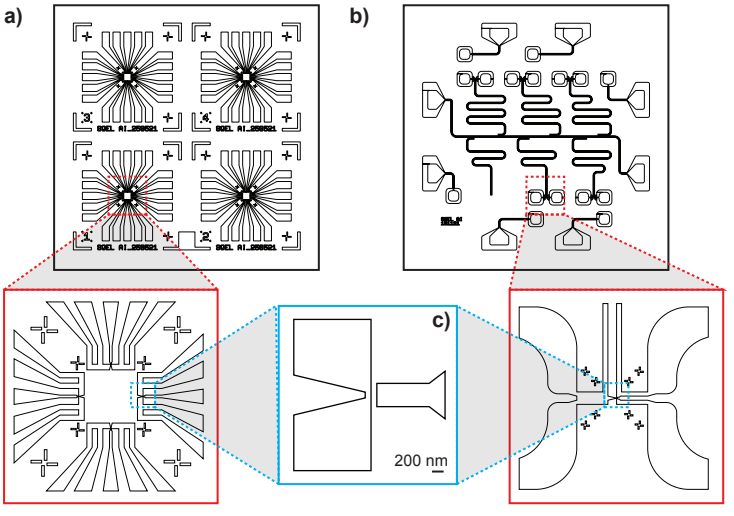

Figure 3.8: CAD designs of two prototypical samples for (a) DC transport and (b) microwave measurements discussed in Chapter 6.

and gate lines from the semiconductors to the closest bonding pads, which are realized in a second aligned EBL step. Before the metal deposition, a passivation step in H_2SO_4 is done to remove the natural oxide, and the mask is immediately placed in the vacuum chamber for metal deposition. Finally, electron-beam evaporated Al or sputtered Nb is deposited, in the latter case with an Ar ion-milling step to improve the semiconductor-metal contact.

For planar metallic Dayem-bridges, we focused on two designs shown in Figure 3.8, where a thin weak-link of typical width $W \sim 100$ nm is positioned in close proximity to a gate line at a distance of $d \sim 50-100$ nm. Typical film thickness ranges from $t \simeq 25-50$ nm. The first design, shown in Fig.3.8a, allows for standard DC characterization of the weak-link properties, while the second, shown in Fig.3.8b, embeds the weak-link galvanically in a resonant microwave network. The galvanic coupling of very large and very small structures, as well as the challenges of working with thin films and dealing with the Sapphire substrate, make the fabrication of the second design particularly challenging. We will discuss in detail the two approaches that we followed: a double-step etching process (top-down approach) and a single-step lift-off process (bottom-up approach).

Devices fabricated through the top-down approach (Nb and Al devices) involve the deposition of a thin metal film via sputtering (Nb) or electron-beam evaporation (Al), followed by optical lithography steps to define the large structures, and RIE/ICP etching to remove the unwanted metal. Aligned electron-beam lithography (EBL) steps then define the small structures, which are also etched using ICP. A detailed schematic of the process flow is illustrated in Figure 3.9.

Devices fabricated using the bottom-up approach (Al and Ti devices), involve defining both large and small structures in a single electron-beam lithography step, followed by metal deposition through electron-beam evaporation of Al or Ti. For microwave de-

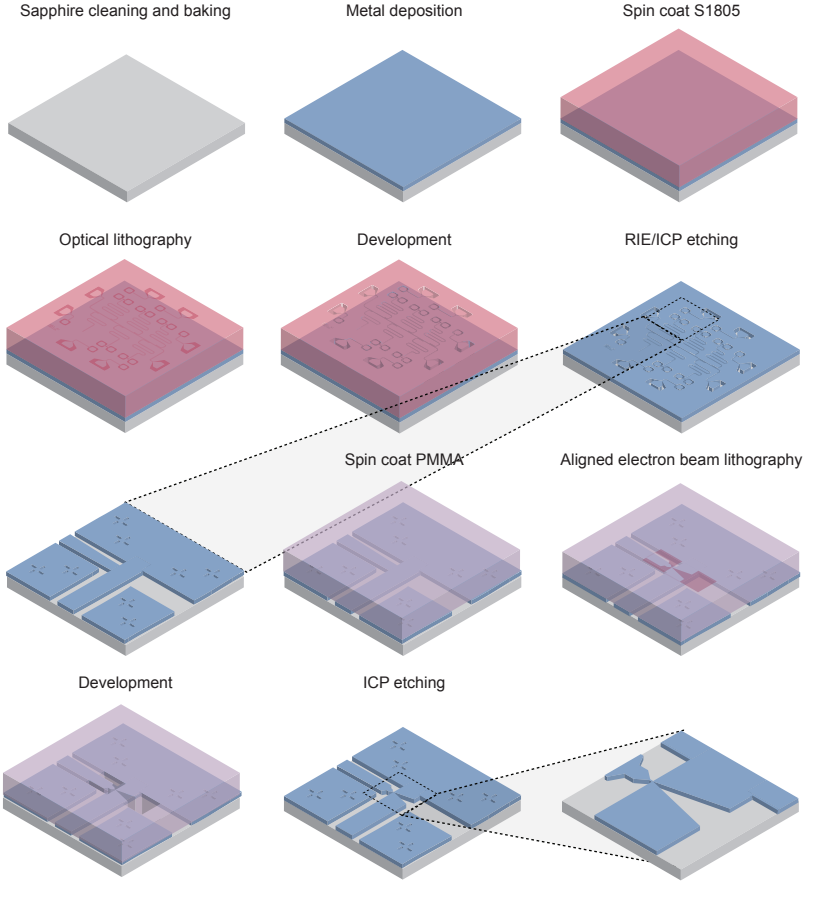

Figure 3.9: Example of a double-step etching process for the microwave devices.

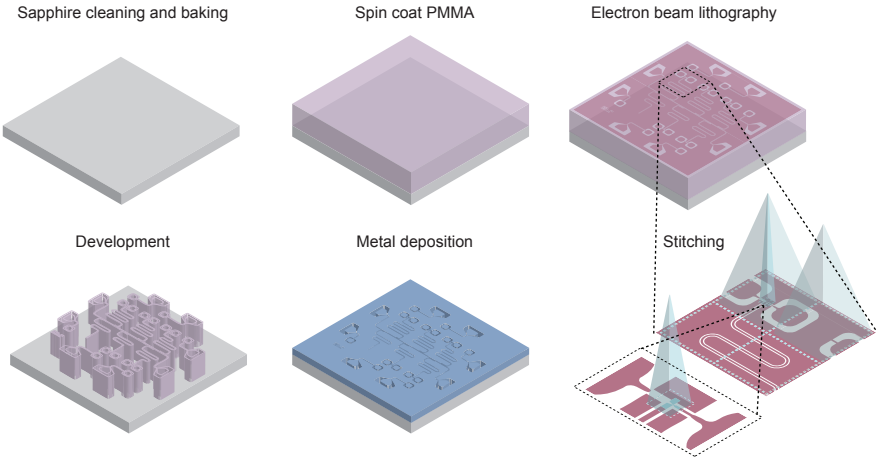

Figure 3.10: Example of a single-step lift-off process for the microwave devices. The zoom-in on the bottom right illustrates the division in writing field areas of the pattern and the corresponding beam deflection areas. A further zoom-in shows the large and small features together, placed concentrically, and requiring careful alignment.

vices, this requires exposing the majority of the mask, resulting in a total exposure time of approximately 12 hours using the maximum beam current available in our EBL system ($\sim$ 10 nA). A detailed schematic of the process flow is illustrated in Figure 3.10.

While both approaches seem straightforward, caution and consideration must be taken into account.

Challenges for etched devices:

- It is important to have well-defined markers for aligning the two lithography steps. The contrast of the metal structure under a scanning electron microscope is determined by the atomic number Z of the element. Therefore, gold markers ($Z = 79$), are often used. In our case, we defined the markers during the first etching step of the thin metal. While this approach worked reasonably well for Nb ($Z = 41$), it was nearly impossible to see the markers for Al ($Z = 14$). To avoid the need for additional markers, in the latter case we decided to reverse the lithography steps.

- While big structures can be etched using either RIE or ICP etching, only ICP etching can achieve sufficient resolution (below 100 nm) for small structures. RIE etching is isotropic, meaning that for our typical thickness film of 50 nm, it would etch the lateral side of the structures to a distance of 100 nm, limiting the minimum achievable pitch to this distance.

Challenges for lift-off devices:

- When designing structures that extend over multiple writing fields of the beam, careful stitching is required. Furthermore, if the design includes small and large structures in precise contact, extra attention is necessary to align the different

apertures of the beam. This is depicted in Figure 3.10 (lower right corner), where we show the division of the CAD design in different writing fields along with the corresponding beam deflection areas. The zoom-in image provides a closer look at the additional small features. Specifically, if the writing field is not well-aligned with respect to the sample coordinate, any angle error could cause the stitching to fail between the areas. Additionally, big and small features need to be concentrically placed to ensure proper alignment between the two.

Challenges in dealing with Sapphire substrates:

- Sapphire is an extremely insulating substrate, and charging effects can deflect the beam during exposure. To mitigate this issue, a thin layer of conductive polymer is spun above the PMMA for each exposure.
- Since Sapphire is transparent, extreme care must be taken not to flip the devices. The transparency further complicates the autofocus procedure in the optical laser writer lithography machine.

3.5. Measurement acquisition

The control over the instrumentation was performed with a custom Python library based on the open-source framework QCoDeS (Quantum Control and Dynamics in Experiment) [68]. QCoDeS is designed for controlling and acquiring data from scientific experiments, particularly those in the field of condensed matter physics and quantum computing. The library provides a set of tools for building and controlling experimental setups, including a comprehensive set of instrument drivers that enable communication with various types of laboratory equipment.

The decision to switch from LabVIEW programs previously adopted in the group to Python-based instrument control represents a significant improvement in experimental efficiency and flexibility. Unlike LabVIEW, which requires specific software licenses and training, QCoDeS can be easily installed, customized, and adapted to specific experimental needs. We also developed comprehensive acquisition routines to adapt to our needs, which, when combined with real-time plotting packages and Jupyter notebooks, allowed for fast acquisition, logging, and analysis of the experimental data.

Despite the many benefits of using QCoDeS, the lack of a graphical user interface (GUI) can make the learning curve more steep for a new user. However, we believe that the overall advantages just mentioned, the user-friendly Python syntax and extensive documentation outweigh the initial learning curve.

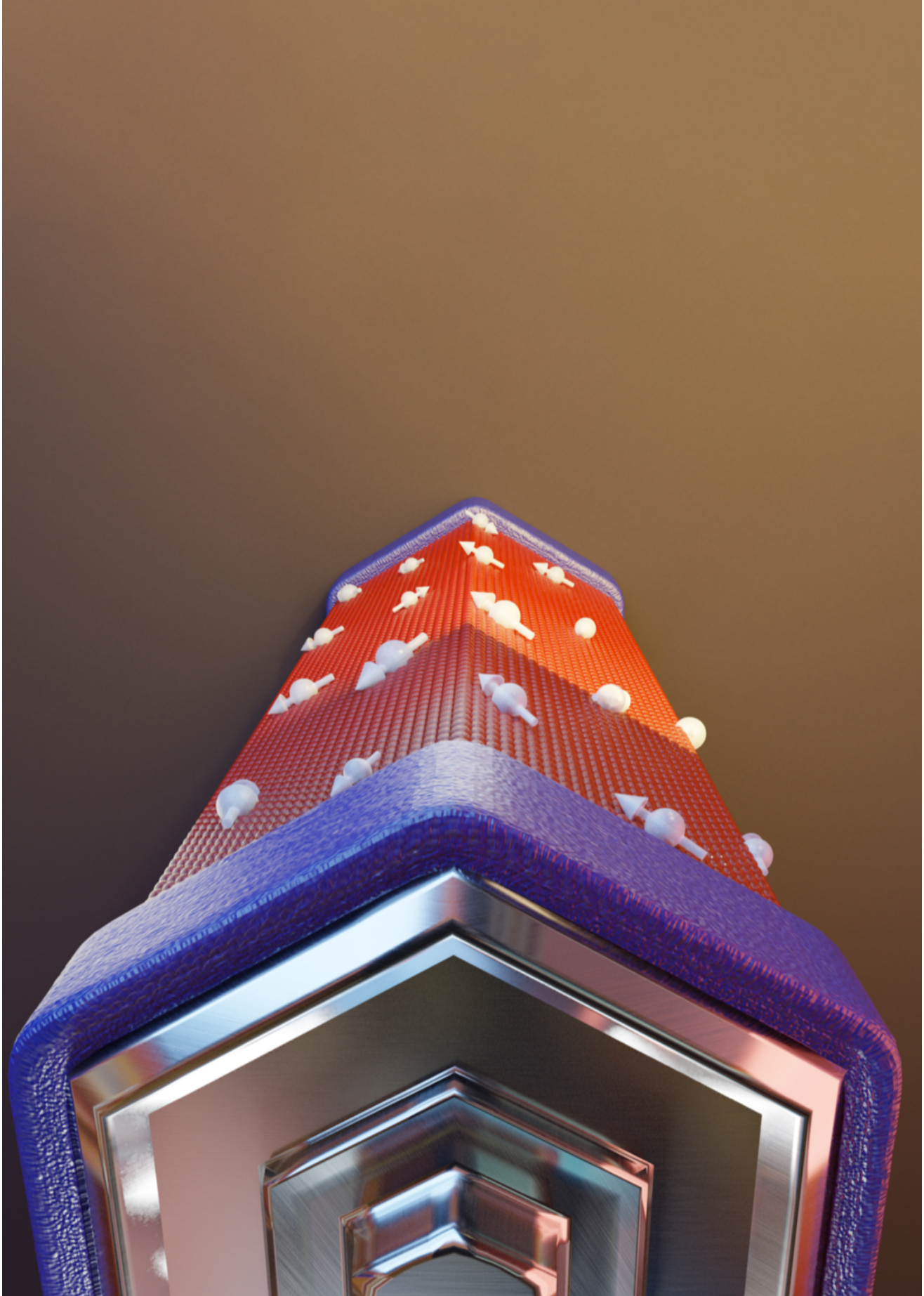

4

A Josephson phase battery

4.1. Introduction

A classical battery converts chemical energy into a persistent voltage bias which can power electronic circuits. Similarly, a phase battery is a quantum device which provides a persistent phase bias to the wave function of a quantum circuit. It represents a key element for quantum technologies based on phase coherence. Here we demonstrate a phase battery in a hybrid superconducting circuit. It consists of an n-doped InAs nanowire with unpaired-spin surface states and proximitized by Al superconducting leads. We find that the ferromagnetic polarization of the unpaired-spin states is efficiently converted into a persistent phase bias φ_0 across the wire, leading to the anomalous Josephson effect [37, 53]. We apply an external in-plane magnetic field and, thereby, achieve continuous tuning of φ_0. Hence, we can charge and discharge the quantum phase battery. The observed symmetries of the anomalous Josephson effect in the vectorial magnetic field are in agreement with our theoretical model. Our results demonstrate how the combined action of spin-orbit coupling and exchange interaction induces a strong coupling between charge, spin and superconducting phase able to break the phase rigidity of the system.

At the base of phase-coherent superconducting circuits is the Josephson effect [3]: a quantum phenomenon describing the flow of a dissipationless current in weak-links between two superconductors. The Josephson current I_J is then intimately connected to the macroscopic phase difference φ between the two superconductors via the current-phase relationship $I_J(\varphi)$. If either time-reversal ($t \to -t$) or inversion ($\vec{r} \to -\vec{r}$) symmetries are preserved, $I_J(\varphi)$ is an odd function of φ and the CPR, in its simplest form, reads $I_J(\varphi) = I_C \sin(\varphi)$ [2], with I_C being the junction critical current. This means that, as long as one of these symmetries is preserved, an open Josephson junction (JJ) ($I_J = 0$) cannot provide a phase bias or, accordingly, a JJ closed on a superconducting circuit ($\varphi = 0$) cannot generate current. As a consequence, the implementation of a phase battery [69] is prevented by these symmetry constraints which impose a rigidity on the superconducting phase, a universal constraint valid for any quantum phase [70, 71].

Our demonstration consists of an n-doped InAs nanowire with unpaired-spin surface

states and proximitized by Al superconducting leads. We find that the ferromagnetic polarization of the unpaired-spin states is efficiently converted into a persistent phase bias φ_0 across the wire, leading to the anomalous Josephson effect [37, 53]. We will discuss later what these unpaired-spin surface states might be.

The breaking of time-reversal symmetry (alone) maintains the phase-rigidity but enables two possible phase shifts 0 or π in the CPR. The 0-π transition has been extensively studied in superconductor/ferromagnet/superconductor junctions [72, 73], and has applications in cryogenic memories [74, 75]. On the other hand, if both time-reversal and inversion symmetry are broken, a finite phase shift $0 < \varphi_0 < \pi$ can be induced [37, 76] and the CPR reads:

$$I_J(\varphi) = I_C \sin(\varphi + \varphi_0). \tag{4.1}$$

A junction with such CPR, called as a φ_0-junction [53], will generate a constant phase bias $\varphi = -\varphi_0$ in an open circuit configuration, while inserted into a closed superconducting loop it will induce a current $I = I_C \sin(\varphi_0)$, usually denoted as *anomalous* Josephson current. Recently, anomalous Josephson currents have been the subject of theoretical [69, 77] and experimental works [78–80] envisioning direct applications in superconducting electronics and spintronics [69, 81].

If we apply an external in-plane magnetic field and, we achieve continuous tuning of φ_0. Hence, we can charge and discharge the phase battery.

Lateral hybrid junctions made of materials with a strong spin-orbit interaction [78, 80] or topological insulators [79] are ideal candidates to engineer Josephson φ_0-junctions. The lateral arrangement breaks the inversion symmetry and provides a natural polar axis $\hat{\mathbf{z}}$ perpendicular to the current direction. Moreover, the electron spin polarization induced by either a Zeeman field or the exchange interaction with ordered magnetic impurities breaks the time-reversal symmetry. In this case, the anomalous φ_0-shift is ruled by the Lifshitz-type invariant in the free energy (F_L), which has the form [37]:

$$F_L \sim f(\alpha, h)(\mathbf{n_h} \times \hat{\mathbf{z}}) \cdot \mathbf{v_s}, \tag{4.2}$$

where $f(\alpha, h)$ is an odd function of the strength of the Rashba coefficient α and the exchange or Zeeman field h, $\mathbf{n_h}$ is a unit vector pointing in the direction of the latter, and $\mathbf{v_s}$ is the superfluid velocity of the Cooper pairs flowing in the JJ. The scalar triple product then defines the vectorial symmetries of φ_0, while the amplitude of the shift depends on sample-specific microscopic details as well as macroscopic quantities like temperature.

4.2. DEVICE CHARACTERIZATION

Driven by the geometric condition for a finite φ_0-shift (Eq. 4.2), we realized a phase battery (Fig. 4.1a and b) consisting of a JJ made of an InAs nanowire (in red) embedded between two Al superconducting poles (in blue). The supercurrent, and hence $\mathbf{v_s}$, flows along the wire (x-direction) which is orthogonal to the effective $SU(2)$ Rashba magnetic field vector pointing out of the substrate plane (z-direction) hosting the InAs nanowire. In the same nanowire, surface oxides or defects generate unpaired spins behaving like ferromagnetic impurities (represented by yellow arrows in Fig. 4.1a) that can be polarized along the y-direction to provide a persistent exchange interaction h in this direction.

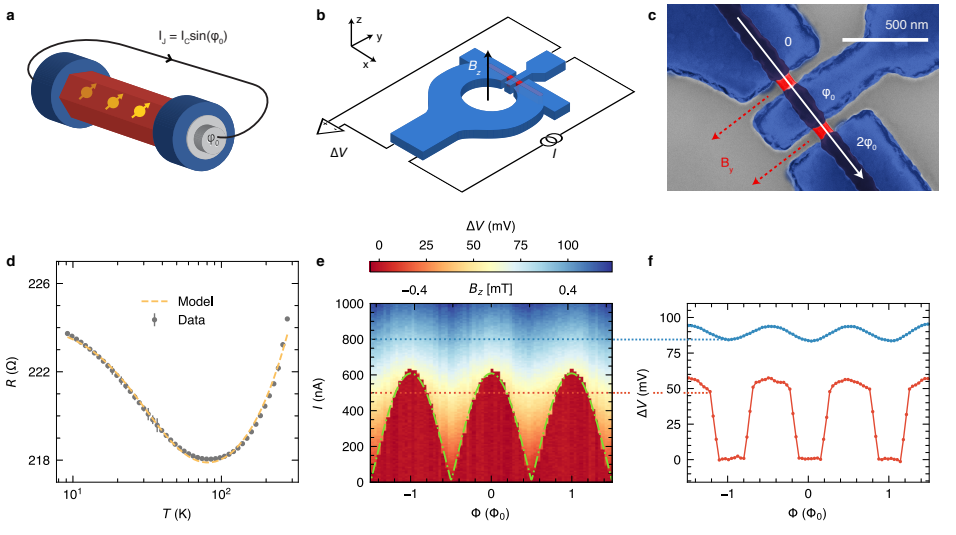

Figure 4.1: Josephson phase-battery device. a, Conceptual scheme of a Josephson phase battery composed of an InAs nanowire (red) embedded between two superconducting poles (blue) converting the spin polarization of surface unpaired spins (yellow) into a phase bias φ_0. The battery, inserted into a superconducting circuit, can generate a supercurrent proportional to $\sin(\varphi_0)$. **b,** Schematic illustration of the hybrid InAs nanowire-aluminum SQUID interferometer used to quantify the phase bias φ_0 provided by the two JJs (in red). The ring lies in the $x-y$ plane with the nanowire parallel to the x-axis. A magnetic field B_z piercing the ring is used to modulate the SQUID critical current (I_S) measured in a 4-wire setup. I is the current flowing through the interferometer, whereas ΔV is the resulting voltage drop across the device. **c,** False-colored SEM image of the active region of the phase battery composed of the two φ_0-junctions. B_y is the in-plane magnetic field orthogonal to the nanowire. **d,** Temperature dependence of the normal-state resistance $R(T)$ of the interferometer showing a Kondo upturn at low temperatures which is consistent with a background of magnetic impurities. From the fit (yellow curve) we estimate a spin density of ~ 4 ppm. Error bars indicate the resistance standard deviation between two temperature points. **e,** Voltage drop ΔV measured across the SQUID vs current bias I and magnetic flux (field) $\Phi(B_z)$. The periodicity of I_S as a function of B_z translates into a periodicity in the flux $\Phi = B_z A$ through the ring with an effective area $A \simeq 4.9\,\mu\text{m}^2$, consistent with the area estimated from Fig. 4.12 in the Additional material. **c** The green line is the best-fit of the SQUID critical current $I_S(\Phi)$ (Eq. 4.3) defined by the interface between the dissipationless (red area) and the dissipative regime (colored). **f,** Traces of $\Delta V(\Phi)$ from **e,** measured for two selected values of the current bias (below and above $2I_C$) which demonstrate the Φ_0-periodicity both in the dissipationless and in the dissipative regime. Data in **e** and **f** were recorded at a bath temperature of 50 mK.

This leads to a finite triple product in Eq. 4.2 and, consequently, to an anomalous φ_0 phase bias.

An Al-based superconducting quantum interference device (SQUID) is used as a phase-sensitive interferometer made with two φ_0-JJs (in red), as shown in Fig. 4.1b, c (see Additional material for fabrication detail). The device geometry has been conceived to maximize the symmetry of the two JJs [82] to accumulate the two anomalous φ_0-shifts when applying a uniform in-plane magnetic field. The anomalous phase shift in the SQUID critical current is then given by:

$$I_S(\Phi) = 2I_C \left| \cos\left(\pi \frac{\Phi}{\Phi_0} + \frac{\varphi_{tot}}{2} \right) \right|, \tag{4.3}$$

where I_C is the critical current of each JJ, Φ is the magnetic flux piercing the ring, $\varphi_{tot} = 2\varphi_0$ is the total anomalous phase shift in the SQUID interference pattern resulting from the φ_0-shifts in each JJs (see Section 4.6.5 of the Additional material for details), and $\Phi_0 = 2.067 \times 10^{-15}$ Wb is the flux quantum. This model provides a good description of the SQUID interference pattern displayed in Fig. 4.1e, which shows the voltage drop across the SQUID as a function of the out-of-plane magnetic field B_z and bias current I. The red-colored region of Fig. 4.1e, corresponding to zero-voltage drop, indicates the dissipationless superconducting regime and the edge of this region provides the $I_S(\Phi)$ dependence. The green line on top of the color plot is the best-fit of $I_S(\Phi)$ from Eq. 4.3, with $I_c \simeq 300$ nA and no phase-shift $\varphi_{tot} \simeq 0$. The latter condition is consistent with the absence of the anomalous phase when the magnetic field has only a component in $\hat{\mathbf{z}}$ direction and the magnetic impurities are not polarized (i.e. $\mathbf{n_h} \parallel \hat{\mathbf{z}}$ in Eq. 4.2). Notably, there is a replica of the $I_S(\Phi)$ oscillations in the voltage drop $\Delta V(\Phi)$ when $I > I_S$, and the SQUID operates in the dissipative regime (blue region and curve in Figs. 4.1e-f), as conventionally realized with strongly overdamped JJs [83]. This oscillation provides a complementary and fast method to quantify the SQUID phase shifts and is used in the following analysis. Additional measurements on similar devices can be found in Section 4.6.7 of the Additional material.

4.3. PHASE BATTERY

The temperature dependence of the device normal-state resistance shows an upturn below ~ 80 K (see Fig. 4.1d) which is a clear signature of the presence of magnetic impurities that increase, at low temperature, the electron scattering events. The upturn can be well fitted by the Kondo model (yellow line of Fig. 4.1d) for spin 1/2 of magnetic impurities with a density of ~ 4 ppm (see Section 4.6.2 of the Additional material for more details on the fitting procedure). The presence of these unpaired spins can be ascribed to the nanowire surface oxides, as already observed in undoped metal oxide nanostructures [84], even if defects in the nanowire crystalline structure [85] cannot be excluded a priori. Although, the amount of intrinsic magnetic impurities is not fully controllable, their presence is crucial for the operation and implementation of the phase battery, as discussed below.

Following the condition imposed by a finite Liftshitz invariant term (Eq. 4.2) we apply an in-plane magnetic field orthogonal to the nanowire axis (B_y) to maximize the effect. The $I_S(\Phi)$ dependence then evolves with a clear generation of an anomalous

phase shift, as presented in the panels of Fig. 4.2. The evolution of $\Delta V(\Phi)$ as a function of B_y ranging from −60 mT up to 60 mT is visible in Fig. 4.2a and in the selected single traces of Fig. 4.2b. The resulting phase-shift φ_{tot} exhibits a non-monotonic evolution as a function of B_y, with a maximum shift at $B_y \simeq 5$ mT and a saturation for $|B_y| \gtrsim 30$ mT (yellow curve in Fig. 4.2c). When the field is reversed, a hysteretic behavior is observed (green curve in Fig. 4.2c), and the evolution of φ_{tot} reverses with a minimum shift at $B_y \simeq -5$ mT. The change in sign of the phase-shift agrees with the theoretical prediction of Eq. 4.2 when $\mathbf{h} \to -\mathbf{h}$, whereas the observed hysteretic behavior suggests a ferromagnetic coupling between the magnetic impurities in the nanowire. Trivial hysteretic phase shifts induced by a trapped flux in the superconductor [86] or in the SQUID ring can be excluded (see Section 4.6.6 of the Additional material for more details). At low temperatures, the coexistence of Kondo effect and ferromagnetism is not unusual [84] and well describes the hysteretic non-monotonic behavior observed in $\varphi_{tot}(B_y)$. Indeed, due to the antiferromagnetic nature of the Kondo interaction, the effective exchange field created by these unpaired spins is opposite to the Zeeman field generated by B_y so that the two contributions are competing in the anomalous phase with a partial cancellation.

This additional component is confirmed by the observation of an *intrinsic* phase-shift, φ_{int}, which is present even in the absence of the in-plane magnetic field ($B_y = 0$) if a finite B_y has been previously applied, as shown in Figs. 4.2d and e. Since it stems from a ferromagnetic ordering, φ_{int} depends only on the history of B_y, and again, the evolution of $\varphi_{int}(B_y)$ can be extracted and is presented in Fig. 4.2f. In contrast to the total phase-shift, φ_{int} follows a clear and almost monotonic behavior which shows a hysteresis in the back and forth sweep direction (blue and red curves of Fig. 4.2f). φ_{int} saturates for $|B_y| \gtrsim 15$ mT in the two asymptotic limits with total phase drop of $\sim \pi$. Furthermore, during the first magnetization of the SQUID, a curve resembling the initial magnetization curve of a ferromagnet has been observed (see Fig. 4.5 in the Additional material), confirming the ferromagnetic nature of the impurity ensemble.

4.4. ANOMALOUS φ_0-PHASE

We now analyze the *extrinsic* contribution, φ_{ex}, to the phase shift which stems directly from the external B-field. Due to the additive nature of the anomalous phase in the exchange field h in Eq. 4.2, it is possible to extract from φ_{tot} the extrinsic contribution $\varphi_{ex} = \varphi_{tot} - \varphi_{int}$. This is depicted in Fig. 4.3a, where the evolution of φ_{ex} in B_y is shown. Here, the agreement between the back (blue) and forth (red) traces in B_y demonstrates implicitly the absence of any hysteresis ensuring the complete extraction of the intrinsic contribution. Notice also that the behavior of φ_{int} and φ_{ex} in the magnetic field is *opposite* in sign as expected from the competition between the exchange interactions induced by the Kondo antiferromagnetic coupling and a Zeeman field, further supporting our analysis. The dependence $\varphi_{ex}(B_y)$ is characterized by a linear increase at low magnetic fields ($|B_y| < 15$ mT) up to a maximum phase-shift of $\pm\pi/2$. Remarkably, our measurement reveals the *odd* parity of the anomalous phase with respect to the magnetic field, one of the main symmetry hallmarks of this effect [37, 53]. This parity is a consequence of the odd parity of the free energy F_L with respect to the exchange field. At higher fields, non-linearities appear suggesting a non-trivial evolution of φ_{ex} in mag-

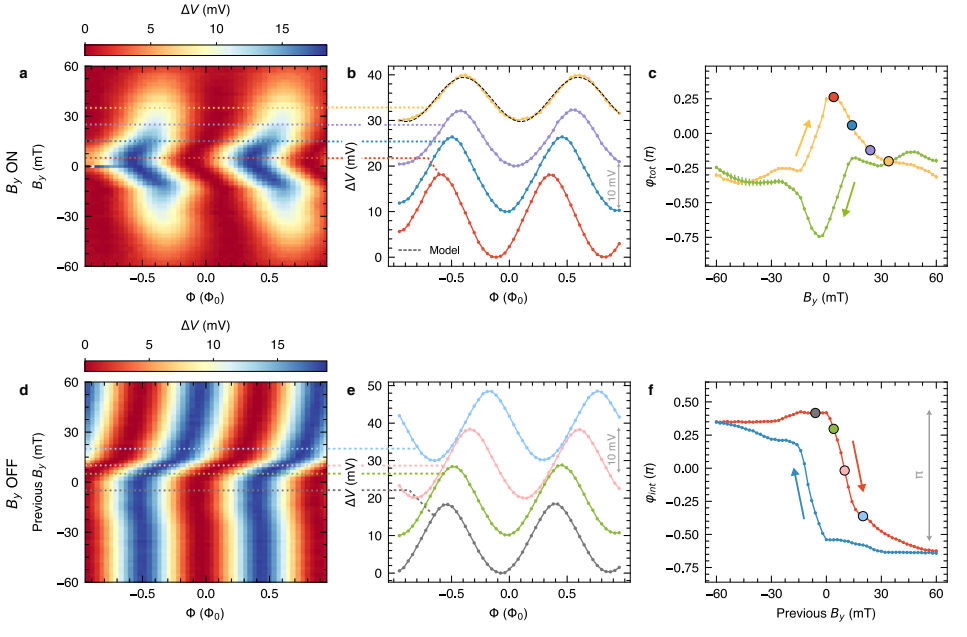

Figure 4.2: Charging loops of the Josephson phase battery. a, Voltage drop $\Delta V(\Phi)$ at constant current bias $I = 1\,\mu$A vs in-plane magnetic field B_y applied orthogonal to the nanowire axis. At large $|B_y|$, the amplitude of $\Delta V(\Phi)$ is lowered due to the suppression of superconductivity inside the wire. **b,** Selected traces $\Delta V(\Phi)$ extracted from **a** for different B_y. Data are vertically offset for clarity. **c,** Extracted phase shift φ_{tot} from the curves in **a** with back (green) and forth (yellow) sweeps in B_y. The shifts are extracted by comparing the single traces to the RSJ relation $\Delta V = \frac{R}{2}\sqrt{I^2 - 4I_C^2 \cos\left(\pi\Phi/\Phi_0 + \varphi_{tot}/2\right)^2}$ [83], see the dashed line in **b** which serves as an example. **d,** Color plot of the persistent voltage drop $\Delta V(\Phi)$ measured at $B_y = 0$ after the magnetic field was swept to the values shown on the y-axis. **e,** Selected traces of $\Delta V(\Phi)$ extracted from **d**. **f,** Intrinsic phase shift φ_{int} extracted from **d**. φ_{int} stems from the ferromagnetic polarization of the unpaired spins. Error bars in c and f indicate the 1σ standard errors resulting from the fit of the curves in b and e. All data were recorded at 50 mK of bath temperature.

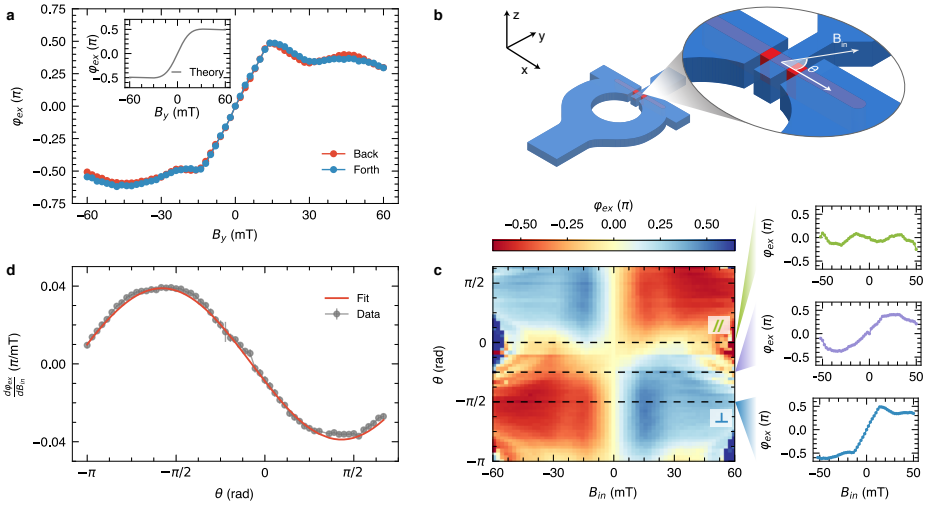

Figure 4.3: Vectorial symmetry of the anomalous phase φ_0. a, Dependence of the extrinsic anomalous phase φ_{ex} on B_y, showing an odd symmetry and non-hysteretic back and forth sweeps (blue and red traces). Inset: The $\varphi_{ex}(B_y)$ dependence obtained from the theoretical model (see Section 4.6.5 of the Additional material for details). **b,** Sketch of the interferometer with the reference axes of the in-plane magnetic field (B_{in}) and the angle θ with respect to the nanowire axis. **c,** Dependence of the anomalous phase φ_{ex} on θ and B_{in}. The single traces on the right show the behavior of φ_{ex} for a longitudinal $\theta = 0$ (green curve), canted $\theta = \pi/4$ (violet curve) and orthogonal field $\theta = \pi/2$ (blue curve). **d,** $d\varphi_{ex}/dB_{in}$ vs θ together with a sinusoidal fit (red curve) to Eq. 4.4. The slope has been evaluated by a linear fit of the data in **c** for $|B_{in}| < 10$ mT. The error bar is the 1σ standard error of the fit. All data were recorded at 50 mK of bath temperature.

netic field. In order to understand this behavior, we have modeled the φ_0-junction setup by a lateral junction treated within the quasi-classical approach presented in Ref. [37] (see Section 4.6.5). The resulting φ_0 obtained from the above model is shown in the inset of Fig. 4.3a. It nicely reproduces the main features of φ_{ex}: the linear dependence at small magnetic fields and the saturation at larger ones. Notice that, within the scale of the magnetic field applied in the experiment, the field dependence of the anomalous phase looks as if it saturates at a value close to $\pi/2$. This value is however non-universal and depends on the characteristics of the nanowire. Moreover, if larger values of B_{in} could be reached[1], the anomalous phase of each junction would increase up to the universal plateau at π, as expected also for planar junctions [37].

At small in-plane fields ($B_{in} = \sqrt{B_x^2 + B_y^2}$) the model leads to a simple expression for the anomalous phase:

$$\varphi_{ex} \simeq C_1 \alpha^3 B_{in} \sin(\theta) + O(B_{in}^3), \tag{4.4}$$

[1]Higher magnetic field values in our device result in the suppression of the interference pattern, as can be seen in Fig. 4.2a.

where θ is the angle between the field and the nanowire axis and C_1 is a parameter dependent on the temperature and the microscopic details of the JJ. By using typical values of the parameters for the InAs/Al junction we obtained $C_1 \approx 0.04\,\mathrm{rad\,mT^{-1}}$, in very good agreement with the experimental data (see Section 4.6.5).

The odd symmetry of the anomalous phase dictated by the triple product in Eq. 4.2 can be further investigated by measuring φ_{ex} over all directions of the in-plane magnetic field. Figure 4.3c shows the full dependence of φ_{ex} on the angle θ (see sketch in Fig. 4.3b). As predicted from Eq. 4.2, the phase-shift is very small for fields along the nanowire axis ($\theta = 0$, green trace in Fig. 4.3c), showing the maximum slope for an orthogonal magnetic field ($\theta = \pi/2$, blue trace in Fig. 4.3c). The odd symmetry manifests clearly as well in the slope $\frac{\partial \varphi_{ex}}{\partial B_{in}}$ in the low-field limit (Fig. 4.3d). The latter is perfectly fitted with a sinusoidal function of θ in agreement with Eq. 4.4 (red trace in Fig. 4.3d).

4.5. CONCLUSIONS

In summary, our results demonstrate the implementation of a quantum phase battery. This quantum element, providing a controllable and localized phase-bias, can find key applications in different quantum circuits such as energy tuner for superconducting flux [87] and hybrid [88] qubits, or persistent multi-valued phase-shifter for superconducting quantum memories [75, 89] as well as superconducting rectifiers [90]. Moreover, the magnetic control over the superconducting phase opens new avenues for advanced schemes of topological superconducting electronics [91] based on InAs JJs [78, 92]. The weak control over the density of unpaired spins makes our proof-of-concept device difficult to reproduce in a massive reliable process. Further technological improvements can be envisioned by a controlled doping of the wires with magnetic impurities [93] or by the inclusion of a thin epitaxial layer of a ferromagnetic insulator, like EuS [94], as recently integrated in similar nanowires [95].

4.6. ADDITIONAL MATERIAL

4.6.1. DEVICE FABRICATION

Hybrid proximity DC SQUIDs devices were fabricated starting from gold-catalyzed n-doped InAs nanowires with typical length of 1.5 µm and diameter of $\sim$ 85 nm grown by chemical beam epitaxy [96]. The n-doping was obtained with Se [97] and the metalorganic precursors for the nanowire growth were trimethylindium (TMIn), tertiarybutylarsine (TBAs), and ditertiarybutylselenide (DTSe), with line pressures of 0.6, 1.5, and 0.3 Torr, respectively. Nanowires were drop-casted onto a substrate consisting of 300 nm thick SiO_2 on p-doped Si. Afterwards, a 280 nm-thick layer of positive-tone Poly(methyl methacrylate) (PMMA) electron beam resist was spun onto the substrate. The devices were then manually aligned to the randomly distributed InAs nanowires and patterned by means of standard electron beam lithography (EBL) followed by electron beam evaporation (EBE) of superconducting Ti/Al (5/100nm) electrodes. Low-resistance Ohmic contacts between the superconducting leads and the InAs nanowires were promoted by exposing the InAs nanowire contact areas to a highly diluted ammonium polysolfide $(NH_4)S_x$ solution, which selectively removes the InAs native oxide and passivates the surface, prior to EBE. The fabrication process was finalized by dissolving the PMMA

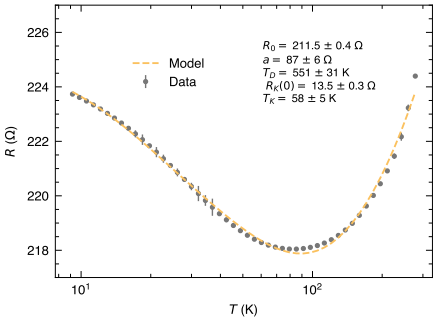

Figure 4.4: Kondo upturn in the resistance of the InAs nanowire. Resistance versus temperature $R(T)$ of one of the devices measured during the cooldown of the refrigerator showing a clear increase of resistance for temperatures below 80 K. This behavior is consistent with the Kondo scattering model as demonstrated by the good fit of the $R - T$ data with the model of Eq. 4.7.

layer in acetone.

From transport characterization on similar wires and normal metal electrodes [98], we estimate a typical electron concentration $n \simeq 2 \times 10^{18}$ cm^{-3} and mobility $\mu \simeq 1200$ cm^2/Vs. The corresponding Fermi velocity v_F, mean free path l_e, and diffusion coefficient $D = v_F l_e/3$, are evaluated to be $v_F \simeq 2 \times 10^6$ m/s, $l_e \simeq 30$ nm, and $D \simeq 200$ cm^2/s.

4.6.2. KONDO RESISTANCE $R(T)$

To quantify the amount of unpaired spins in our system the temperature dependence of the normal-state resistance $R(T)$ has been studied in the range 10 K to 300 K. The data exhibits an upturn at $T \sim 80$ K (see Fig. 4.4) suggesting a Kondo scattering mechanism between the free electrons and the unpaired spins in the weak-links. Since the InAs nanowires were synthesized without incorporating any magnetic impurity (to the best of our knowledge, Se doping cannot provide by itself any magnetism), we conjecture that unpaired spins are originated from oxides states at the nanowire surface, in analogy with what is observed in metallic nanowires [84, 99]. Indeed, the $R(T)$ of a diluted magnetic alloy follows the universal non-monotonic relation [100]

$$R(T) = R_0 + R_{el-ph}(T) + R_K(T), \tag{4.5}$$

where R_0 is the residual resistance while $R_{el-ph}(T)$ and $R_K(T)$ are the contribution given respectively by the electron-phonon and the Kondo scattering. The temperature dependence of the former can be expressed according to the Bloch-Grüneisen model as [101]

$$R_{el-ph}(T) = a \left(\frac{T}{\theta_D}\right)^5 \int_0^{\theta_D/T} \frac{x^5}{(e^x - 1)(1 - e^{-x})} \mathrm{d}x. \tag{4.6}$$

For the Kondo contribution, many analytical approximations are available according to the range of temperature investigated. In the full range of temperature, the exact solution

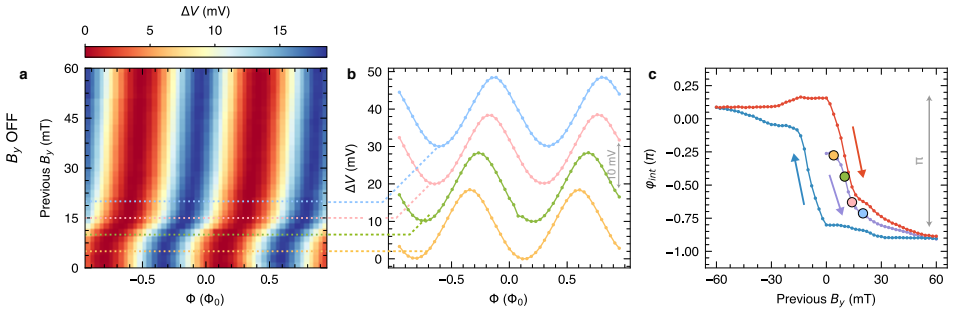

Figure 4.5: First magnetization curve of φ_{int}. **a**, Color plot of the voltage drop $\Delta V(\Phi)$ measured at $B_y = 0$ after the magnetic field was swept to the values shown on the y-axis straight after the thermal cycle. **b**, Selected traces $\Delta V(\Phi)$ corresponding to the cuts in **a**. **c**, Intrinsic phase shift φ_{int} extracted from **b**, showing the first polarization of the unpaired spins (violet curve) and the hysteresis loop followed in the subsequent back and forth sweeps of B_y, blue and red curves, respectively.

is obtained from the numerical renormalization group theory (NRG). In the following we use an empirical fitting function derived as an analytical approximation of the NRG given by [102–105]

$$R_K^{NRG} = R_K(0)\left(\frac{T_K'^2}{T^2 + T_K'^2}\right)^s, \tag{4.7}$$

with T_K' related to the actual Kondo temperature T_K by $T_K' = T_K/(2^{1/s} - 1)^{1/2}$. Note that Eq. 4.7 is defined such that $R_K(T_K) = R_K(0)/2$, and the parameter s is fixed to $s = 0.22$ as expected for a spin $1/2$ impurity. In Fig. 4.4 we show the fit of the experimental data with Eq. 4.7, from which we extract a Kondo temperature $T_K = 58 \pm 5$ K, a residual magnetic impurity resistance $R_K(0) = 13.5 \pm 0.3\ \Omega$, a coefficient $a = 87 \pm 6\ \Omega$, and a Debye temperature $\theta_D = 551 \pm 31$ K. From $R_K(0)$ it is possible to estimate the density of unpaired spins, that from the Hamann expression of the residual Kondo resistance in the unitary limit is given by [106]

$$R_K(0) = \frac{L}{A}\frac{4\pi c\hbar}{n k_F e^2}, \tag{4.8}$$

with $L \sim 80$ nm junction lenghts, $A \sim \pi r^2$ with $r \sim 45$ nm nanowire cross-sectional area, k_F Fermi wavevector and n electron carrier density, from which we estimate the density of magnetic impurities $c \simeq 1.36 \times 10^{17}$ cm^{-3}. This corresponds to a concentration of ~ 4 ppm ($= c/n_{InAs}$, with the InAs atomic density $n_{InAs} = 3.59 \times 10^{22}$ cm^{-3}) of unpaired spins in the InAs nanowire.

4.6.3. FIRST "MAGNETIZATION" CURVE

The persistent hysteretic loops of the φ_0-shift, shown in Fig. 4.1d-f, are consistent with the presence of a ferromagnetic background of unpaired spin. To support this hypothesis, we show in Fig. 4.5a and b the first magnetization curve of this spin ensemble measured in the same device. Initially, the magnetization of the sample is lifted by warming

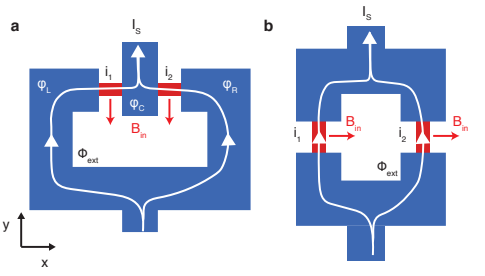

Figure 4.6: Comparison between SQUID geometries. The SQUID geometry employed in this work **a** allows a simple readout of the anomalous phase φ_{tot} generated by a uniform magnetic field B_{in} due the opposite direction of the supercurrents in the two JJs. This would not be possible in a conventional geometry as the one shown in **b**.

the system above 3 K. Then, the SQUID voltage drop $\Delta V(\Phi)$ is measured in the absence of an in-plane magnetic field B_y which is then gradually turned on thus polarizing the unpaired spins. The resulting $\Delta V(\Phi)$ shows no shifts at low B_y while, only above 5 mT a clear shift is generated. The resulting φ_{int} extracted by fitting $\Delta V(\Phi)$ is shown in the violet curve of Fig. 4.5c. By reversing B_y the φ_{int} then evolves to the hysteretic curve typical of a ferromagnetic system (blue and red curves in Fig. 4.5c).

4.6.4. SQUID WITH ANOMALOUS JOSEPHSON JUNCTIONS

The critical current of a SQUID interferometer can be evaluated from the CPR of the two JJs forming the interferometer. Using a sinusoidal CPR, the currents through the two junctions can be written as

$$i_1 = I_c \sin\left[(\varphi_C - \varphi_L) + \varphi_0^{(1)}\right] \qquad i_2 = I_c \sin\left[(\varphi_C - \varphi_R) + \varphi_0^{(2)}\right], \tag{4.9}$$

where $\varphi_L, \varphi_C, \varphi_R$ are the left,central and right superconducting phases and I_c is the critical current of each JJ (assumed to be equal).

The supercurrent of the SQUID is the sum of the two contributions ($I_s = i_1 + i_2$,) and, with the constraint on the superconducting phases of the flux quantization

$$(\varphi_L - \varphi_C) + (\varphi_C - \varphi_R) + 2\pi\frac{\Phi}{\Phi_0} = 2\pi \text{ (mod n)}, \tag{4.10}$$

it has the form

$$I_s = 2I_C \sin(\delta_0) \cos\left[\frac{1}{2}\left(2\pi\frac{\Phi}{\Phi_0} + \varphi_{tot}\right)\right], \tag{4.11}$$

where $\delta_0 = \varphi_C - \frac{\varphi_L+\varphi_R}{2} + \frac{(\varphi_0^{(2)}+\varphi_0^{(1)})}{2}$ and $\varphi_{tot} = \varphi_0^{(2)} - \varphi_0^{(1)}$ the total anomalous phase accumulated in the interferometer. With the geometry depicted in Fig. 4.6a, the two junctions experience the same in-plane magnetic field orientation but the supercurrents flow in opposite directions, resulting in $\varphi_0^{(2)} = -\varphi_0^{(1)} = \varphi_0$ and $\varphi_{tot} = 2\varphi_0$. The stable configuration of the SQUID is achieved by minimizing the total Josephson free energy

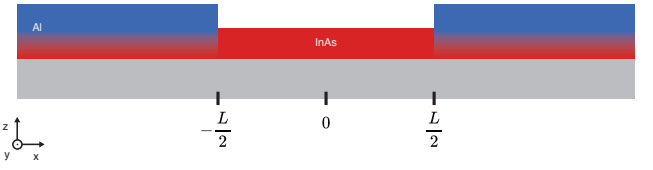

Figure 4.7: Schematic view of the S-N-S junctions. At $|x| > L/2$, the InAs nanowire (red region) is partially covered by the Al superconducting leads (dark blue regions). The gray region corresponds to the substrate. This schematic view corresponds to the z-x plane of Fig. 4.3b (top panel).

obtained at $\delta_0 = \pi/2$, and then the maximum sustainable supercurrent results to be

$$I_S(\Phi) = 2I_C \left| \cos\left(\pi \frac{\Phi}{\Phi_0} + \frac{\varphi_{tot}}{2}\right)\right|. \tag{4.12}$$

It follows that in the absence of magnetic flux, the maximum supercurrent is reduced by a factor $\sim |\cos(\varphi_{tot}/2)|$ compared to the non-anomalous case as a consequence of the anomalous supercurrent already present in the interferometer. In a more conventional geometry such as the one shown in Fig. 4.6b, the anomalous phases acquired by the two junctions would be the same $\varphi_0^{(1)} = \varphi_0^{(2)} = \varphi_0$, making its detection impossible in the phase-to-current readout mode employed in the present work.

4.6.5. THEORY OF LATERAL φ_0-JUNCTION

The origin of the anomalous phase φ_0 is the singlet-triplet conversion mediated by the spin-orbit coupling (SOC), which in the normal state corresponds to the charge-spin conversion [37]. The calculations of the anomalous Josephson current in φ_0-junctions have been done for ideal planar S-N-S junctions, in which the superconducting electrodes and the normal region with SOC are separated by sharp boundaries [37, 53, 107], where the singlet-triplet coupling takes place only in the N region. As shown in Ref. [37], this assumption leads to a monotonical increase in the anomalous phase φ_0 as a function of the applied magnetic field, which contrasts with curves extracted from our experiment (see Fig. 4.3a). It is however clear that our experimental setup (Fig. 4.1) differs from an ideal S-N-S junction. Indeed, in each junction, the superconducting leads are covering part of the wire over distances larger than the coherence length. This means that the SOC, and hence the spin-charge conversion, is also finite in the portion of the wire covered by the superconductor. As we will show in this section, this feature is essential to understand the experimental findings; in particular, the dependence of φ_0 on the external magnetic field. In this calculation, we focus on the dependence of φ_0 on the y direction of the field, i.e., B_{in} at $\theta = \pi/2$ (see Figs. 4.3a and b).

To be specific, we consider the junction sketched in Fig. 4.7. We assume an infinite diffusive quasi-one dimensional nanowire along the x-axis, which is partially covered by two semi-infinite Al superconducting leads at $x < L/2$ and $x > L/2$. We assume, for simplicity, that the proximity effect is weak and that the wire is diffusive. In such a case, the condensate function, which determines the Josephson current, obeys the linearized

Usadel equation, which results in two coupled differential equations for the singlet and triplet components, as shown in Ref. [37]. Because the wire lies on a substrate, the system has an uniaxial asymmetry in the z direction perpendicular to the substrate (see Fig. 4.7). In the presence of SOC, this allows for a gradient in singlet-triplet coupling generated by a differential operator of the form $C_k^a \partial_k \sim (\hat{z} \times \nabla)^a$, which converts a scalar (the singlet) into a pseudovector (the triplet) and vice-versa [37, 107]. We consider the case when the external field is applied in the y direction, and hence the superconducting condensate function has the form $f = f_s + i f_t \mathrm{sgn}\omega \sigma^y$, where $f_{s,t}$ are the singlet and triplet components and ω the Matsubara frequency. The linearized Usadel equation reads:

$$\begin{aligned} \frac{D}{2}\nabla^2 f_s - |\omega| f_s + (h - iD\kappa_{\mathrm{sc}}\partial_x) f_t = 0 \,, \\ \frac{D}{2}\nabla^2 f_t - |\omega| f_t - (h - 2iD\kappa_{\mathrm{sc}}\partial_x) f_s = 0 \,. \end{aligned} \tag{4.13}$$

Here D is the diffusion coefficient and $h = \mu_{\mathrm{B}} g_{\mathrm{s}} B_{\mathrm{in}}/2$ is the Zeeman field. The last term in both equations describes the spin-charge conversion due to the SOC. It is proportional to the effective inverse length κ_{sc} and the spatial variation of the condensate in the direction of the wire axis. The form of this term is determined by the uniaxial anisotropy of the setup in combination with the fact that we assume that the field is applied only in y direction.

Equation 4.13 is written for the full 3D geometry. To obtain an effective 1D Usadel equation, we integrate Eq. 4.13 over the wire cross-section and use boundary conditions imposed on the condensate function at the surface of the wire. In the part of the wire which is covered by the superconductor, the interface between the wire and the superconductor is described by the linearized Kupryianov-Lukichev boundary condition:

$$\partial_x f_s|_{\mathrm{InAs/Al}} = \gamma f_{\mathrm{BCS}} e^{i\phi}, \tag{4.14}$$

where γ is a parameter describing the InAs/Al interface, $f_{\mathrm{BCS}} = \Delta/\sqrt{\omega^2 + \Delta^2}$ is the BCS bulk anomalous Green's function in the superconducting leads, and ϕ is the phase of the corresponding lead. In the uncovered parts of the wire, we impose a zero current flow which corresponds to $\partial_x f_{s/t}\big|_{\mathrm{InAs/vac.}} = 0$. The integration of Eq. 4.13 over the cross-section of the wire results in two coupled equations for the singlet and triplet components:

$$\begin{aligned} \partial_x^2 f_s - \kappa_\omega^2 f_s + \left(\kappa_h^2 - 2i\kappa_{\mathrm{sc}}\partial_x\right) f_t = S(x) \,, \\ \partial_x^2 f_t - \kappa_\omega^2 f_t - \left(\kappa_h^2 - 2i\kappa_{\mathrm{sc}}\partial_x\right) f_s = 0 \,, \end{aligned} \tag{4.15}$$

with

$$S(x) = \gamma f_{\mathrm{BCS}} \left[\Theta\left(x - \frac{L}{2}\right) e^{i\frac{\varphi}{2}} + \Theta\left(-x - \frac{L}{2}\right) e^{-i\frac{\varphi}{2}}\right] \,, \tag{4.16}$$

$\kappa_\omega^2 = \frac{2|\omega|}{D}$, $\kappa_h^2 = \frac{2h}{\hbar D}$, and φ the phase difference between the two Al leads. After a cumbersome but straightforward procedure, we solve Eq. 4.15 for continuous and finite

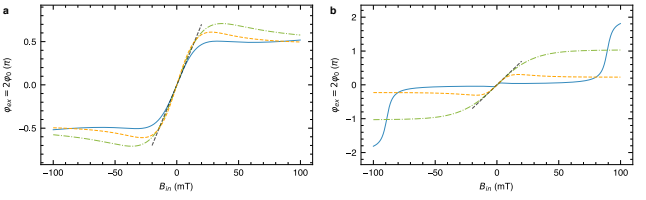

Figure 4.8: Theoretical model for the extrinsic anomalous phase. The dependence of the extrinsic anomalous phase on magnetic field applied in y direction (B_{in} at $\theta = \pi/2$) for a) different temperatures, with $\alpha \simeq 0.24$ eV Å, and (b) for different values of α, with $T \simeq 10$ mK. In (a), the solid blue line coincides with the one shown in Fig. 4.3a, with $T \simeq 25$ mK and $g_s \simeq 12$. For the dashed orange line, we choose $T \simeq 10$ mK and $g_s \simeq 5$, and for the dashed-dotted line, $T \simeq 5$ mK and $g_s \simeq 2$. In (b), the solid blue line corresponds to $\alpha \simeq 0.1$ eV Å and $g_s \simeq 37$, the dashed orange line to $\alpha \simeq 0.18$ eV Å and $g_s \simeq 7$, and the dashed-dotted green line to $\alpha \simeq 0.4$ eV Å and $g_s \simeq 3$. In both (a) and (b), the dashed grey line corresponds to the measured slope at low fields.

$f_{s,t}$. From the knowledge of the singlet and triplet components one determines the Josephson current as follows [37]:

$$j(x) = \frac{\pi\sigma_D T}{e} \sum_\omega \mathbb{I}\mathrm{m}\{f_s^* \partial_x f_s - f_t^* \partial_x f_t - i\kappa_{sc}\,(f_s^* f_t + f_s f_t^*)\}\,. \tag{4.17}$$

The resulting current can be written as $j = I_c \sin(\varphi + \varphi_0)$, with the anomalous-phase given by:

$$\varphi_0 = \arctan\left\{ \frac{\sum_\omega \mathbb{I}\mathrm{m}\left\{ f_{BCS}^2 e^{-qL} \frac{\sinh(\kappa_{sc}L)(q^2+\kappa_{sc}^2)+2q\kappa_{sc}\cosh(\kappa_{sc}L)}{q(q^2-\kappa_{sc}^2)^2} \right\}}{\sum_\omega \mathbb{R}\mathrm{e}\left\{ f_{BCS}^2 e^{-q^*L} \frac{\cosh(\kappa_{sc}L)(q^{*2}+\kappa_{sc}^2)+2q^*\kappa_{sc}\sinh(\kappa_{sc}L)}{q^*(q^{*2}-\kappa_{sc}^2)^2} \right\}} \right\}\,, \tag{4.18}$$

where $q^2 = \kappa_\omega^2 + \kappa_{sc}^2 - i\kappa_h^2$. In order to compare with the experimental data, we assume a Rashba-like SOC and use the expression derived in Ref. [37] for the spin-charge coupling parameter, namely $\kappa_{sc} = 2\tau\alpha^3 m^{*2}/\hbar^5$. By using typical values for the parameters of a InAs/Al system: $\xi_0 \simeq 100$ nm, $\Delta \simeq 150$ μeV, $m^* = 0.023\ m_e$, $T \simeq 25$ mK, $g_s \simeq 12$, and $\alpha \simeq 0.24$ eV Å, we find the $\varphi_0(B_{in})$ dependence corresponding to the one shown in Fig. 4.3a. We see that our model provides a good qualitative explanation of the two main observed features. Namely, the linear increase of φ_0 for small fields and a kind of saturation at $\varphi_0 \approx \pm 0.5\pi$.

In Fig. 4.8, we show different $\varphi_0(B_{in})$ curves obtained from the general expression 4.18. Whereas for small fields the experimental slope (dashed grey line) can be obtained with various parameters sets, the behaviour of φ_0 at larger fields depends strongly on these parameters.

Indeed, it is important to emphasize that the saturation value at $\varphi_0 \approx \pm 0.5\pi$ is not an universal property of the phase-battery. This value depends on the intrinsic properties of the system. In particular, larger values α of the SOI leads to larger values of φ_{ex} at values of the field larger than those accessed in the experiment. This is shown in Fig. 4.8b, where we plot the $\varphi_0(B_{in})$ dependence for different values of α, with $T \simeq 10$ mK. In

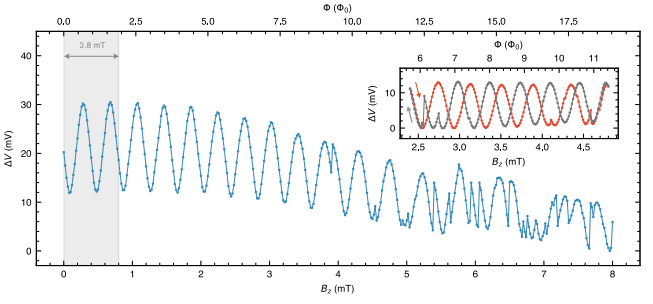

Figure 4.9: Fluxon-induced phase shifts at high B_z. Voltage drop $\Delta V(B_z)$ across the SQUID for $I_{sd} = 1\,\mu$A versus applied magnetic field B_z up to 8 mT recorded at $T = 100$ mK. The grey area indicated in the plot (corresponding to $0 \leq B_z \leq 0.8$ mT) is the one used to track and evaluate the induced phase shift in our interferometer. For $B_z \gtrsim 3$ mT, abrupt jumps in the phase start to appear due to trapped fluxons piercing the SQUID area. Inset: back (gray) and forth (red) traces at high B_z in the same conditions as before show an hysteretic behavior which is expected for fluxons pick-up.

Fig. 4.8a, we change the g_s value to maintain the experimental slope in the low-field region. The linear behavior for the low-field region is shared by all $\varphi_0(B_{in})$ curves, as shown in Fig. 4.8. In this regime, we can thus find the slope value by linearizing Eq. 4.18:

$$\varphi_0 \simeq C_1 B_{in} + O(B_{in}^3), \tag{4.19}$$

with $C_1 \simeq 0.035\,\text{rad}\,\text{mT}^{-1}$, which is in good agreement with the value extracted from the experiment.

4.6.6. TRIVIAL MECHANISMS TO INDUCE PHASE SHIFTS

Trivial hypotheses, alternative to the anomalous φ_0 effect, have been also considered for the generation of a hysteretic phase shift: trapped magnetic fluxes and Abrikosov vortices.

- Trapped magnetic fluxes can be observed in superconducting loops with a non-negligible ring inductance L and, more precisely, for a screening parameter $\beta_L = \frac{2\pi L I_c}{\Phi_0} \gtrsim 1$, with I_C the critical current of a single junction [83]. This indeed can lead to a hysteretic behavior due to the presence of a circulating current in the ring. For our interferometer we estimated $\beta_L \lesssim 10^{-2}$ ($I_C \sim 300$ nA and $L \sim 10$ pH [108]) that is very unlikely to induce any magnetic hysteresis. Still, if circulating currents are present, hysteretic jumps should be sharp, periodic, and visible even at low B_z. The absence of any hysteretic behavior at low magnetic field is further confirmed by the continuous interference patterns shown in Fig. 4.1e and 4.1f.

- Abrikosov vortices, also known as fluxons, can be often induced in type-II superconductors – like the thin Al film used in our SQUID devices – when an out-of-plane magnetic field is applied. To avoid vortex intrusion into the ring surface,

which might induce a parasitic phase shift, we limit our out-of-plane component to $|B_z| < 0.8\,\mathrm{mT}$, which guarantees the absence of any fluxon. Indeed, upon the application of a larger field $B_z \gtrsim (3-4)$ mT, also in our case abrupt phase shifts appear with a density that increases by increasing B_z, as shown in Fig. 4.9.

This is what is expected for fluxons pinning in the Al, i.e., stochastic and abrupt events providing a discrete jump of the phase [86]. Notice also the hysteretic behavior expected for fluxon inclusion, which is underlined in the inset of Fig. 4.9 showing a local back and forth measurement.

With respect to the in-plane magnetic fields, the thickness of the Al film (thinner than the superconducting coherence length) ensures the complete penetration of the magnetic field, and thereby the absence of generated fluxons. This is consistent with the lack of any stochastic shift upon the application of B_{in}.

4.6.7. SUPPLEMENTARY DEVICE MEASURED

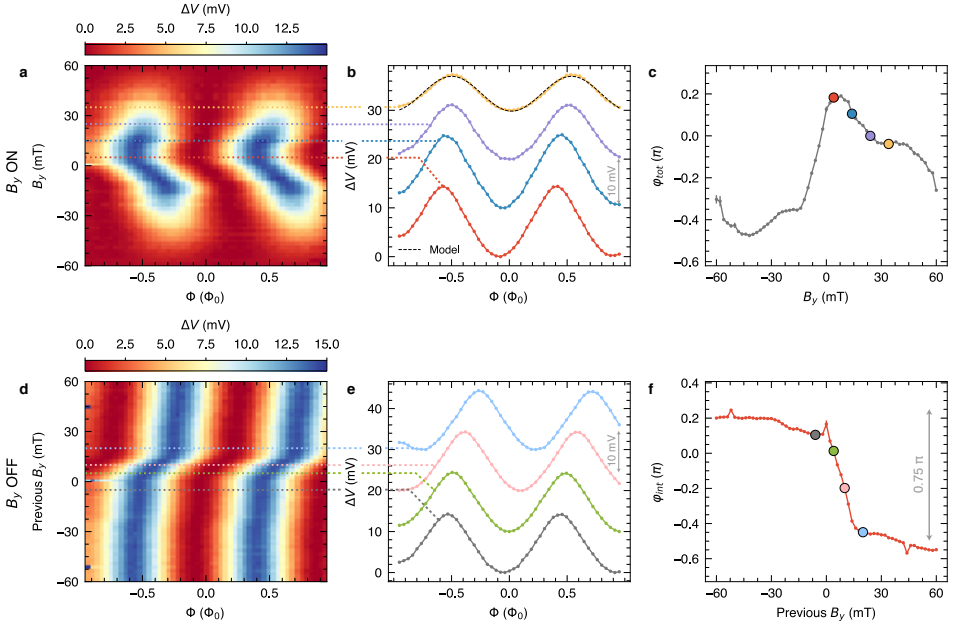

Figure 4.10: Charging loops of the Josephson phase battery (second device). a, Voltage drop $\Delta V(\Phi)$ at constant current bias $I = 1\,\mu\mathrm{A}$ versus in-plane magnetic field B_y applied orthogonal to the nanowire axis . At large $|B_y|$, the amplitude of $\Delta V(\Phi)$ is lowered due to the suppression of superconductivity inside the wire. **b,** Selected traces $\Delta V(\Phi)$ extracted from **a** for different B_y. Data are vertically offset for clarity. **c,** Extracted phase shift φ_{tot} from the curves in **a**. **d,** Color plot of the persistent voltage drop $\Delta V(\Phi)$ measured at $B_y = 0$ after the magnetic field was swept to the values shown on the y-axis. **e,** Selected traces $\Delta V(\Phi)$ corresponding to the cuts in **d**. **f,** Intrinsic phase shift φ_{int} extracted from **d**. φ_{int} stems from the ferromagnetic polarization of magnetic impurities. All data were recorded at 30 mK of bath temperature.

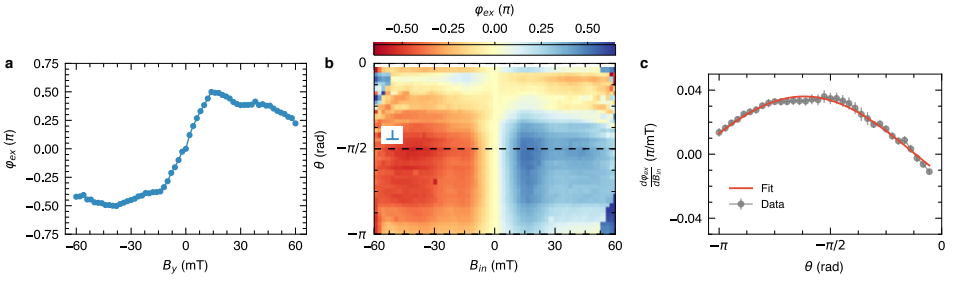

Figure 4.11: Vectorial symmetry of the anomalous phase φ_0 (second device). **a,** Dependence of the extrinsic anomalous phase φ_{ex} with B_y. **b,** Evolution of the anomalous phase φ_{ex} on θ and B_{in}. **c,** $d\varphi_{ex}/dB_{in}$ versus θ together with a sinusoidal fit (red curve) to Eq. 4.19. The slope has been evaluated by a linear fit of the data in **b** for $|B_{in}| < 10\,\mathrm{mT}$. The error bars are the RMS of the fit. All data were recorded at 30 mK of bath temperature.

In this section we repeated the same magnetic characterization of the Josephson phase battery shown in Fig. 4.2 and 4.3, performed on a different device to demonstrate the high reproducibility of the effect, apart sample-specific details. Notice that the behaviour of φ_{tot} and φ_{int} (Fig. 4.10) is qualitatively similar, but with a smaller total phase shift of $\sim 0.4\pi$ stemming from a weaker exchange interaction induced by the unpaired-spin. Moreover, the angle dependence of $\varphi_{ex}(\theta)$ shown in Fig. 4.11 is in very good agreement with the evolution observed in Fig. 4.2 and expected from the model presented in Section 4.6.5.

4.6.8. Low magnification SEM image of the device

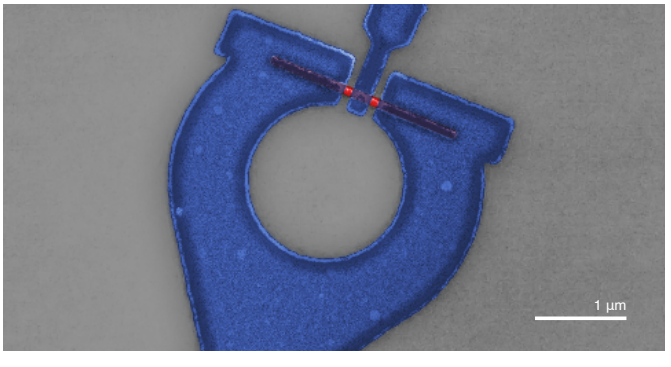

Figure 4.12: Low magnification SEM image of the device. As shown in Fig. 4.1c.

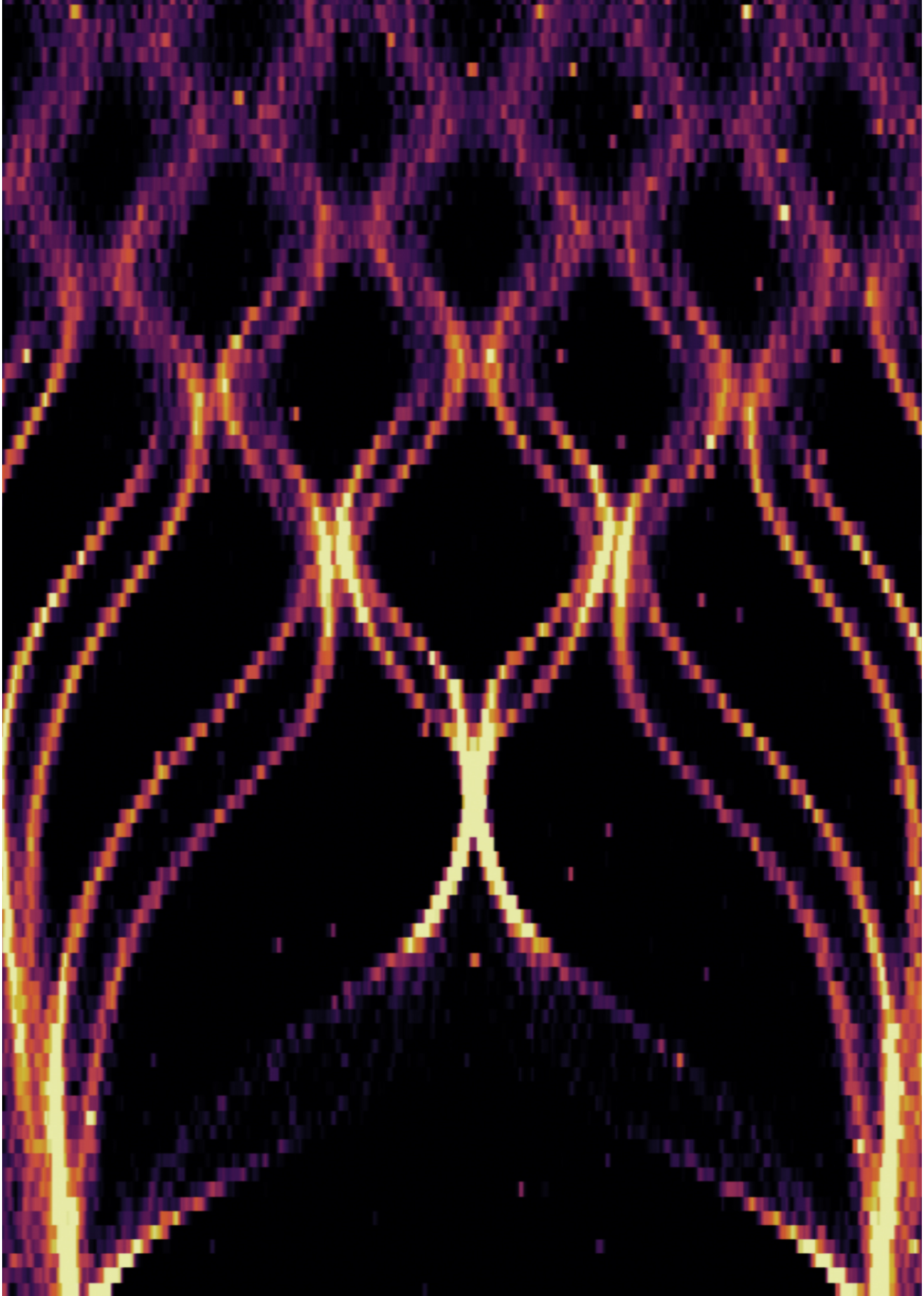

5

Half-integer Shapiro steps in InSb Josephson junctions

5.1. Introduction

The advancing quantum technologies have made the investigation of low-dimensional hybrid superconducting nanostructures a major area of research in recent years. When a normal conductor is coupled to a superconductor, the superconducting correlations can penetrate into the non-superconducting region through the proximity effect [109, 110]. As a result, the hybrid system can exhibit unique properties derived from both the normal and superconducting components, offering exciting possibilities for novel functionalities. This phenomenon has been investigated in various solid-state platforms, including semiconductors [31, 111], two-dimensional electron systems [46, 112, 113], magnetic and ferroelectric materials [114, 115] and topological insulators [116–118]. In this context, Indium Antimonide (InSb) is a particularly promising semiconductor, known for its high electron mobility, narrow bandgap, strong Rashba spin-orbit coupling, and large g^*-factor [46, 119–122]. Due to the challenges of growing InSb quantum wells on insulating substrates, free-standing InSb nanoflags have emerged as a highly flexible platform, as they can be grown without defects on lattice-mismatched substrates [123–134]. They have also been referred to as nanoflakes, nanosheets, or nanosails in the literature [124–126, 135]. Recently, InSb nanoflags have been used to realize proximity-induced superconductor-normal conductor-superconductor (SNS) Josephson junctions, which exhibit ballistic and gate-tunable supercurrents [127, 136, 137], clear subharmonic gap structures [128, 136], and non-local and non-reciprocal supercurrent transport [125, 137]. These developments highlight the potential of InSb nanoflags as a platform for exploring the complex dynamics between charge, spin, and superconducting correlations, including topological superconductivity [138, 139], gate-tunable hybrid superconducting qubits [32, 140, 141], and non-equilibrium quasiparticle dynamics [141–143].

In this work, we present a thorough investigation of highly transmissive ballistic Josephson junctions on InSb nanoflags made with niobium (Nb) contacts. Compared to previous works [136, 137], our device has a higher junction transparency, which enables

the investigation of unexplored transport regimes. Our findings reveal the coexistence of parallel short and long conducting channels, as confirmed by the temperature dependence of the critical current and magnetoresistance. Under microwave irradiation, we observe Shapiro steps at half-integer values of the canonical voltage $hf/2e$, which exhibit a non-monotonic evolution with temperature. The observation suggests that a non-equilibrium state is formed in the junction due to the microwave drive.

5.2. DEVICE CHARACTERIZATION

The device depicted in Figure 5.1a and 5.1b consists of a planar SNS junction made of an InSb nanoflag with two Nb contacts. Previous studies have revealed that these InSb nanoflags are defect–free and exhibit a zincblende structure with high mobility (up to 29 500 cm V^{-2} s^{-1}) and a mean free path $l_e \simeq 500$ nm at 4.2 K [134]. The Fermi wavelength $\lambda_F \simeq 30$ nm for a carrier concentration of $n_s \simeq 8.5 \times 10^{11}$ cm^{-2} is comparable to the thickness of the nanoflags ($\simeq 100$ nm), resulting in a strong quasi two-dimensional character. Measurements were performed using a standard four-wire technique at the base temperature of $T = 75$ mK of a dilution refrigerator. A highly doped Si backgate allows for control of the carrier density of the InSb and was set to $V_G = 40$ V for the results shown in the following. Microwave signals are applied via an open-ended attenuated coaxial cable placed ~ 1 cm away from the chip surface. The junction dynamics is modeled using an extended resistively and capacitively shunted junction (RCSJ) model, which takes into account the dissipative environment surrounding the junction, as depicted in Fig. 5.1c [28, 31, 145]. Further information on materials, fabrication, and measurement techniques can be found in the Additional material.

We first characterize the device in the absence of microwave irradiation. A typical back and forth sweep $V(I)$ is presented in the inset of Figure 5.1d, in which a current bias I is applied and the resulting voltage drop V across the junction is measured. The $V(I)$ characteristics shows a considerable hysteresis with a switching current $I_{sw} \simeq$ 170 nA and a retrapping current $I_{rt} \simeq 30$ nA. The hysteresis in planar SNS junctions is commonly due to electronic heating in the normal region [18], with a finite junction capacitance C_j potentially contributing [1]. Additional contributions to the hysteresis can arise from the cross-capacitance of the bonding pads via the backgate electrode, resulting in the underdamping of the junction [149, 150].

Figure 5.1d shows the temperature dependence of the switching and retrapping currents on a semi-log scale. We can distinguish two distinct regions in the data. For temperatures $T > T^*$, with $T^* \sim 500$ mK (see Figure 5.1d), the switching current follows the predictions of a short junction model (shown as a red shaded area). However, for $T \leq T^*$, we see a deviation from the short junction behavior, and the switching current follows an exponential increase with decreasing T, which is characteristic of long junctions (blue shaded area). The data can be well-reproduced over the entire temperature range using a simple model that considers the transport predominantly determined by two conducting channels, long and short, as illustrated in Figure 5.1b and demonstrated by the green line in Figure 5.1d. The coincidence of the separation of switching and retrapping currents occurring approximately at T^* is purely coincidental.

[1] In our device, the geometric junction capacitance is estimated $\sim$ aF, which may not cause a noticeable hysteresis, but intrinsic capacitance effects cannot be ruled out [146–148]

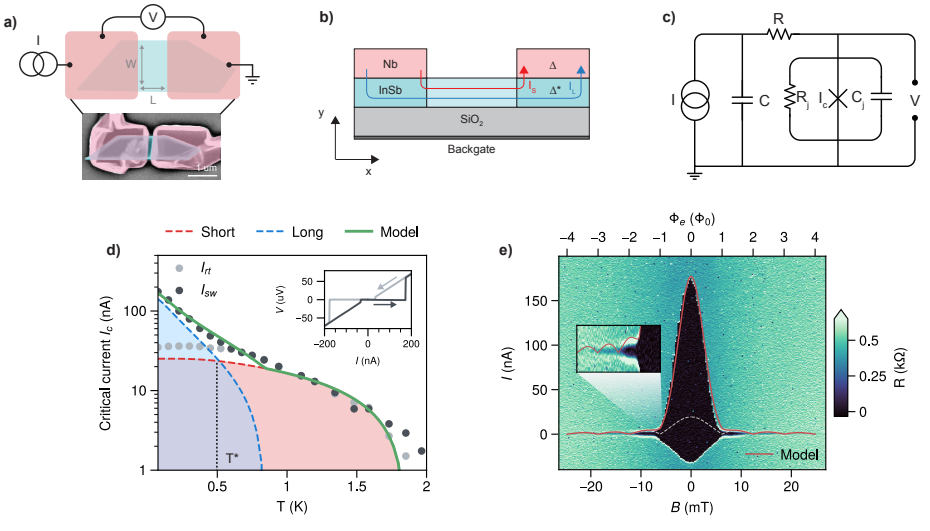

Figure 5.1: (a) Upper part: sketch of the sample with the relevant dimensions and a simplified measurement setup. The junction length is $L = 80\,\text{nm}$ and the width is $W = 650\,\text{nm}$. Lower part: scanning electron micrograph of the SNS junction. The InSb nanoflag has a trapezoidal shape, and the Nb contacts are patterned on top of it. (b) Schematic cross-section of the device, where the superconducting Nb contacts with gap Δ proximitize an induced gap Δ^* in the InSb layer [144]. The red and blue lines represent, respectively, the short and long conducting channels that are discussed in (d). (c) Extended RCSJ model, with the Josephson junction of critical current I_c in parallel with a shunt resistance R_j and capacitance C_j. Additional shunt capacitance C and resistor R take into account the dissipative environment around the junction. (d) Temperature dependence of the switching current I_{sw} (black dots) and the retrapping current I_{rt} (grey dots). The blue and red areas indicate the contributions of the long and short conducting channels, respectively, as estimated from the corresponding models. The green line represents the sum of the two contributions. Inset: forward (black line) and backward (grey line) current sweeps used to extract the switching I_{sw} and retrapping I_{rt} currents, respectively. (e) Differential resistance $R = dV/dI$ plotted as a function of the bias current I and the out-of-plane magnetic field B. The red curve takes into account both the long and short model contributions. The grey line shows the Fraunhofer pattern resulting from the short channel only. The inset provides a zoomed-in view of lobes in the low-bias region.

In the short junction limit $L \ll \xi_N$ (where $\xi_N = \hbar v_F/\Delta \simeq 720$ nm is the coherence length, with $v_F \simeq 1.5 \times 10^6$ m/s [134] and $\Delta = 1.764 k_B T_c \simeq 1.35$ meV, with $T_c \simeq 8.9$ K being the Nb critical temperature), the supercurrent flows directly through the InSb region between the Nb contacts separated by $L = 80$ nm. For simplicity, we assume that all modes in the junction have equal effective transmission τ, which can be described in the ballistic limit ($L \ll l_e$) by [5]:

$$I_S(T) = \max_{\varphi} \frac{\overline{N} e \Delta^{*^2}(T)}{2\hbar} \frac{\tau \sin\varphi}{E_A(\varphi, T)} \tanh \frac{E_A(\varphi, T)}{2k_B T}, \tag{5.1}$$

with $\overline{N}$ the number of effective modes, $E_A(\varphi, T) = \Delta^*(T)\sqrt{1 - \tau \sin^2(\varphi/2)}$ the Andreev bound state (ABS) energy of the mode, $\Delta^*(T) = \Delta^* \tanh\left(1.74\sqrt{T_c^*/T - 1}\right)$ the temperature-dependent induced energy gap[2], and φ the macroscopic phase-difference across the junction. The best fit with the short junction model yields the red dashed line in Figure 5.1d, with a single mode $\overline{N} = 1$, $\tau \simeq 0.93$ and $T_c^* \simeq 1.85$ K ($\Delta^* \simeq 280$ µeV), and a value of critical current $I_S \simeq 25$ nA at $T = 75$ mK. The observed lower values of currents are consistent with the transport mechanism illustrated in Fig. 5.1b, where the supercurrent flows between the two proximized InSb regions with an induced gap Δ^*, rather than being dominated by the Nb gap Δ.

The exponentially enhanced conduction at low temperatures is typical of long channel states (of length d). The conduction via these states holds in the long junction limit $d \gg \xi_N$ and reads [11]:

$$I_L(T) = \frac{E_{Th}}{R_N e} a \left[1 - 1.3 \exp\left(-\frac{a E_{Th}}{3.2 k_B T}\right)\right], \tag{5.2}$$

where $E_{Th} = \hbar v_F l_e / 2d^2$ is the Thouless energy [110], R_N is the junction resistance and $a = 3$ [3]. The best fit of the long junction model is shown as the blue dashed line in Figure 5.1d and yields $E_{Th} \simeq 20$ µeV, corresponding to $d \simeq 3.5$ µm, close to the total length of the InSb nanoflag (3.35 µm), $R_N \simeq 400\,\Omega$ and a critical current $I_L \simeq 140$ nA at $T = 75$ mK.

Previous studies have documented similar results in highly transmissive ballistic SNS junctions with topological insulators or graphene [111, 150, 152–156], with the behavior being attributed to contributions from both surface and bulk states [153, 155]. One study linked the low-temperature enhancement to a low-energy Andreev bound state localized around the circumference of the junction [152]. In our nanoflags, this could be consistent with electronic transport at the edges of the nanoflag due to band-bending, similarly to what has been reported by de Vries et al. [125]. Compared to earlier works on InSb nanoflags that employed a Ti sticking layer between Nb and InSb [136, 137], the increase of I_{sw} at low temperature is consistent with the increased transparency achieved in this study through the direct deposition of bare Nb on the passivated surface of InSb, without the use of additional metallic layers.

Magnetotransport measurements further confirm the coexistence and magnitude of the two current conducting channels in the junction, providing additional insight into

[2] We are assuming for simplicity a BCS gap [151].
[3] The constant a is dependent on the ratio E_{Th}/Δ^* [11].

the current density distribution across the channels. The differential resistance of the junction $R = dV/dI$ as a function of magnetic flux is presented in Figure 5.1e. An unconventional Fraunhofer pattern, with a first lobe much more pronounced than the side lobes, is visible and well-described by the superposition of a conventional Fraunhofer pattern typical of short junctions, and a monotonic quasi-Gaussian decay, which is characteristic of long SNS junctions [59–61, 154, 157, 158]. The forward-biasing of the current results in a non-symmetrical supercurrent region for switching and retrapping currents (black area). The periodicity of the Fraunhofer pattern corresponds to one flux quantum inside the junction, taking into account a London penetration depth of $\lambda_L \simeq 100$ nm [159] and a flux enhancement of a factor of $\Gamma_f \sim 1.8$ due to flux focusing within the planar geometry. The critical current values from short and long transport channels estimated in Figure 5.1d are used here to model the magnetic interference patterns. The red line in Figure 5.1e shows the combined contribution of both channels to the supercurrent $I(\Phi_e) = I_S(\Phi_e) + I_L(\Phi_e)$, where $\Phi_e = \Gamma_f B(L + 2\lambda_L)W$ is the applied magnetic flux on the uncovered junction area, with $W = 650$ nm the junction width. The standard Fraunhofer pattern $I_S(\Phi_e) = I_S|\sin(\pi(\Phi_e/\Phi_0))/(\pi\Phi_e/\Phi_0)|$ expected for a wide-short junction, and a Gaussian decay $I_L(\Phi_e) = I_L \exp(-\sigma\Phi_e^2/\Phi_0^2)$, typical of a narrow-long junction, are accounted for in the calculation. We have included a possible different effective area of the long junction directly in the estimated value of $\sigma \sim 0.329$ while preserving the same flux dependence.

Our conclusions are further supported by the temperature-dependent change in the magnetoresistance, which exhibits an exponential reduction of the Gaussian component and limited variation in the Fraunhofer lobes up to $T = 800$ mK (refer to Figure 5.6 of the Additional material). This further excludes the hypothesis that non-uniformity in the current distribution within the short exposed junction area, though possible in our device, is the cause of the anomalous interference pattern, as it would imply a simultaneous decrease in both the central and side lobes with temperature. The lack of distinct oscillations in the magnetoresistance indicates that possible edge states are not interfering coherently with magnetic fields perpendicular to the nanoflag. However, the impact of flux screening, phase decoherence, and transport along various facets of the flag make it challenging to arrive at more definitive conclusions.

5.3. Half-integer Shapiro steps

Having established the response of the junction at equilibrium, we will now examine how the system behaves when subjected to a microwave irradiation. In Figure 5.2a, we present a sample $V(I)$ curve with a microwave tone at frequency $f = 1.75$ GHz and applied power $P_{RF} = 12$ dBm. As it can be difficult to estimate the precise power delivered to the sample, we will only refer to the power provided by the signal generator in the following discussion. Quantized voltage steps of amplitude $n \times hf/2e$ appear in the $V(I)$ characteristic (black line), as a result of the phase-locking between the microwave frequency and the junction Josephson frequency [26]. In addition to integer steps occurring at $n = \pm1, \pm2, \pm3, \ldots$, half-integer steps appear with $n = \pm1/2, \pm3/2, \pm5/2, \ldots$. The overlapping grey trace displays dV/dI and shows peaks associated to both integer and half-integer steps, some of which are highlighted by red arrows. Steps with fractions different from multiples of $1/2$ are not observed. A histogram, resulting from the

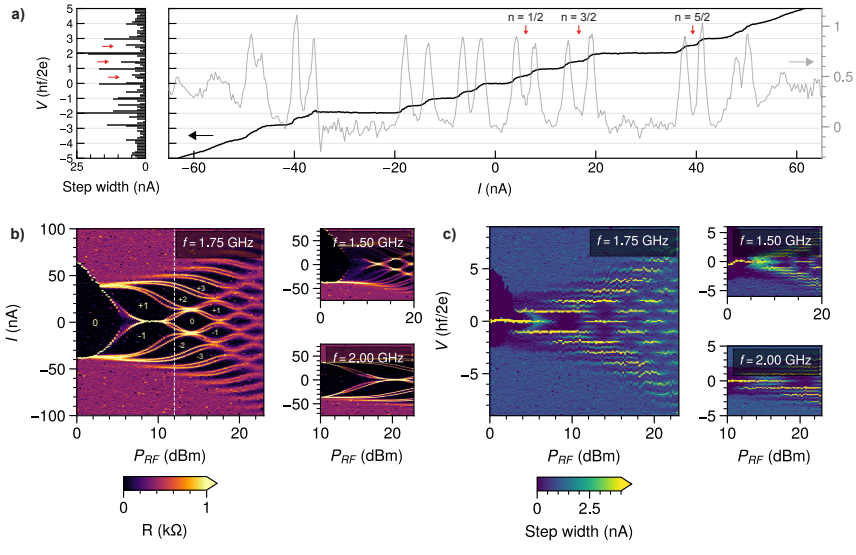

Figure 5.2: (a) Sample $V(I)$ curve (black) in the presence of microwave irradiation at $P_{RF} = 12\,\text{dBm}$ and frequency $f = 1.75\,\text{GHz}$. The grey line represents the differential resistance $R = dV/dI$ with arrows highlighting half-integer Shapiro steps. The histogram on the left shows the distribution of the voltage data. The bin unit is equal to the current step size, such that the number of counts corresponds to the width of the voltage plateaus. The value of P_{RF} refers to the one provided by the signal generator. (b) Full evolution of R as a function of current bias I and microwave power P_{RF} at $f = 1.75\,\text{GHz}$. Pairs of bright peaks indicate the presence of half-integer steps. The white dashed line corresponds to the data shown in (a). Label numbers refer to the corresponding step index n. The right side shows the colormaps for $f = 1.50\,\text{GHz}$ and $f = 2.00\,\text{GHz}$. (c) Histograms, as shown in (a), are displayed based on the data in (b) in a colorplot as a function of microwave power P_{RF}.

binning of the voltage data, is shown on the left and provides an immediate visual representation of the length of each step. The bin unit equals the current step size, such that the number of counts corresponds to the width of the voltage plateaus.

Figure 5.2b shows a color plot of R as a function of I and P_{RF}. Sharp jumps in voltage appear as bright peaks in R, while voltage plateaus correspond to dark regions. The pattern of bright peak pairs in the data provides stark evidence of fractional steps that occur over a wide range of power and frequencies, as demonstrated by the maps at $f = 1.50\,\text{GHz}$ and $f = 2.00\,\text{GHz}$. The region between the plateaus ± 1 displays bistability at around $P_{RF} = 10\,\text{dBm}$ of applied power, with sudden switching occurring between the two overlapping plateaus (see the Additional material for further discussion). Figure 5.2c better highlights the emergence of Shapiro steps by depicting the evolution of the histogram data as a function of microwave power for various frequencies. In the Additional material, we present additional measurements for different backgate voltages, magnetic field values, and temperatures. These measurements confirm the robustness of the observed half-integer steps, indicating that the effect is not related to variations in current density or flux motion.

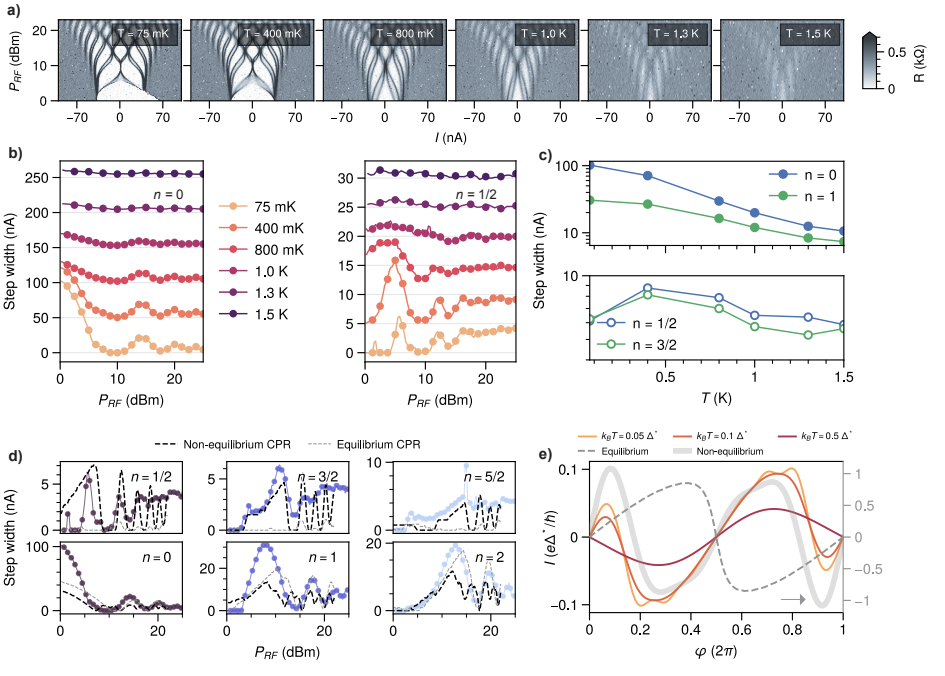

Figure 5.3: (a) Shapiro maps at different temperatures $T =$ (75 mK, 400 mK, 800 mK, 1.0 K, 1.3 K, 1.5 K) at $f = 1.75$ GHz. (b) Step width for $n = 0$ (left) and $n = 1/2$ (right) extracted from the temperature maps show in (a). As temperature increases, a monotonic decrease is observed for $n = 0$, while a non-monotonic evolution with a maximum at 400 mK is observed for $n = 1/2$. Traces are offset for clarity, with an offset of 50 nA (left) and 5 nA (right). (c) Step widths displayed on a semi-log scale as a function of T for integers $n = 0, 1$ (top) and half-integers $n = 1/2, 3/2$ (bottom). Microwave powers $P_{RF} = 0$ dBm for $n = 0$, $P_{RF} = 8$ dBm for $n = 1$, $P_{RF} = 5.5$ dBm for $n = 1/2$, and $P_{RF} = 11$ dBm for $n = 3/2$. (d) Step width of half-integer $n = 1/2, 3/2, 5/2$ (top) and integer $n = 0, 1, 2$ (bottom). Each trace is a horizontal slice of Figure 5.2c. The dashed black lines represent the numerical simulations obtained from the extended RCSJ model using the non-equilibrium CPR shown as the thick grey line in (e). The dashed grey lines represent the simulations using the equilibrium CPR. (e) CPRs under microwave irradiation for $\tau = 0.98$ and driving $w = 1.3$ at different temperatures ($k_BT = 0.05$, 0.1, and 0.5 Δ^*) are depicted by light to dark orange lines. The dashed grey line represents the equilibrium CPR at $w = 0$ and $k_BT = 0.05\ \Delta^*$, for the same value of τ. The thick grey line represents the effective non-equilibrium CPR used in panel (d).

We then study the behavior of the system by increasing the temperature. Figure 5.3a displays Shapiro maps at temperatures ranging from $T = 75\,\mathrm{mK}$ ($\sim 0.02\,\Delta^*/k_B$) to $T = 1.5\,\mathrm{K}$ ($\sim 0.5\,\Delta^*/k_B$). The temperature rise leads to a decrease of the supercurrent and an increase in thermal fluctuations, resulting in rounded voltage plateaus. However, the half-integer steps remain stable from base temperature up to around $1\,\mathrm{K}$ ($\sim 0.3\,\Delta^*/k_B$), where the current-phase relationship (CPR) given by the equilibrium supercurrent is expected to be mostly sinusoidal (as illustrated in Figure 5.13).

Figure 5.3b shows the change in step width for the steps $n = 0$ and $n = 1/2$ extracted from Figure 5.3a. The amplitude of the integer step decreases monotonically with increasing temperature, while the half-integer step shows a non-monotonic trend, with a maximum at $T \simeq 400\,\mathrm{mK} \sim 0.12\,\Delta^*/k_B$. This is also demonstrated in Figure 5.3c, where the step widths for $n = 0, 1$ and $n = 1/2, 3/2$ are plotted on a semi-log scale as a function of T. While the integer steps show an exponential decrease, the width of the half-integer steps first increases, then decreases, and eventually saturates due to the noise level at high temperatures. This remarkable evolution points to a non-equilibrium origin of the half-integer steps, where the supercurrent is altered by a non-equilibrium population of the ABSs that is induced by the microwave drive. This is consistent with theoretical predictions and experimental observations that non-equilibrium supercurrents are less sensitive to temperature compared to equilibrium supercurrents, which are exponentially suppressed [33, 112, 160–163].

In the Additional material, we provide data from an additional device with lower transparency. While the junction behaves similarly under microwave irradiation, the signatures of the half-integer steps are considerably weaker.

5.4. Discussion

Despite their frequent occurrence, the origin of fractional steps in superconducting devices is not univocal. Measurements of fractional Shapiro step are commonly used to identify non-sinusoidal CPRs in highly transparent SNS junctions [164], or in junctions incorporating ferromagnetic layers [114, 115, 165, 166] or those exhibiting exotic superconducting states [167, 168]. Geometric or intrinsic capacitance [61, 146–148, 169], and circuit feedback [28, 170, 171] can also contribute to the appearance of fractional steps or hysteretic behavior. Sub-harmonic structures may also indicate a unique mode of a more complex circuit network, as seen in junction arrays [172–177] and superconducting quantum interference devices (SQUIDs) [174, 178, 179]. These manifestations are also visible even in the absence of multiple superconducting terminals, as in grain boundary or step-edge junctions [180–183], as a consequence of the complex evolution of multiple phase-locked states.

The fractional steps reported in the previous examples, including both ballistic and diffusive SNS junctions, are ascribed to the equilibrium properties of the supercurrent and can be understood within a phenomenological extended resistively and capacitively shunted junction (RCSJ) model, which takes into account the dissipative environment surrounding the junction, as depicted in Fig. 5.1c [28, 31, 145]. In the phase-particle picture, neglecting capacitive effects, the phase evolves in a washboard potential that is tilted by the applied bias current and modulated by the time-dependent drive. Shapiro steps arise as time-dependent phase slips between the minima of the Josephson potential,

and for a typical $\sin(\varphi)$ CPR, integer steps arise as $2\pi n$ phase slips. Within this picture, half-integer Shapiro steps require an energy-phase relation that displays a secondary minimum and arise when the second harmonic of the CPR is stronger than the first one.

However, a microwave drive can also significantly alter the supercurrent's steady-state behavior, exciting non-equilibrium supercurrents [23, 24, 33, 35, 112, 142, 160–163, 184–188]. The adiabatic changes in the ABS energies, as well as the multiple transitions induced by microwave photons between the ABSs or between the ABSs and the continuum, can result in a non-trivial dynamics of the supercurrent-carrying states [23, 24, 35, 160]. Such effects can give rise to highly distorted CPRs, which exhibit sign-reversals of the supercurrent and π-periodic oscillations at twice the Josephson frequency [34, 112, 161, 162, 184, 186, 187].

We notice that in the experiment the induced gap $\Delta^* \simeq 280\,\mu\text{eV}$ (67 GHz), so that we cover values $hf \simeq 0.03\ \Delta^*$. In an effort to capture the emergence of half-integer Shapiro steps, we describe the junction dynamics by adiabatically incorporating non-equilibrium effects into the RCSJ model of Fig. 5.1c through a single effective CPR. The latter is provided by the thick grey line in Fig. 5.3e, and its origin will be discussed later. In Figure 5.3d, we plot the step width for integer and half-integer values of n vs. P_{RF}, obtained as horizontal slices of Figure 5.2c at constant V. The dashed black line in the figure shows the results of the simulation using the effective non-equilibrium CPR, while the dashed grey line represents the equilibrium one. Although the equilibrium CPR effectively reproduces the integer steps in the oscillatory pattern (bottom row), it completely fails to capture the half-integer steps (top row). This is despite the presence of higher-order harmonics in the highly skewed CPR, which are often attributed to the origin of half-integer steps [164].

To gain further insight into the origin of such a distorted CPR, we used a tight-binding method within the Keldysh-Green's function approach [24, 35] to numerically calculate the current-phase relationship of an SNS junction irradiated by a microwave tone. The model describes a single-channel Josephson junction with an arbitrary junction transparency τ and gap Δ^*. The microwave driving is included as a time-dependent modulation of the phase difference across the junction with amplitude $w = eV_{RF}/hf$. Figure 5.3e shows the simulated CPR for microwave irradiation of $hf = 0.1\ \Delta^*$ at a microwave driving of $w \sim 1.3$ and $\tau = 0.98$ for different temperatures. The dashed grey line represents the equilibrium CPR. The microwave irradiation significantly alters the CPR, boosting a strong second harmonic, which results in the development of an additional minimum. This provides insight into the origin of the effective non-equilibrium CPR used in the RCSJ model. The wiggles in the CPR are due to non-equilibrium population of Floquet sidebands produced by the microwave driving and disappear at temperatures on the order of the driving frequency, $k_BT \sim hf$. In turn, the secondary minimum is robust and still visible at $k_BT = 0.1\ \Delta^*$, as shown in Figure 5.3e, and it qualitatively agrees with the robustness of the half-integer steps with respect to temperature. In the Additional material, we detail the theoretical model and present additional simulations showing that reducing the junction transparency results in the disappearance of the CPR's secondary minimum (Figure 5.13).

The outlined procedure should be regarded as an attempt to reconcile the results of the adiabatic approximation, typical of the RCSJ model, with the microscopically calculated CPR in the presence of microwave driving and in the absence of a steady voltage

across the junction. In particular, the model reproduces the two-minima shape of the effective non-equilibrium CPR only within a limited range of w values, which is inconsistent with the experimental observations and highlights the limitations of the present description. Alternative phenomenological theories of non-equilibrium supercurrents have been proposed [112, 161, 184], which model the system by considering both the ABSs and their occupation distributions oscillating at the Josephson frequency. The specific structure of the ABSs, including the effects of finite junction length or ballistic quasi two-dimensional transport, may be responsible for the discrepancies between different predictions, which calls for more comprehensive theories.

5.5. CONCLUSIONS

In conclusion, we have investigated a highly transmissive Josephson junction made of an InSb nanoflag with Nb contacts. Our results indicate strong evidence of parallel transport in both long and short conducting channels, confirmed by the temperature-dependent supercurrent and magnetic field interference. Under microwave irradiation, we observe strong half-integer Shapiro steps, showing a non-monotonic temperature evolution that points to non-equilibrium effects induced by the driving. The observed phenomenology is only partially captured by the predictions based on the adiabatic approximation in terms of a non-equilibrium CPR. Further theoretical developments are needed to address the presence of strong second harmonic supercurrents in ballistic, highly transparent SNS junctions. Future experiments should investigate the potential of InSb nanoflag Josephson junctions for exploring the coherent manipulation of Andreev states and their non-equilibrium dynamics.

5.6. ADDITIONAL MATERIAL

5.6.1. SAMPLE INFORMATION AND MEASUREMENT TECHNIQUES

The InSb nanoflags utilized in this work have been extensively described in previous studies [129, 134]. They are defect-free structures that exhibit excellent electrical properties, including high mobility (up to 29 500 cm V^{-2} s^{-1}) and a large mean free path ($l_e \simeq$ 500 nm) at $T = 4.2$ K. The devices were fabricated by placing nanoflags on a p-doped Si/SiO_2 substrate, which served as a backgate, and connecting them with 150 nm of Nb deposited via DC magnetron sputtering at a deposition rate of approximately 1 nm s^{-1} in a chamber with a base pressure of 2×10^{-6} mbar. Prior to metal deposition, a passivation step was performed to improve the semiconductor-metal transparency. The critical temperature of Nb was measured to be 8.9 K on two independently connected electrodes on the same device, corresponding to a gap $\Delta = 1.76 k_B T_c \sim 1.35$ meV. Further information on device fabrication can be found in the supporting material of Salimian et al. [136] and Turini et al. [137]. We conducted transport measurements using a low-temperature Leiden Cryogenics dilution refrigerator with a base temperature of 75 mK. The cryostat is equipped with a three-level filtering system, comprising π filters at room temperature as well as cryogenic π and RC filters at base temperature. The $V(I)$ curves were acquired in a standard four-wire configuration, with the junction current-biased using a Yokogawa GS200 voltage source over a 10 MΩ resistor. The voltage drop over the junction was amplified by a factor 1000 using a room temperature DL1201 voltage

preamplifier operated in battery mode and acquired by an Agilent 34410 multimeter. We applied voltage to the backgate using a Keithley 2602 voltage source. Microwave signals were applied using an R&S SMR20 microwave source to an attenuated semi-rigid open-ended coaxial cable in close proximity to the sample holder, which had been attenuated by 20 dB and 10 dB at 3K and Cold plates, respectively. For measurements in magnetic field, we used a low-noise Keithley 2400 sourcemeter connected to a 2 T American Magnetics superconducting magnet.

5.6.2. Dependence on Backgate Voltage

Figure 5.4(a-d) displays $V(I)$ curves in a higher current range at different backgate voltages V_G ranging from 10 V to 40 V. For negative gate voltages, the InSb nanoflag is insulating, and no supercurrent can flow. The black dashed line fitted to the Ohmic region allows obtaining the normal state resistance R_N and excess current I_{exc}. In panel (e), we present the switching current I_{sw} and retrapping current I_{rt} over the same range of gate voltages. The switching current I_{sw} decreases from 170 nA to 75 nA as the gate voltage is varied, while the retrapping current I_{rt} remains roughly constant at approximately 30 nA.

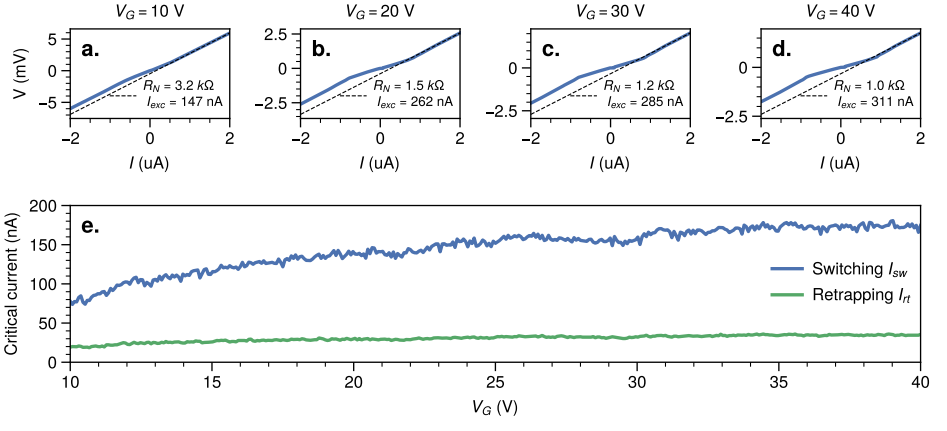

Figure 5.4: (a-d) Sample I-V traces for different V_G values (10,20,30,40) V. The black dashed line is the linear fit to the Ohmic region used to extract R_N and I_{exc}. (e) Full backgate dependence of the switching and retrapping current in the same gate voltage range.

Figure 5.5a depicts the evolution of R_N and $G_N = 1/R_N$ as a function of V_G, with the resistance decreasing from 3 kΩ (at $V_G = 10$ V) to 1 kΩ (at $V_G = 40$ V). The high transparency of the junction is confirmed by the high values of the excess current I_{exc} and the $I_{sw}R_N$ product. Figure 5.5b shows the excess current as a function of V_G in the same range. The product $I_{exc}R_N$ remains roughly constant at about 350 μV (1.2 Δ^*/e) over the entire gate voltage range, close to the theoretical value of $8/3\ \Delta^*/e$ predicted for the ballistic case (Fig. 5.5c) [189]. Moreover, the product $I_{sw}R_N$ is expected to be $I_{sw}R_N = 10.82\ E_{Th}/e$ for a long diffusive junction in the limit $\Delta^* \gg E_{Th}$ [11]. In our device, $I_{sw}R_N$ varies from 180 μV to 250 μV ($7 - 10\ E_{Th}/e$) (Fig. 5.5d). Additionally, we can estimate the transparency of the superconductor-semiconductor interface to be

$\gamma_B \sim 7$ [190], which is almost half the value reported in [136], confirming the increased transparency.

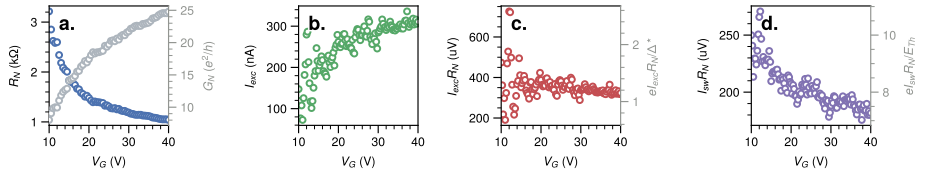

Figure 5.5: (a) Normal state resistance R_N, (b) excess current I_{exc}, (c) $I_{exc}R_N$ product, and (d) $I_{sw}R_N$ product plotted as functions of the backgate voltage V_G.

5.6.3. MAGNETIC INTERFERENCE MAPS

Figures 5.6 and 5.7 present additional measurements of magnetic interference patterns at different temperatures, $T = (300, 500, 800)$ mK, and backgate voltages, $V_G = (30, 20, 10)$ V. The magnetoresistance maps in Figure 5.6 demonstrate a decrease in the Gaussian-like contribution as the temperature increases, further confirming that the exponential suppression of I_{sw} is related to states in the long junction limit. The Fraunhofer diffraction side-lobes remain unchanged up to a temperature of 500 mK, consistent with the limited dependence of $I_{sw}(T)$ for modes in the short junction limit, and eventually begin to disappear only for $T > 800$ mK.

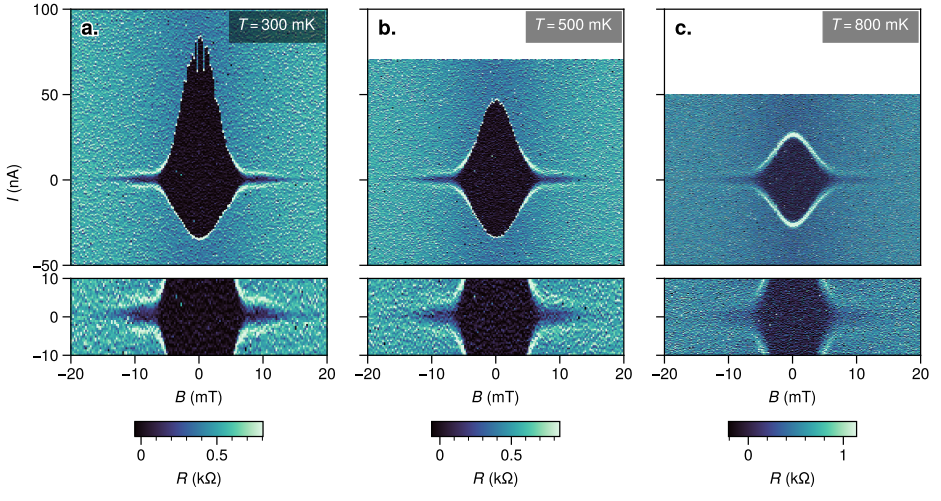

Figure 5.6: Magnetoresistance maps at temperatures of (a) 300 mK, (b) 500 mK, and (c) 800 mK. Below each panel, a zoom-in on the low bias region shows the behavior of the side-lobes with respect to T.

Figure 5.7 shows the magnetoresistance evolution in V_G. States in the long junction limit are more sensitive to changes in the semiconductor depletion level at low gate

voltages V_G, as evidenced by the corresponding changes in the Gaussian amplitude. Only a little variation of the Fraunhofer diffraction lobes is observed confirming the high homogeneity of the current density in the short junction area between the electrodes.

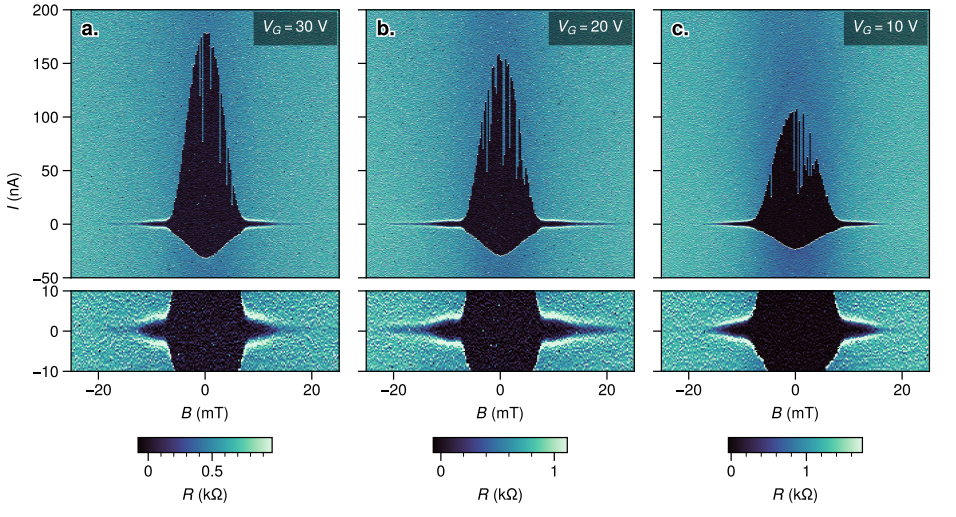

Figure 5.7: Magnetoresistance maps at backgate voltage V_G of (a) 30 V, (b) 20 V, and (c) 10 V. Below each panel, a zoom-in on the low bias region shows the behavior of the side-lobes with respect to V_G.

5.6.4. Shapiro Maps at finite Magnetic Field

Figure 5.8 depicts the Shapiro maps obtained at a frequency of $f = 1.75$ GHz for different out-of-plane magnetic field values ranging from 0 to 11 mT. As the magnetic field suppresses I_c, the reduced drive frequency $\Omega = \frac{2\pi f}{2eI_cR_j/\hbar}$ increases, and the $V(I)$ maps follow the Bessel function dependence on the applied RF power [28, 145].

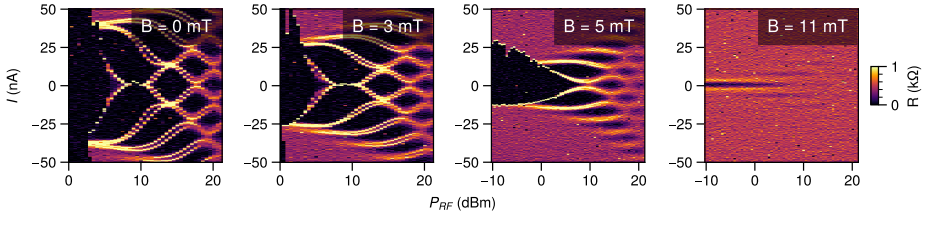

Figure 5.8: Shapiro maps at $f = 1.75$ GHz for various out-of-plane magnetic field strengths B ranging from 0 to 11 mT.

5.6.5. Shapiro Maps at different Backgate Voltages and Temperatures

The evolution of the half-integer steps is robust in temperature and backgate voltage, as detailed by the scans in Fig. 5.9 for $V_G = 40$ V (top row) and $V_G = 10$ V (bottom row).

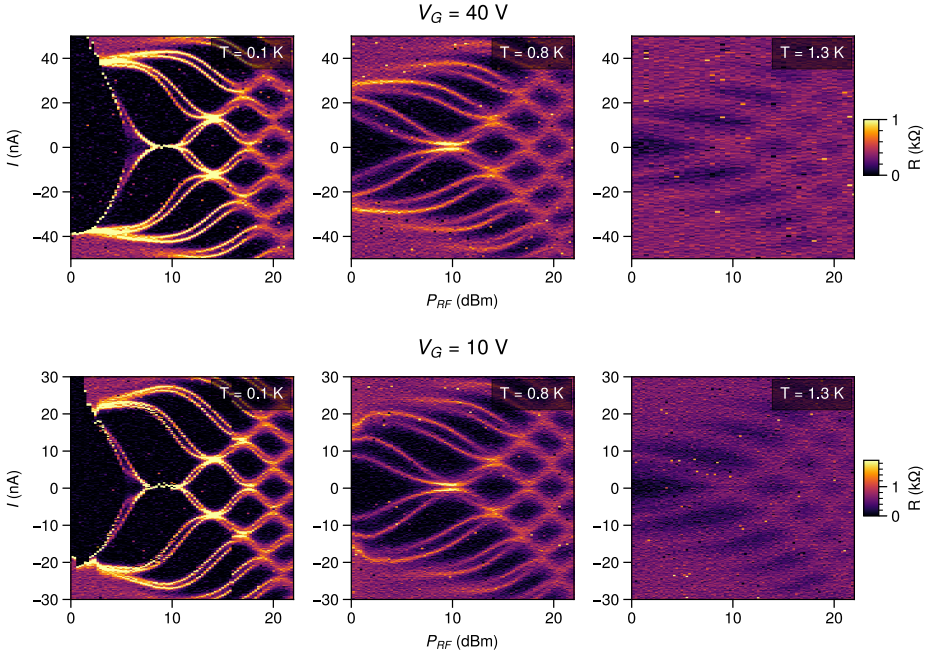

Figure 5.9: Top row: Shapiro maps at $f = 1.75\,\text{GHz}$ for different temperatures of 0.1 K, 0.8 K, and 1.3 K at a backgate voltage of 40 V. Bottom row: same maps for a backgate voltage of 10 V.

5.6.6. SHAPIRO MAPS AT ZERO CROSSING STEP

We present in Fig. 5.10 a more detailed scan of the Shapiro map at $f = 1.75\,\text{GHz}$, covering a restricted range of microwave power and currents as shown in Figure 5.2. Zero-crossing steps (red line) are visible as a result of the overlapping ± 1 lobes. The presence of zero-crossing steps has been extensively investigated in Larson et al. [145] and explained as a consequence of the shunting RC environment and the high $I_c R_j$ product.

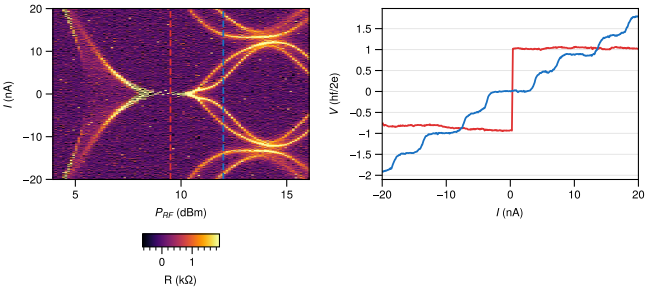

Figure 5.10: Left: A zoom-in view of the Shapiro maps at $f = 1.75\,\text{GHz}$, as shown in Figure 5.2, highlighting the zero-crossing steps and providing finer details of the half-integer plateaus. Right: The red and blue $V(I)$ cut shown on the left for $P_{RF} = 9$ dBm and $P_{RF} = 12$ dBm, respectively.

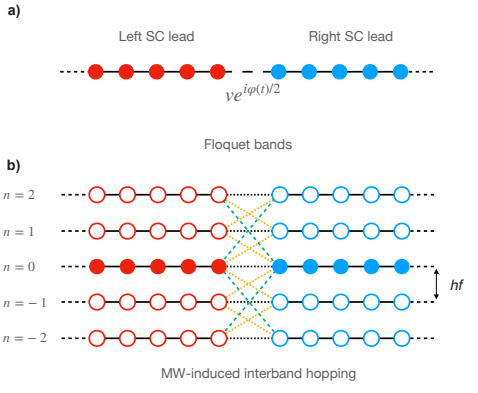

Figure 5.12: (a) 1D tight-binding model describing the Josephson junction. The driving appears as a time-dependent phase in the left-right hopping amplitude. (b) Floquet side bands shifted in energy by nhf. The different bands are coupled at the interface by the time-oscillating phase.

5.6.7. Data from an additional Device with lower Transparency

An additional device has been measured in a similar way, which had a 5 nm Ti adhesion layer embedded under the niobium layer. In this case, only weak signatures of half-integer steps are visible.

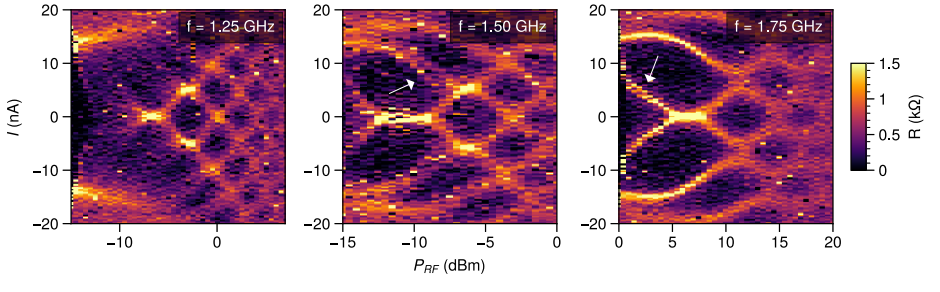

Figure 5.11: Shapiro maps for $f = 1.25, 1.50$ and $1.75\,\mathrm{GHz}$ for a device with reduced transparency.

5.6.8. Theory

CPR under microwave irradiation

Our microscopic model for a microwave-irradiated Josephson junction is based on the works of Bergeret et al. [24], Cuevas et al. [35], Cuevas and Yeyati [191] and consists of a highly transparent junction, with a short ballistic region between the left and right superconducting leads (L and R, respectively), as schematically displayed in Figure 5.12a. We describe the system through the 1D tight-binding Hamiltonian $H = H_L + H_R + \sum_\sigma (v c^\dagger_{L\sigma} c_{R\sigma} + v^* c^\dagger_{R\sigma} c_{L\sigma})$, where the left and right leads are described by $H_\alpha = -\mu \sum_{n\sigma} c^\dagger_{\alpha,n,\sigma} c_{\alpha,n,\sigma} - t \sum_{n,\sigma} (c^\dagger_{\alpha,\sigma,n} c_{\alpha,\sigma,n+1} + \mathrm{H.c.}) + \Delta_\alpha \sum_n c^\dagger_{\alpha,n,\uparrow} c^\dagger_{\alpha,n,\downarrow} + \mathrm{H.c.}$,

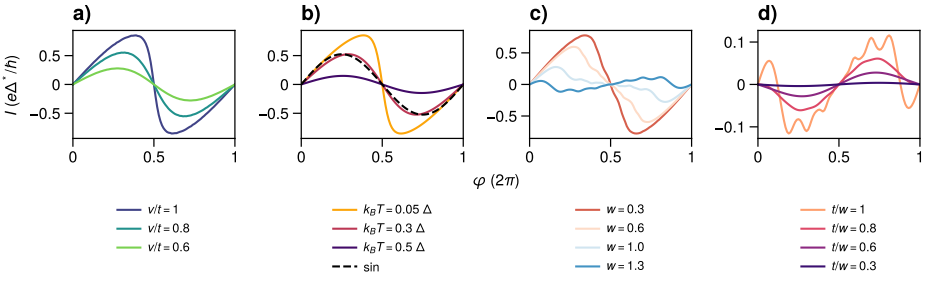

Figure 5.13: Different CPRs: (a) in the absence of microwave irradiation for different transparencies, (b) in the absence of microwave irradiation for different temperatures, (c) for different microwave drive strengths at $v/t = 1$, and (d) for different transparencies at driving $w = 1.3$.

with c and $c^\dagger$ being the annihilation/creation operators for particles with spin σ in the superconducting leads and $\Delta_\alpha = \Delta e^{i\varphi_\alpha}$, with $\varphi_R - \varphi_L = \varphi$ their phase difference. The normal state transmission of this single channel model is $\tau = \frac{4(v/W)^2}{(1+(v/W)^2)^2}$, where $W = 1/(\pi\rho_F) = \sqrt{4t^2 - \mu^2}/2$ and ρ_F is the density of states at the Fermi energy in the leads. The current takes the form $\hat{I}(t) = \frac{ie}{\hbar}\sum_\sigma (v c^\dagger_{L\sigma} c_{R\sigma} - v^* c^\dagger_{R\sigma} c_{L\sigma})$, and under microwave irradiation, the phase difference acquires the time dependence $\varphi(t) = \varphi_0 + 2w\sin(2\pi f t)$ with $w = eV_{\rm ac}/hf$, so that $v \to v e^{i\varphi(t)/2}$.

The microwave source can inject and absorb photons of frequency f, so that an incident carrier with energy ϵ can be scattered into states with energy $\epsilon + nhf$. Introducing the Floquet sidebands, which are replicas of the system shifted in energy by nhf, the hopping term $\hat{v}_{LR}$ can couple different sidebands $\hat{v}_{n,m} = \int dt e^{i(n-m)2\pi f t}\hat{v}(t) = v\begin{pmatrix} J_{n-m}(w)e^{i\varphi_0/2} & 0 \\ 0 & -J_{m-n}(w)e^{-i\varphi_0/2}\end{pmatrix}$, where $J_n(w)$ are Bessel functions of the first kind, and we have absorbed the possible phase of v in the phase difference φ_0. The hopping between the L and R leads acquires a matrix structure that connects the rightmost site in the L lead and Floquet band n with the leftmost site of the R lead and Floquet band m, as schematized in Fig. 5.12b.

We now apply the microscopic theory and calculate different CPRs under microwave irradiation. In the absence of driving ($w = 0$), the model accurately reproduced the CPRs of the junction in both the highly transparent and tunneling regimes by varying the ratio v/t, as shown in Fig. 5.13a, and for different temperatures, as shown in Fig. 5.13b. We then apply increasing microwave driving and observe a second zero of the CPR in the interval 0-π, along with a region of negative current for positive phase bias, which indicated the occurrence of a secondary minimum (Fig. 5.13c). At high driving amplitude, the CPR exhibits wiggles due to the presence of Floquet sidebands, which decay with temperature, as shown in Fig. 5.3e. Finally, Figure 5.13d shows that the CPR loses its secondary zero for low transmission. These features are qualitatively similar to those observed in the additional device reported in the experiment. Including additional bands up to 6 does not qualitatively change the discussion above.

RCSJ model

In the previous section, we described the microscopic theory of non-equilibrium supercurrents in a microwave irradiated Josephson junction in the presence of an AC voltage bias. However, modeling the time-dependent phase dynamics in the presence of non-equilibrium effects, particularly for the experimentally relevant current-bias scenario, is more challenging. Moreover, we find that the environment surrounding the junction plays an important role, as confirmed by the deviations from the Bessel regime and the presence of zero-crossing steps. We opted for a simplistic approach that employs a modified version of the resistively and capacitively shunted junction (RCSJ) model, which includes the dissipative environment surrounding the junction [31, 145] and incorporates the non-equilibrium effects only in a single effective CPR. Despite the simplicity of the assumptions, we are able to capture the main findings of this work. The junction, which has a critical current I_c, is shunted by a capacitance C_j and resistance R_j, and is additionally shunted by an RC environment represented by a parallel capacitor C and resistor R. The entire circuit is biased by a current I, which accounts for the external DC and AC bias. The equations for the current I and the voltage V, shown in Figure 5.1c, are:

$$\begin{aligned} I &= I_{DC} + I_{RF}\sin(2\pi f t) \\ &= C\frac{dV}{dt} + \mathrm{CPR}(\varphi) + \frac{\hbar}{2eR_j}\frac{d\varphi}{dt} + \frac{\hbar C_j}{2e}\frac{d^2\varphi}{dt^2} \\ V &= \frac{\hbar}{2e}\frac{d\varphi}{dt} + R\left(\mathrm{CPR}(\varphi) + \frac{\hbar}{2eR_j}\frac{d\varphi}{dt} + \frac{\hbar C_j}{2e}\frac{d^2\varphi}{dt^2}\right), \end{aligned} \tag{5.3}$$

where φ is the macroscopic phase difference across the junction, I_{DC} and I_{RF} are the DC and RF current biases, respectively, and $\mathrm{CPR}(\varphi)$ is the junction's current-phase relationship. We use a fourth-order Runge-Kutta method to solve for $\varphi(t)$ and obtain the DC voltage across the junction as $V_j = \left\langle \frac{\hbar}{2e}\frac{d\varphi}{dt} \right\rangle$.

In the limit of small I_c, the Shapiro map follows the Bessel function dependence, with steps centered at $I_n = \frac{V_n}{R_j}$ and an extension of $\sim I_c|J_n(2w)|$, where $V_n = n\frac{hf}{2e}$ and $w = eV_{AC}/hf$. Figure 5.14a shows the Shapiro map at lower I_c with an applied external magnetic field of $B = 5\,\mathrm{mT}$. From the position of the centers, we can extract $R_j \sim 420\,\Omega$ (dotted white lines), while the dashed lines show a good agreement with the Bessel behavior, depicting the amplitudes $I_c|J_n(2w)|$, with $V_{AC} = \alpha \times 10^{P_{RF}/20}$, $\alpha \sim 0.8$ and $I_c \sim 10\,\mathrm{nA}$.

Figures 5.14b and 5.14c show the complete maps for the simulation presented in Fig. 5.3d for the equilibrium and non-equilibrium CPRs, respectively, obtained by the model in Eq. 5.3. While the equilibrium CPR well describes the overall trend, it completely lacks half-integer steps, which are instead captured by the effective non-equilibrium CPR. This is despite the presence of higher-order harmonics in the skewed equilibrium CPR. In the simulation, we estimate the geometric capacitance of the junction to be $\sim$ fF and neglect C_j. The capacitance C is determined by the bonding pads' capacitance to the SiO_2 backgate, which we estimate to be $C \sim 15\,\mathrm{pF}$, while the value of R is set to $R \sim 150\,\Omega$ to achieve the best agreement with the experiment. The CPR is expressed as $\mathrm{CPR}(\varphi) = \sum_n I_{c,n}\sin(n\varphi)$, where $I_c = \max_\varphi \mathrm{CPR}(\varphi)$, which is set to 35 nA. The current I_{RF} is given by $I_{RF} = \beta \times 10^{P_{RF}/20}$ with $\beta \sim 20$.

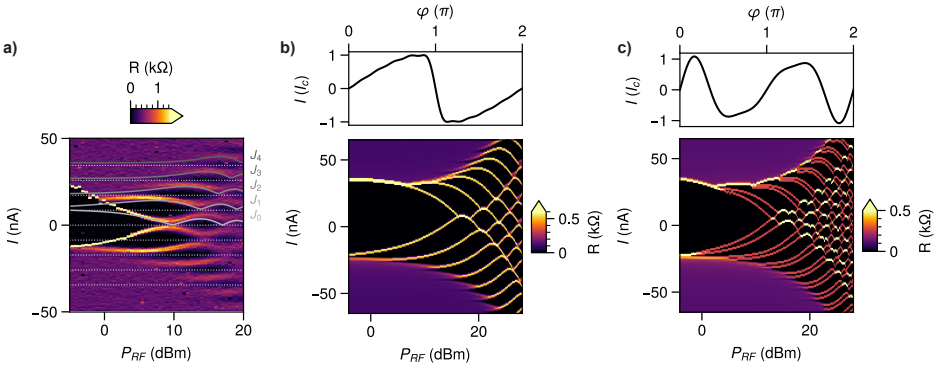

Figure 5.14: (a) Experimentally measured Shapiro map in the Bessel regime at $B = 5\,\mathrm{mT}$. The dotted white lines are used to extract R_j, while the continuous lines show the dependence on the Bessel function J_n. (b) Numerical simulation of the Shapiro map with the equilibrium skewed CPR. The amplitudes of the harmonics are $I_{c,n}$ = (0.91, -0.33, 0.19, -0.12, 0.09, -0.06, 0.04, -0.03, 0.03, -0.02). (c) Same as in (b) for the effective non-equilibrium CPR with the amplitudes $I_{c,n}$ = (-0.38, 0.75, 0.44, 0.22).

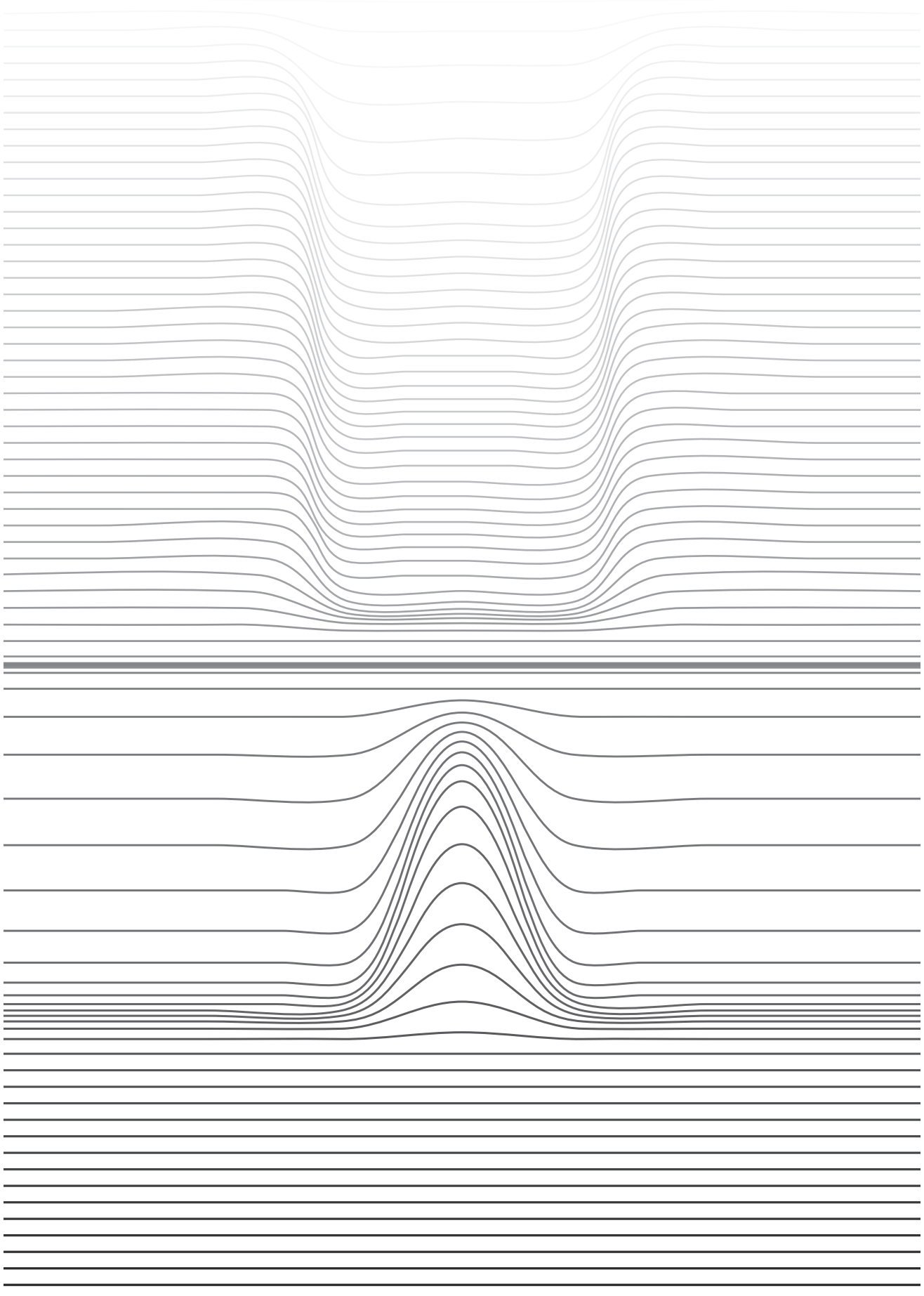

6

Gate-tunable superconductivity

In the last few years, a series of exciting experiments have shown that superconductivity in a metallic weak-link can be controlled by applying voltages to electrostatic gates, in a similar experimental way as semiconducting transistors are controlled by the field effect. This discovery has the potential to revolutionize the world of supercomputing, leading to a technology that would combine the advantages offered by semiconductors and superconductors. However, the underlying physical mechanism behind this effect is still unclear, and it has been demonstrated only at low frequencies. In this chapter, we will provide a historical overview and the current state of understanding of the gating effect in metallic superconductors. We will discuss the experimental results of the gating effect on weak-links embedded in microwave resonators fabricated during this thesis. Finally, we will conclude with a comprehensive review of the experimental data, comparing relevant parameters and providing insights into the potential for future applications.

6.1. Introduction

The effect was first reported in 2018, when De Simoni et al. [192] demonstrated the suppression of supercurrents in superconducting titanium and aluminum Dayem-bridges when subjected to a gate voltage applied on a nearby gate line. This finding was unexpected as the gate voltage was not thought to affect a metallic wire since electrostatic fields are rapidly screened in superconductors, similar to normal metals. The results were initially interpreted as an electrostatic-field suppression of the supercurrent. Since then, numerous experimental publications have extended the materials used, investigated the effect on the superconducting phase in SQUIDs, and examined the distribution of the switching currents under gating [193–197]. Additionally, microscopic theoretical analyses of the electrostatic field effect were developed, based on electric field-induced surface orbital polarization, Rashba-like surface effects, and pair-breaking phenomena due to Schwinger-like effects [198–201].

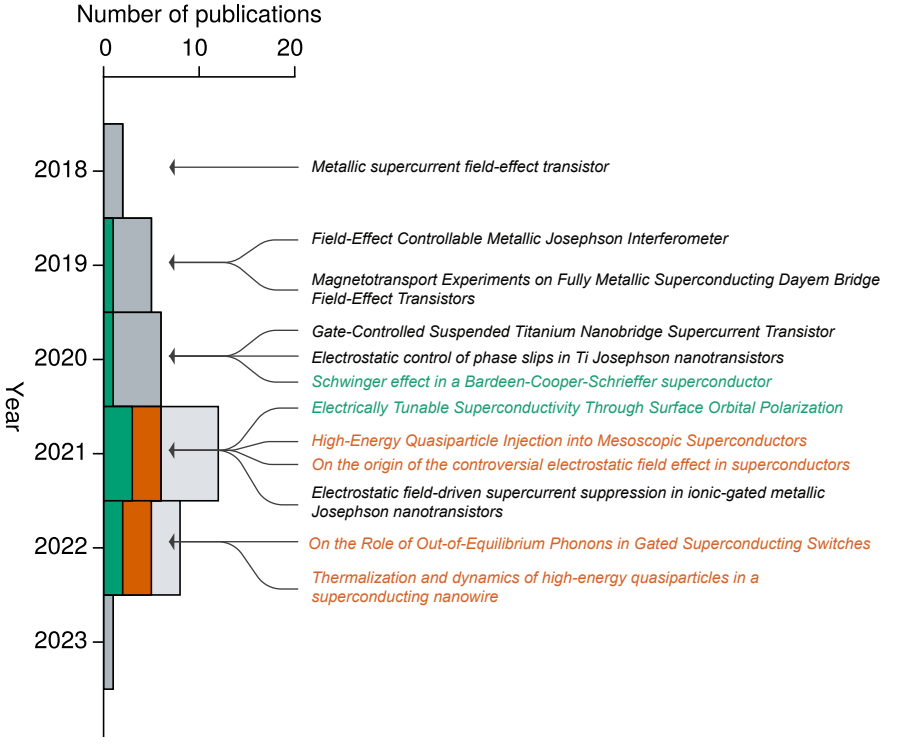

Figure 6.1: Historical development of the gating effect. In dark grey the publications related to the electrostatic-field hypothesis, in green theoretical proposals, in orange publications opposing the electric-field hypothesis.

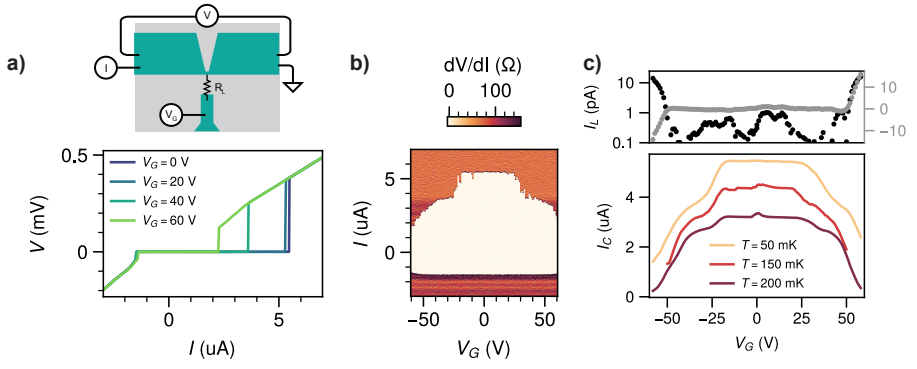

Figure 6.2: Typical characterization of the gating effect. a) $V(I)$ curves for a Ti Dayem-bridge shown as a function of the applied gate voltage V_G. The current is swept from negative to positive values. Top: typical simplified device schematic. b) Differential resistance dV/dI as a function of current and gate voltage. A bipolar modulation of the switching current is observed with respect to V_G. The retrapping current is only affected at high V_G. c) The temperature evolution of the switching current is shown for different temperatures T. As the temperature increases, the effectiveness of the gate is reduced. Top: an increase in leakage current I_L is measured, occurring at the same time or at a slightly higher value of V_G than at supercurrent suppression. The black trace is shown on a log scale, while the grey trace on a linear one. The leakage current is measured as described in Section 3.2.3.

In the years that followed, several publications have questioned the interpretation of the electrostatic-field effect [202–206]. It has been argued that a small leakage current originating from the gate electrode is primarily responsible for the suppression of the supercurrent. This leakage current can suppress the supercurrent by either causing highly energetic electrons to flow through the substrate (or vacuum) and impinge upon the superconducting wire, or indirectly by propagating out-of-equilibrium phonons resulting from charge injection into the substrate. We will discuss each of these scenarios in more detail. Figure 6.1 illustrates the (brief) historical development of the gate-tunable supercurrent suppression in metallic nanowires, highlighting experimental publications supporting the electrostatic field-effect hypothesis in dark grey, publications opposing this interpretation in orange, and theoretical ideas proposed behind the phenomenon in green.

6.2. EXPERIMENTAL PHENOMENOLOGY

The effect is typically measured in a four-wire configuration, as shown in Fig. 6.2, where a thin superconducting film (typically of the order of the coherence length ξ_0) is deposited to create a device that features a narrow wire or constriction. The device is then current-biased, and the voltage drop V across the device is measured while sweeping the current at various gate voltage values V_G. It has been observed that the gate voltage V_G reduces the switching current I_{sw} at which the device switches to the normal from the superconducting state, as shown in Fig. 6.2a and b. Typically, a device employs side gates, although back gates have also been used. The gate-superconductor separation

is very small, usually between $d = 50 - 150$ nm, while the effect is not observed for higher gate-wire distances. The main findings indicating the gate effect are summarized in Fig. 6.2 and are as follows:

- Switching current suppression: The average switching current remains unaltered at voltages below a threshold, and then starts to decrease monotonically. The suppression is bipolar in the gate voltage, although not always symmetric.

- Switching current distribution: The switching current distribution broadens from its non-gate voltage counterpart [196, 205, 207]. This broadening does not correspond to thermal equilibrium broadening, which indicates a non-equilibrium state induced in the weak-link. This is a very important hallmark, as it excludes any model of simple thermal Joule heating.

- Temperature and spatial dependence: The suppression is less effective as the temperature increases, and the gate voltage threshold also increases. The spatial decay is reported to extend over a typical length scale of $\sim 1\,\mu$m [192, 205].

- Materials: The gating effect has been demonstrated for various superconducting materials, including Ti, Al, Nb, Vd, superconductors epitaxially grown, and proximitized metals. The processing of the material (i.e., lifted-off or etched) might be relevant. On one hand, the lateral profile of the material can be different, with lifted-off materials leaving a less smooth and rougher surface compared to etched devices, and thus can produce locally higher electric fields. On the other hand, lifted-off processes are naturally more prone to contamination, with potential residues left on the substrate.

- Impact on the phase: Two works reported measurements of the gating effect in SQUID devices [194, 208]. A reduction of the critical current of the device, an increase in the current noise, and a shifting of the SQUID interference pattern are observed, indicating a non-trivial impact on the superconducting phase.

- Leakage current: The gating effect is correlated with an exponential-like increase in leakage current I_L flowing from the gate to the wire [142, 202, 203, 205]. The amount of leakage depends on the substrate, with Si and SiO_2 substrates being more prone to high values of leakage compared to Sapphire. For lower gap materials like Ti, the increase in leakage does not always occur concomitantly with the threshold voltage for supercurrent suppression (see also Fig. 6.2c). Two studies [209, 210] have shown suppression in suspended wires or with ionic gating, where the effects of leakage current should be reduced.

6.3. PROPOSED EXPLANATIONS

There is an ongoing debate regarding the underlying mechanism behind gate-controlled superconductivity. Several hypotheses have been proposed, each of which could contribute to the observed effect. The relative importance of these mechanisms may vary, and understanding their individual role could help unravel the complex interplay of factors at play. The main hypotheses, illustrated in Figure 6.3, include:

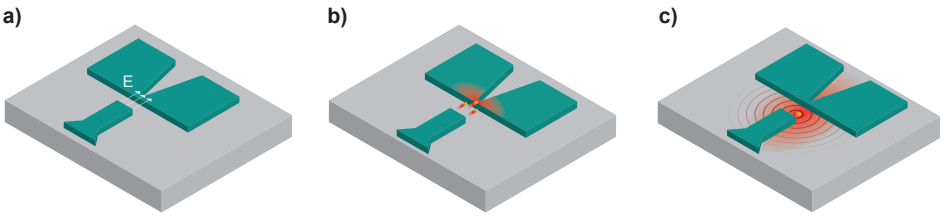

Figure 6.3: Illustrations of different possible mechanisms involved in gating-induced supercurrent suppression, which may occur simultaneously. a) Purely electrostatic field effect. b) High-energy electrons leaking from the gate, flowing through the substrate or vacuum, and relaxing into the weak-link. c) High-energy electrons injected into the substrate, generating out-of-equilibrium phonons that relax in the weak-link.

1. Electric field-effect: This is a purely electrostatic field effect associated with the applied gate voltage V_G. The necessary values of E are typically in the range of $\sim$ GV/m. Several theories have been formulated, which mostly focus on electrically driven effects at the surface of the superconductors, which become relevant when the thickness of the film is of the order of the superconducting coherence length $\sim \xi_0$. These theories include induced surface orbital polarization due to spin-orbit coupling effects, surface depairing by magnetic impurities, or pair-breaking phenomena due to Schwinger-like effects [198, 199, 211].

2. High-energy electrons: The emission of high-energy electrons of energies $\sim$ eV from the gate through vacuum or the substrate that impinge on the superconductor and relax, generating quasiparticles [202–205]. Direct evidence of this phenomenon comes from a small leakage current (typically of the order of pA - nA) flowing from the gate to the constriction. This scenario is similar to the hotspots created by photons on superconducting nanowire single photon detectors [212, 213]. The specific mechanisms leading to the leakage current flow can be different, including Schottky emission into the substrate or Fowler–Nordheim emission from the metal either to the vacuum or the substrate.

3. Out-of-equilibrium phonons: Out-of-equilibrium phonons are generated when the high-energy electrons discussed in (2) partially relax into the substrate, exciting non-thermal phonons [206]. These phonons can reach the nanowire and then relax, generating quasiparticles. This mechanism is qualitatively similar to high-energy particle events in superconducting quantum processors and microwave resonators, where cosmic or gamma rays hit the substrate, propagate as phonons, and reach the superconductors [214, 215]. It is still not clear what the relative weight of this process is compared to the former. The only study on this phenomenon has investigated only Si substrate and reported phonons traveling up to a distance of $\sim 1 - 2$ μm [206].

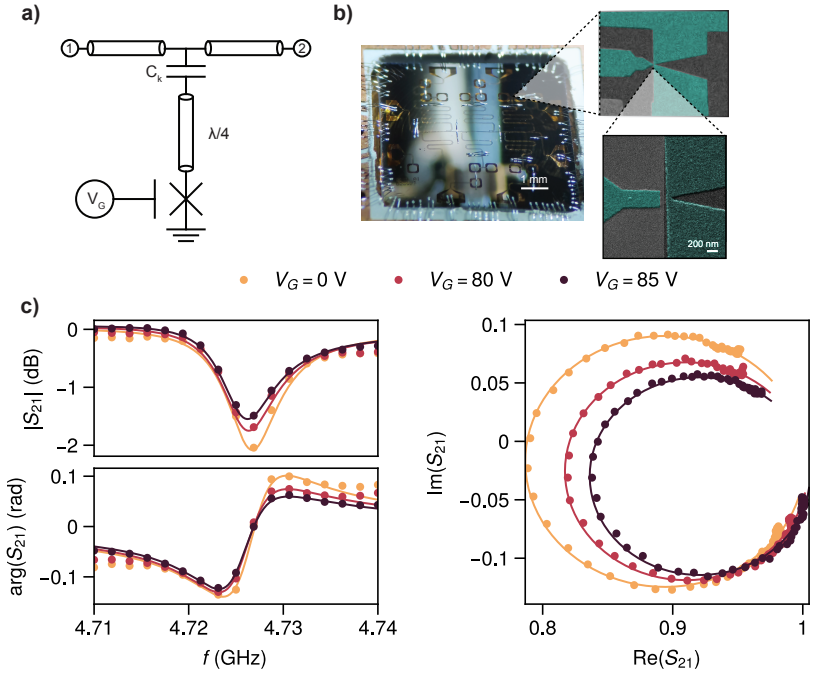

Figure 6.4: a) Circuit schematic of a notch-coupled $\lambda/4$ resonator coupled to a feedline. The resonator is shorted to ground via the weak-link, which provides tunable inductance when a gate voltage (V_G) is applied. b) Optical and SEM images of the chip and the microwave resonator section shorted to ground. The magnification is a zoom-in of the weak-link region. c) Transmission S_{21} for different values of gate voltage V_G. The solid lines represents the corresponding fit (Eq. 6.1). The extracted values of f_r, Q_{int} and Q_{ext} are shown in Fig. 6.5 for the full range of applied V_G.

6.4. GATED MICROWAVE RESONATORS

In this thesis, we further elucidated some of the possible mechanisms behind the gate induced suppression. We present a detailed study of the impedance changes in gated Dayem-bridges achieved by embedding them into a microwave resonant network. We monitored the real-time change in the network's scattering parameters as a function of the applied gate voltage. This design has been motivated by different factors:

- It allows probing both the inductive and reactive part of the Dayem-bridge, monitoring not only a decrease in its critical current (hence increase in its inductance), but also any possible increase in the dissipation, which are more indicative of scenarios 2 and 3.
- Microwave resonators are a crucial building block in the context of superconducting qubits and detectors. The realization of fully metallic gate-tunable microwave resonators, regardless of the microscopic origin behind the gate tunability, can hold great promise for potential applications.
- At the time of our research, there is only one published result on the gating effect with microwave resonators, pointing towards a leakage-induced mechanism [203]. However, this result was obtained on a SiO_2 substrate, which is more prone to leakage compared to Sapphire and has never been replicated.

Fig. 6.4a shows the circuit schematic, which consists of a $\lambda/4$ coplanar waveguide resonator terminated to ground via a Dayem-bridge. The gate voltage allows to change the Dayem-bridge impedance $Z = R + i\omega L$ by altering either the wire's inductance ($L \propto 1/I_c$) or the dissipation R, thereby modifying the amplitude and phase of the microwave probe signal transmitted past the circuit. By notch-coupling the resonator to a feedline, we are able to multiplex multiple devices.

The devices were fabricated in a single lift-off step on a highly insulating Sapphire substrate, on which 25 nm of Aluminium were deposited via an electron beam evaporator with a base pressure of $\sim 10^{-11}$ Torr. The gate voltages were applied using single coaxial lines with high dielectric resistance above 1 TΩ at room temperature.

6.4.1. GATING

Figure 6.4 shows the transmission S_{21} of a resonator with a center frequency of $f_r = 2\pi\omega_r = 4.72$ GHz at different values of the applied gate voltage $V_G = (0, 80, 85)$ V. The gate-wire separation is ~ 70 nm. Each panel displays the magnitude, phase and the complex resonator scattering data. Solid lines represent the fits obtained for the complex data with the expression:

$$S_{21} = 1 - \frac{\kappa_e}{\kappa_i + \kappa_e + 2i\delta} = 1 - \frac{1/Q_{ext}}{1/Q_l + 2i(f/f_r - 1)}, \tag{6.1}$$

which allows to extract the resonance frequency f_r and the internal and external Q-factors, Q_{int} and Q_{ext}.

Figure 6.5a and b display the full transmission spectra of two resonators with center frequencies of $f = 4.72$ GHz and 8.67 GHz as a function of the applied gate voltage V_G. The behavior of the resonance frequency f_r and internal Q-factor Q_{int} as a function of

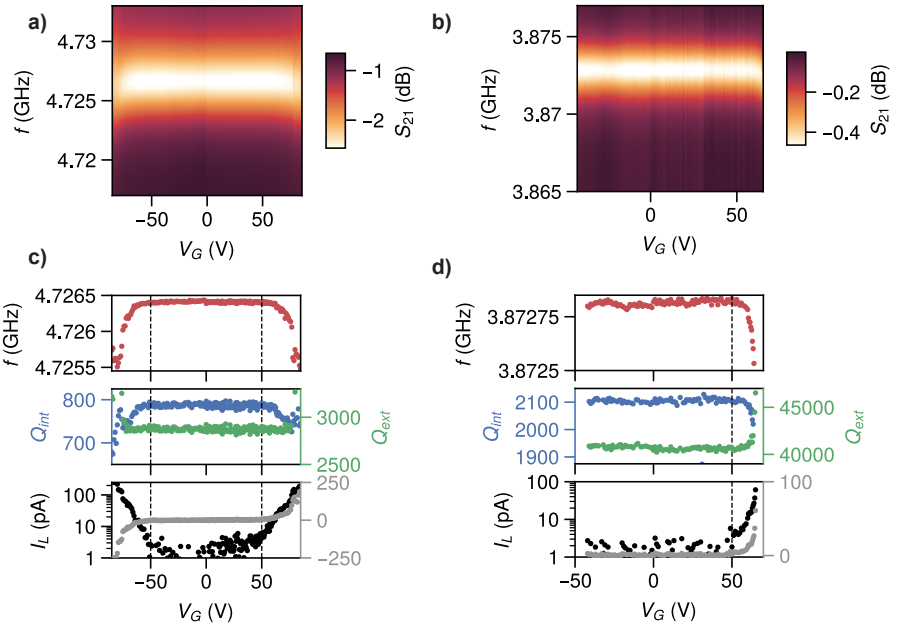

Figure 6.5: a) and b) Magnitude of the transmission coefficient S_{21} as a function of the gate voltage V_G for two resonance frequencies. c) Top: resonance frequency f_r, center: internal and external quality factor Q_{int} and Q_{ext}, and bottom: leakage current I_L as a function of V_G. The values of f_r, Q_{int} and Q_{ext} are extracted from the fit of the complex data (Eq. 6.1).

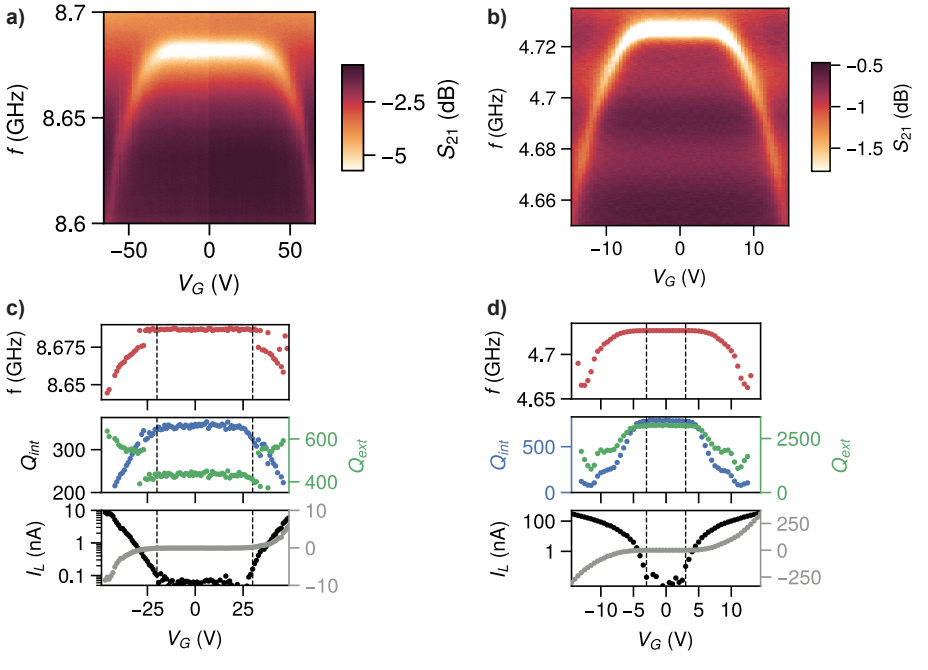

Figure 6.6: a) and b) Magnitude of the transmission coefficient S_{21} as a function of the gate voltage V_G for two resonance frequencies after a soft-breakdown event happened. c) and d) Top: resonance frequency f_r, center: internal and external quality factor Q_{int} and Q_{ext}, and bottom: leakage current I_L as a function of V_G. The values of f_r, Q_{int} and Q_{ext} are extracted from the fit of the complex data (Eq. 6.1).

V_G, extracted as explained above, are shown in Fig. 6.5c and d. During the measurement, the leakage current I_L flowing from the gate is also recorded as 100 averages of the current provided by the gate source and is plotted in the bottom row in log (black) or linear (gray) scale. The resonance frequency exhibits a bipolar shift towards lower frequencies with increasing gate voltage, indicating an increase in the wire inductance. The internal Q factor Q_{int} decreases, indicating an increased dissipation in the wire. This trend is evidently correlated with an approximately exponential increase in I_L for $|V_G| > 50\,\mathrm{V}$.

6.4.2. GATING AFTER SOFT-BREAKDOWN

During the gate sweeps, the application of high electric field conditions on the metal and substrate can result in significant device instabilities. We have observed instances where sudden modulation occurs simultaneously with a spike in the leakage current, even after several sweeps with no apparent effects. This behavior can cause irreversible changes to the device, resulting in modest leakage currents at lower threshold voltages. Previous studies, such as Elalaily et al. [216], have also described this behavior and it emphasizes

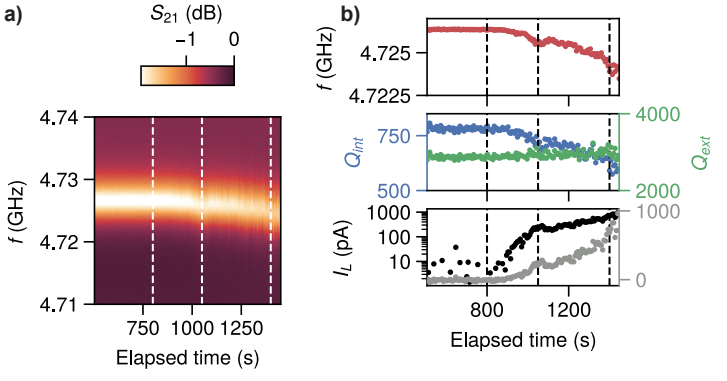

Figure 6.7: a) Transmission spectrum as a function of elapsed time when a gate voltage $V_G = 100\,\text{V}$ is applied to the gate line. b) Top: resonance frequency f_r, center: internal and external quality factor Q_{int} and Q_{ext}, and bottom: leakage current I_L as a function of elapsed time.

the importance of monitoring the leakage current flow throughout the experiment.

In Figure 6.6, we present two examples of this phenomenon, where device (a) is less affected by the breakdown than device (b). The frequency shift achieved in terms of modulation is on the order of $\Delta f \sim 100\,\text{MHz}$, and the threshold voltages at which this modulation occurs are $V_G \sim 25\,\text{V}$ and 5 V, respectively. These results suggest that the considerable variation in the reported threshold gate voltages in literature, after accounting for differences in the substrate used, is also likely related to phenomena of soft dielectric breakdown. We have obtained analogous results for identical wires measured in DC on the same Sapphire substrates.

In Figure 6.7, we demonstrate our ability to track and detect the development of the soft-breakdown process thanks to the high-sensitivity provided by the resonator design. The data shows the spectrum of the resonator depicted in Figure 6.6(b) before the breakdown occurred. We measured the spectrum as a function of elapsed time when the gate was left fixed at a voltage of $V_G = 100\,\text{V}$. We observed a shift in f_r and Q_{int} after approximately $t \sim 800\text{s}$, coinciding with an increase in the leakage current $I_L \sim 10-100\,\text{pA}$. As time progressed, the leakage increased considerably until we stopped the measurement. When we repeated the gate sweep, we observed modulation occurring for threshold voltages as low as 5 V, as already discussed in Fig. 6.6(b).

6.4.3. NON-LOCAL GATING EFFECTS

While previous results have focused on the effect of gate lines on nearby resonators, we also conducted experiments to investigate the impact of gating a single weak-link while monitoring all six resonators on the chip simultaneously. Figure 6.8 illustrates our findings. We applied the gate voltage on line #4 while tracking all the resonances in real time. We found that there was no frequency shift recorded for $V_G < 47\,\text{V}$, but a shift was observed in all resonators across the 7×7 mm chip when V_G reached 47 V. This shift was accompanied by a spike in leakage current, which reached a value of $\sim 100\,\text{pA}$.

Our observations are compatible with the generation of high-energy phonons in the

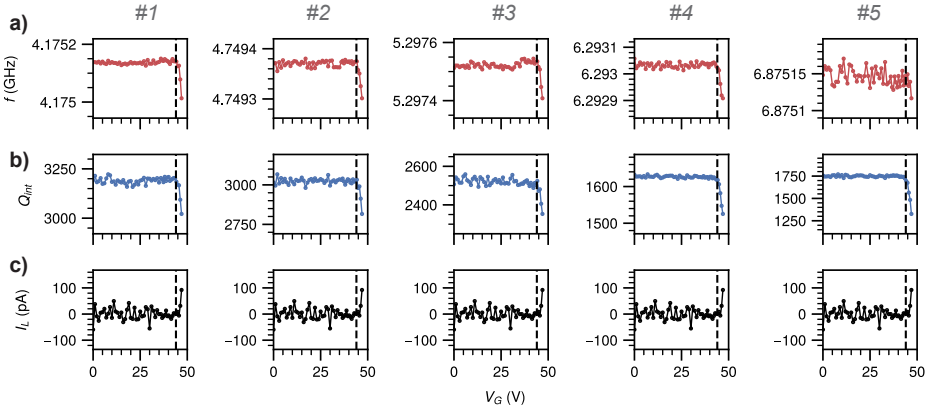

Figure 6.8: Top: resonance frequency f_r, center: internal quality factor Q_{int}, and bottom: leakage current I_L as a function of V_G. The gate is applied to resonator #4 while monitoring the transmission on all the resonators on the chip measured at the same time.

substrate emitted from the highly energetic leakage current spike, similarly to what was reported in [206]. A single electron with energies in the range of a dozen eV can produce a considerable amount of energetic phonons in most dielectrics (which have typical maximum energies $\sim$ meV). Part of these phonons can either relax into the nearby metal, creating quasiparticles, or reach other parts of the sample traveling through the substrate and relaxing at the other weak-links. Indeed, the phonons can propagate through the substrate ballistically over centimeter scales, as also observed in high-energy events recorded on superconducting qubits [215] and in phonons injected from voltage-biased tunnel junctions [217–220].

We did not observe a significant trend that correlated the resonator shifts with their position on the chip with respect to the injection point, which would probably require higher sensitivity and control over the stability of the injection mechanism. Indeed, also in this case, the intense electric field led to a soft breakdown of the substrate, resulting in the formation of a resistive current channel at the gate line, and with subsequent gate sweeps leading to the heating of the entire sample.

6.5. SYSTEMATIC REVIEW

This section presents a systematic review of experimental data on gated superconducting nanowires measured in a standard DC configuration. The review compares different device properties, including materials, substrates, and leakage currents. The meta-analysis includes all the data published in literature and the data obtained during this work, which are available in the Additional material.

Figure 6.9a (left) shows the dependence of the electric field at full suppression, E, as a function of the employed substrate (Si in blue, SiO_2 in green, Al_2O_3/Sapphire in red) and the gate-wire separation d. For simplicity, we define $E = V/d$, where V is the gate voltage at full suppression, if available, or at the highest suppression point reached, and

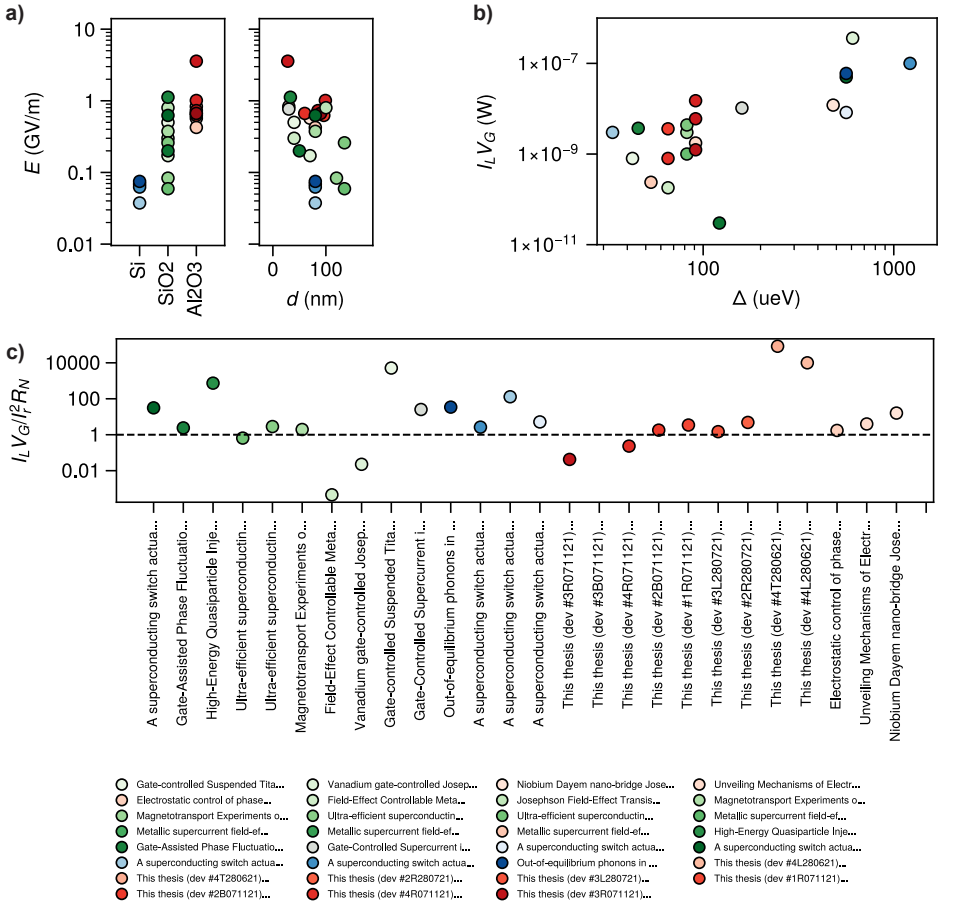

Figure 6.9: a) Electric field E at full supercurrent suppression as a function of the substrate (left) and the gate-wire distance d (right). b) Power dissipated by the gate, $I_L V_G$, at full suppression as a function of the superconducting gap Δ. c) Ratio between the power dissipated by the gate, $I_L V_G$, and the power at the retrapping current, $I_r^2 R_N$, for different devices. The dashed line indicates a ratio equal to 1. All data were extracted from the corresponding publications shown in the legend at the bottom. The colors indicate the different substrates: blue for Si, green for SiO_2, and red for Al_2O_3 (Sapphire).

d is the wire-gate distance. The majority of devices have E values in the range of 0.1 to 1 GV/m (1 to 10 MV/cm), which are close to the electrical breakdown of the substrates. The lowest E values were found for devices with Si substrates, where onset of the leakage current is determined by the Schottky barrier at the metal-semiconductor interface. The E values for devices on SiO_2 showed great variability, which can be attributed to the different thicknesses and qualities of the oxides. Devices made on Al_2O_3 required the highest electric field to suppress the supercurrents in agreement with the highest resistivity of Sapphire compared to the other substrates. In Figure 6.9a (right), we compare E with the gate-wire separation d. We do not observe any trend, expected for a purely electrostatic field effect, where a lower magnitude of electric field suppression E would be expected for smaller d.

In Figure 6.9b and 6.9c, we compare the impact of suppression in terms of the relevant energy scales in the system. Figure 6.9b compares the superconducting gap $\Delta = 1.764 k_B T_c$ of the devices, where T_c is their critical temperature, with the power delivered by the gate leakage current at full suppression, $I_L V_G$. The majority of studies have focused on materials with lower gaps, such as Ti or proximitized metals, where $\Delta < 100$ μeV. In addition, there is a positive correlation between the gap and the power delivered by the gate at full suppression: devices with higher gaps typically require more power to be delivered by the gate to achieve suppression.

Figure 6.9c compares the gate-injected power, $I_L V_G$, to the power at the retrapping current, $I_r^2 R_N$, where R_N is the wire's normal state resistance. The quantity $I_r^2 R_N$ provides an estimate of the minimum thermal power required to maintain the wire in its normal state, as the retrapping current in these wires is mainly influenced by heating. The ratio $I_L V_G / I_r^2 R_N > 1$ indicates devices in which the power delivered by the gate leakage current alone may be sufficient to suppress the supercurrent. Here, we assume that the leakage current will only be dissipated in the wire, ignoring the dissipation in the substrate. Most of the devices lie above the dashed line $I_L V_G / I_r^2 R_N = 1$, suggesting that the gate leakage current alone may be sufficient to suppress the supercurrent in many cases. It is worth emphasizing again that gate suppression is a non-equilibrium phenomenon. Therefore, the injected power is not dissipated into a thermal equilibrium state in the superconductor, but it is likely inducing non-equilibrium hotspots. About 5 out of 25 devices show values of $I_L V_G / I_r^2 R_N < 1$, indicating the possibility of a non-leakage related suppression.

Although this analysis provides valuable insights, it has some limitations. Firstly, our comparison was made at the maximum achieved supercurrent suppression, but lower gate voltages were already sufficient to reduce the supercurrent. Consequently, the gate-injected power at threshold voltages could be much smaller. Secondly, in some cases, the leakage current can include a background contribution from cabling and setup, which could lead to an overestimation of the product $I_L V_G$ in certain devices. On the other hand, as discussed earlier, the reported leakage current values in the literature may have been measured before a soft breakdown event occurred, which could result in an underestimation of the true value. Despite these limitations, we found a ubiquitous correlation in the increase in the leakage current and supercurrent suppression in all works analyzed, suggesting that the former plays a significant role in the observed phenomenon.

6.6. CONCLUSIONS

In conclusion, we studied the gate-induced suppression of supercurrent in metallic superconducting Dayem-bridges. We fabricated thin-film metallic $\lambda/4$ microwave resonators with embedded gated nanowire constrictions, which allowed us to monitor the changes in the real and imaginary components of the nanowire under gating. We demonstrated the tuning of the resonator frequencies, achieving modulation from 1 MHz up to 100 MHz. We confirmed that, even when employing highly insulating Sapphire as a substrate, the gate suppression is correlated with an onset of an increase in the gate leakage currents. We observed preliminary evidence of non-local modulation induced by phonons extending over the entire chip area when a single gate line influenced multiple resonators on the same chip. Finally, we highlighted the role of soft breakdown processes of the substrate that can affect the stability and reproducibility of the supercurrent tunability.

Further investigation is needed, especially to investigate the time-resolved dynamics of the gate suppression, which has the difficult task of unraveling the complex interplay between the high-energy electron injection, the subsequent partial relaxation into the substrate and the quasiparticle diffusion and recombination processes in the superconductor. A true electrostatic field effect on the superconductor might be present, but could be masked by the aforementioned mechanisms that seem to dominante in solid-state platforms.

From a technological perspective, further work should explore optimal strategies for integrating the gate tuning effects for its potential applications in superconducting quantum devices. For instance, to realize high frequency superconducting switches, frequency-tunable resonators and couplers, and gate-controlled parametric amplifiers while minimizing power dissipation or limiting unwanted cross-talk caused by phonon excitations. This would require optimization of substrates, material choice, and nanowire geometry.

6.7. ADDITIONAL MATERIAL

6.7.1. DC SAMPLES

We present additional characterization on nominally identical wires measured using standard four-wire measurements. The Dayem-bridge geometry of the wires was the same as the one embedded in the microwave resonators presented before. Each plot below shows the forward and backwards dV/dI curves, as well as the leakage current I_L, as a function of gate voltage V_G at a temperature of $T = 35\,\mathrm{mK}$. We measured I_L as described in Section 3.2.3 to achieve the best accuracy, and exclude additional potential leakage paths in the setup. We will only present devices that showed some modulation under gating, which represent approximately 20% of the measured devices. We used different material combinations during this work, using both lift-off and etching techniques, including Titanium, Aluminum, and Niobium. In many instances, a sticking layer of Ti was employed, significantly enhancing adhesion. However, in certain cases, this resulted in a decrease in the superconducting gap of the parent material due to the inverse proximity effect. Figure 6.10, 6.11, 6.12, and 6.13 provide a summary of the results obtained under gating for each material.

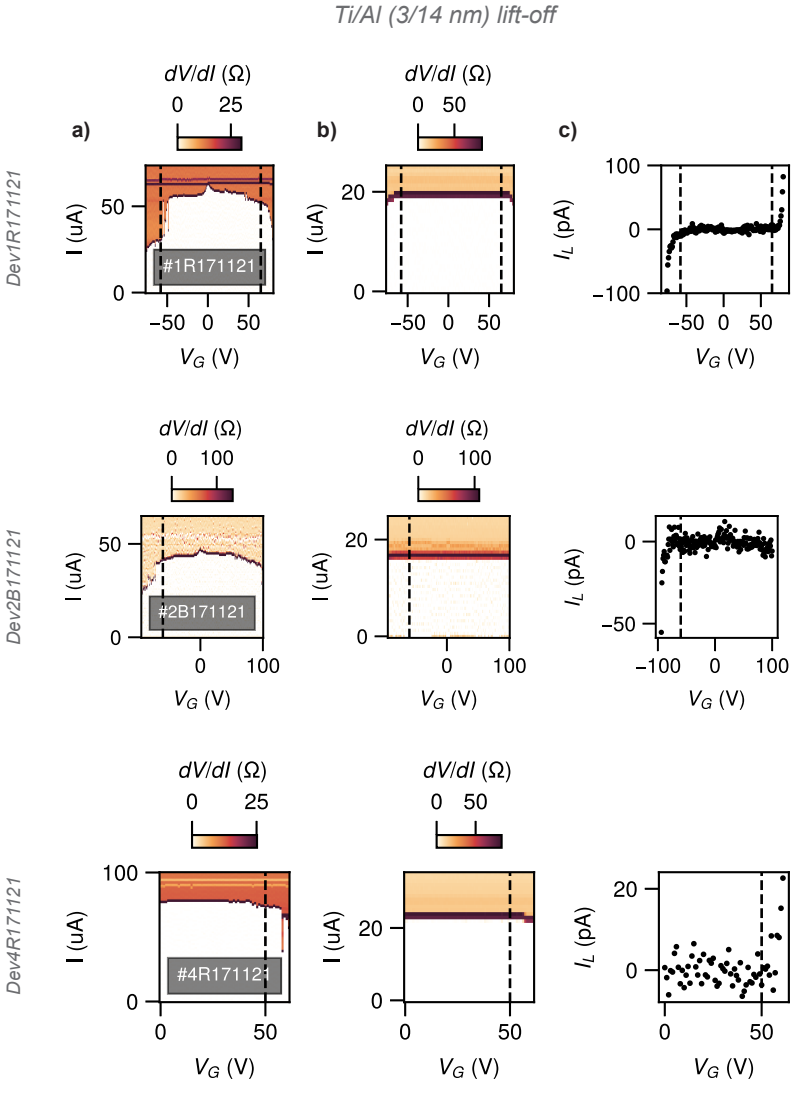

Figure 6.10: Ti/Al Dayem-bridges with a thickness of 3/14 nm fabricated using lift-off. a) and b) Differential resistance dV/dI curves are shown as a function of the gate voltage V_G for both forward and backward current biases. The boundary between the white and colored regions indicates the switching and retrapping current. c) Leakage current I_L.

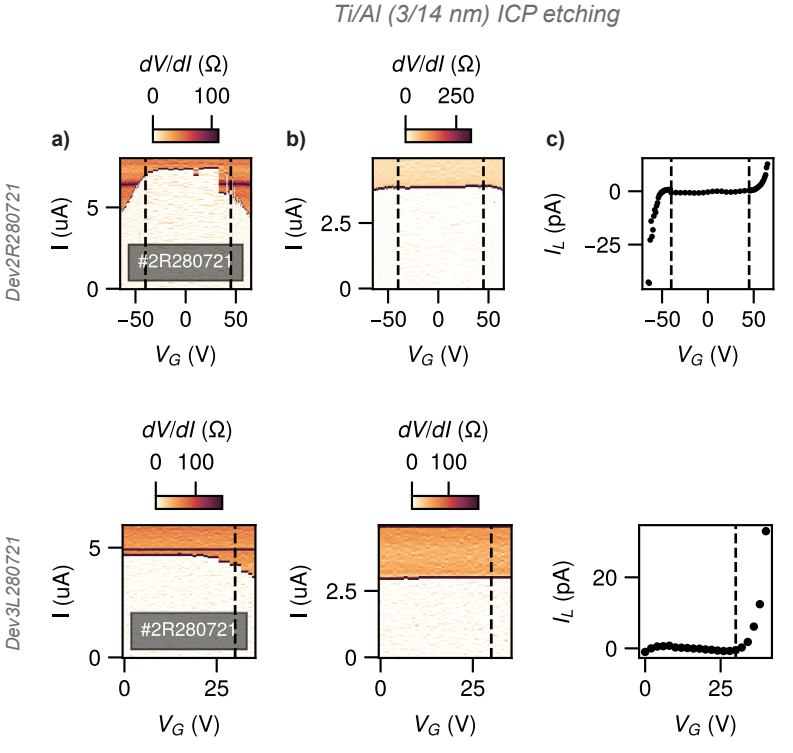

Figure 6.11: Ti/Al Dayem-bridges with a thickness of 3/14 nm fabricated using ICP-RIE etching. a) Differential resistance dV/dI curves are shown as a function of the gate voltage V_G for both forward and backward current biases. The boundary between the white and colored regions indicates the switching and retrapping current. c) Leakage current I_L is also shown.

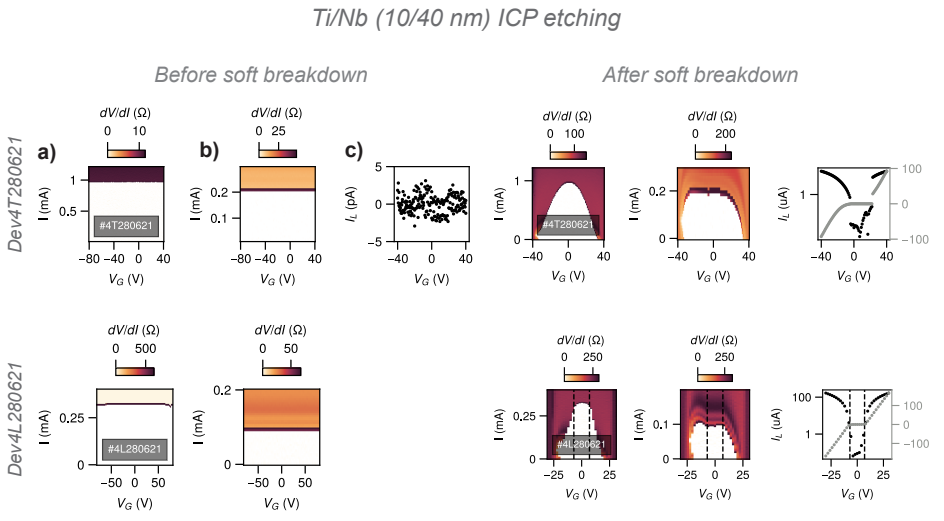

Figure 6.12: Ti/Nb Dayem-bridges with a thickness of 10/40 nm fabricated using ICP-RIE etching. a) Differential resistance dV/dI curves are shown as a function of the gate voltage V_G for both forward and backward current biases. The boundary between the white and colored regions indicates the switching and retrapping current. c) Leakage current I_L is also shown. The figure shows data before and after substrate breakdown in the left and right region, respectively.

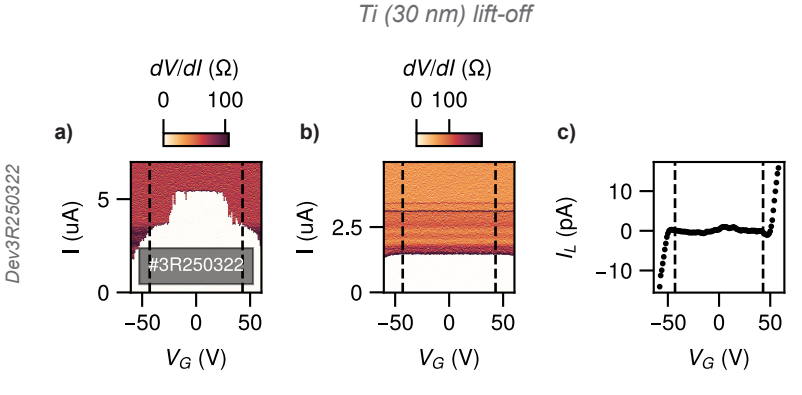

Figure 6.13: Ti Dayem-bridges with a thickness of 30 nm fabricated by lift-off. a) Differential resistance dV/dI curves are shown as a function of the gate voltage V_G for both forward and backward current biases. The boundary between the white and colored regions indicates the switching and retrapping current. c) Leakage current I_L is also shown.

6.7.2. MICROWAVE IRRADIATION AND GATING

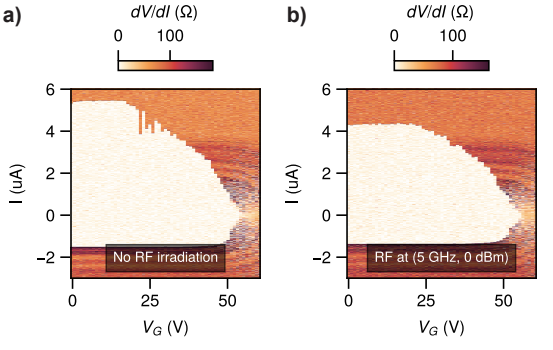

Figure 6.14: a) dV/dI curves as a function of gate voltage V_G for the Ti weak-link in the absence of microwave irradiation. b) dV/dI curves for the same device as in a) when irradiated with microwaves at a frequency of $f = 5$ GHz.

Figure 6.14 shows the measurements on the Ti-based weak link shown in Fig. 6.13 when we applied a static gate voltage V_G and exposed the weak link to microwave irradiation via an open-end coax antenna placed close to the sample. The left plot shows the dV/dI curves as a function of V_G without microwaves, indicating complete suppression of the supercurrent at $V_G \sim 50$ V. The right plot shows the same dV/dI curves when the Ti weak-link was irradiated at a frequency of $f = 5$ GHz. However, we did not observe any additional effects related to the gate-induced suppression, nor did we observe any form of phase locking, such as Shapiro steps. The microwave irradiation had a minor effect of reducing the wire critical current. Additional measurements at a range of microwave frequencies and powers give analogous results.

6.7.3. NON-LINEAR DAYEM-BRIDGE RESPONSE

The weak-link inductance of the Dayem-bridge resonator exhibits a nonlinear dependence on the current flowing through it, as given by Eq. 2.30. This can be approximated as $L_J(I) = L_{J,0}(1 + I^2/I_c^2)$, where I_c is the critical current that determines the scale of the nonlinearity. This effect is also known as Kerr or Duffing nonlinearity [221–223]. As a result, the resonator shows a nonlinear response when driven by high-power input.

A hallmark of Kerr nonlinearity is the distortion of the transmission spectrum at high powers, which leads to a multivalued response above a critical power known as the bifurcation point. In Fig. 6.15a, we present the power dependence of the transmission data, which shows the characteristic low frequency shift and distortion of the resonator frequency from $P = -75$ dBm. As the power increases, the resonance bifurcates into two stable states with distinct oscillation amplitudes, as shown in Fig. 6.15b for the forward frequency sweep direction.

To further explore the nonlinear dynamics, we introduce degenerate four-wave mixing by applying a pump tone with a detuning ($\delta = f_p - f_r$) from the resonator frequency $f_r = 3.785$ GHz and a low-power signal at a fixed detuning ($\Delta = f - f_p = 125$ kHz)

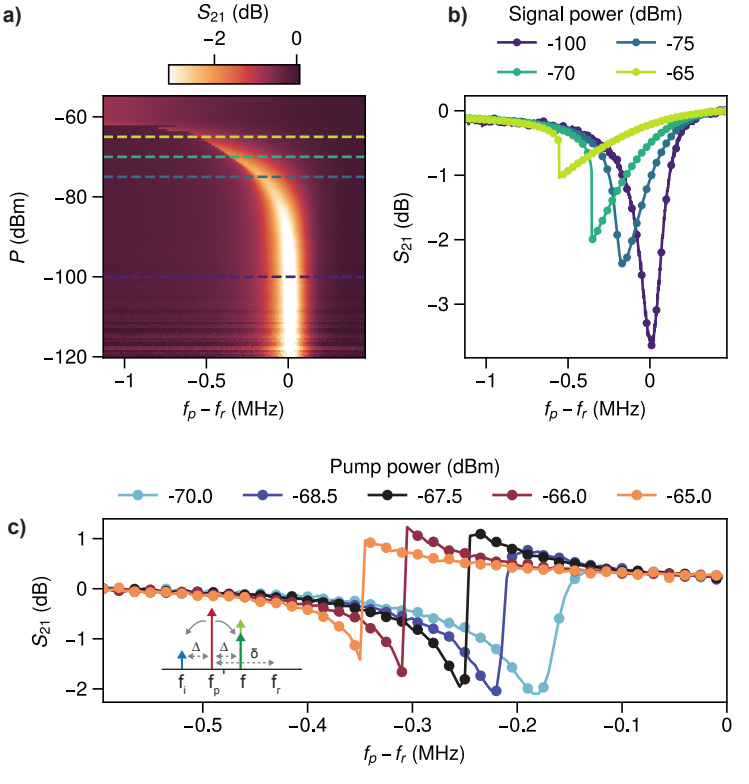

Figure 6.15: a) Transmitted signal S_{21} as a function of frequency and power. At high power, the distortion of the resonance curves is indicative of bifurcation. b) Selected traces of the transmitted signal S_{21} for different values of power. c) Signal tone S_{21} when an additional strong pump tone is present and detuned by $\Delta = 125\,\mathrm{kHz}$ from the signal.

from the pump tone. As illustrated in Fig. 6.15c (inset), two pump photons will be mixed into a signal and an idler photon. We measure the pump-signal conversion in Fig. 6.15c, where we observe a small gain of the propagating signal, which is limited by the device design and internal losses.

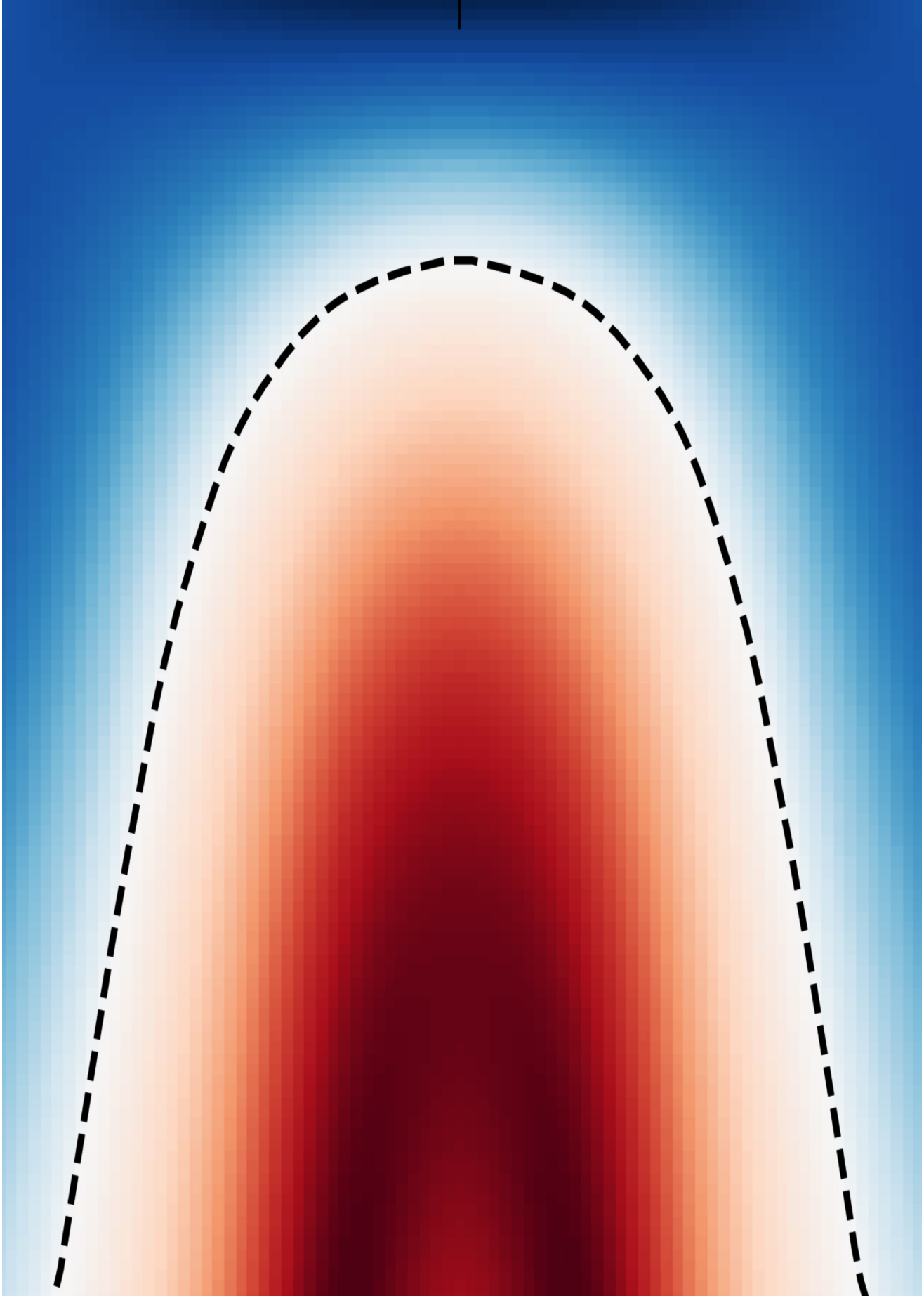

7

Photonic heat rectification in a coupled qubits system

We theoretically investigate a quantum heat diode based on two interacting flux qubits coupled to two heat baths. Rectification of heat currents is achieved by asymmetrically coupling the qubits to the reservoirs modelled as dissipative RLC resonators. We find that the coherent interaction between the qubits can be exploited to enhance the rectification factor, which otherwise would be constrained by the baths temperatures and couplings. Remarkably high values of rectification ratio up to $\mathcal{R} \sim 3.5$ can be obtained for realistic system parameters, with an enhancement up to $\sim 230\%$ compared to the non-interacting case. The system features the possibility of manipulating both the rectification amplitude and direction, allowing for an enhancement or suppression of the heat flow to a chosen bath. For the regime of parameters in which rectification is maximized, we find a significant increase of the rectification above a critical interaction value which corresponds to the onset of a non vanishing entanglement in the system. Finally, we discuss the dependence of the rectification factor on the bath temperatures and couplings.

7.1. Introduction

The recent development of quantum technologies brought an increasing interest in the experimental and theoretical investigation of heat transport at the nanoscale [224–227]. In this context, phenomena such as phase coherence and entanglement are currently actively studied as they could potentially lead to quantum advantages, e.g., in terms of improved performance of thermal machines [228] and devices [229–232], including refrigerators [233–236], heat switches [237–241], heat engines [242–248], thermal accelerators [249], and towards genuine quantum thermal machines producing entanglement [250–252]. A topic of great interest in this context is thermal rectification i.e., the lack of reversal symmetry of heat current under the reversal of the temperature gradient established between two thermal reservoirs. A finite rectification means that the magnitude of the thermal powers changes as the direction of the heat current gets reversed. Su-

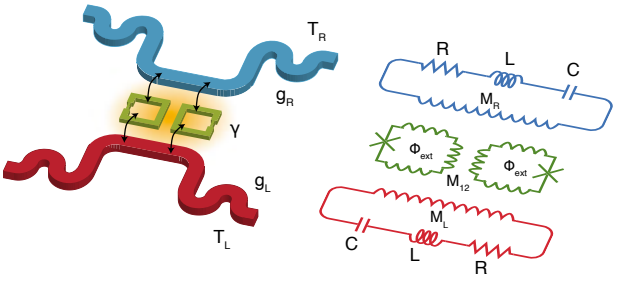

Figure 7.1: Left: graphic illustration of the qubit heat diode. Two interacting flux qubits (green) are mutually coupled to each others via the inductance M_{12} and to two thermal reservoirs with coupling factors $g_{L,R}$. The two reservoirs reside at temperature T_L and T_R (red and blue). Right: circuit diagram corresponding to the investigated system.

perconducting hybrid devices offer outstanding performance regarding electronic heat rectification and highest values of rectification have been reported in systems composed by tunnel junctions between different superconductors/normal metals [226, 253–256], topological insulators [197] and ferromagnetic insulators [257]. While typically electronic heat conduction is considered at low temperature, also the radiative channel can be significant or even dominant in certain designs [237, 248, 258–261]. Photonic heat flow is important, for instance, when applying circuit quantum electrodynamics (cQED) schemes to the thermal regime with the potential to study quantum heat transport with remarkable control and precision [224, 262, 263]. This emerging field of superconducting circuit quantum thermodynamics (cQTD) has already achieved a number of relevant results [240, 264, 265], being significant for both fundamental study of quantum mechanics as well as for real world quantum technologies applications. The investigation of more complex schemes where the interaction and coherence among multiple qubits plays a prominent role is now actively developing [251, 266–273].

Here, we theoretically analyze a prototypical system consisting of two interacting flux qubits coupled to two environmental photonic baths, as sketched in Fig. 7.1. The two qubits are inductively coupled to each other and asymmetrically to the two baths which are modeled as RLC oscillators. This system, which has been previously investigated as a heat switch [239], can behave as a photonic thermal diode whose rectification factor can be greatly enhanced by the qubits interaction. Moreover, we show that not only the amplitude, but also the direction of rectification can be manipulated, allowing to switch from configurations in which heat flow is favored or suppressed. The high tunability provided by the magnetic flux provides a convenient knob for the control of both the rectifying amplitude and direction. Tunable inductive couplings can allow a further control of the mutual interaction between the qubits themeselves and between qubits and reservoirs [274].

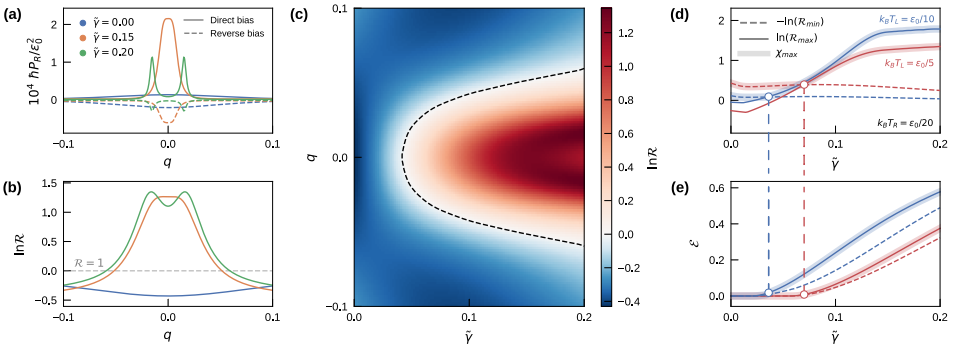

Figure 7.2: a) Normalized power $\hbar P_R^{\pm}/\epsilon_0^2$ transmitted to the right bath as a function of the dimensionless applied external flux q for different values of interaction $\tilde{\gamma} = \gamma/\epsilon_0$. Continuous/dashed lines indicates the direct and reverse thermal bias configuration with $k_B T_L = \epsilon_0/5$ and $k_B T_R = \epsilon_0/20$. b) Rectification ratio $\mathcal{R} = |P_R^+/P_R^-|$ extracted from the curves in a). The grey dashed line indicates absence of rectification. c) Full dependence of $\mathcal{R}$ as a function of q and $\tilde{\gamma}$. The dashed black line over the white area corresponds to points of absence of rectification ($\mathcal{R} = 1$). Red and blue areas correspond, respectively, to regions of direct and reverse rectification direction. d) Maximal rectification χ_{max} as a function of $\tilde{\gamma}$ for different T_L at fixed $k_B T_R = \epsilon_0/20$ is shown as an highlighted curve. The solid and dashed lines corresponds to the quantities $\ln \mathcal{R}_{max}$ and $-\ln \mathcal{R}_{min}$. The turning points at $\tilde{\gamma}_c$, associated with a switch of the rectification direction, are shown as white circles. The red curve corresponds to the temperature bias shown in c). e) Entanglement $\mathcal{E}$ corresponding to the same parameters values of d). In all plots, $\epsilon_0 = 1, \Delta = 0.1, \hbar\omega_{LC} = 10\epsilon_0, Q_L = Q_R = 10, R_L = R_R = 1\,\Omega, g_L = 0.75, g_R = 0.25$ are assumed.

7.2. MODEL

The full Hamiltonian describing the two interacting qubits with the dissipative environments reads

$$H = H_S + H_{S,L} + H_{S,R} + H_L + H_R, \tag{7.1}$$

where H_S is the Hamiltonian of the two interacting qubits, $H_{S,L/R}$ are the qubit-bath interaction and H_L and H_R are the bare baths Hamiltonians, which we shall model as sets of harmonic oscillators. The Hamiltonian of the interacting qubits reads

$$H_S = H_0 + H_{12}, \tag{7.2}$$

with H_0 being the two non-interacting flux qubits Hamiltonian and H_{12} the interaction between them. The first term reads [275]

$$H_0 = \sum_{i=1}^{2} -\epsilon_i (q\hat{\sigma}_{z,i} + \Delta_i \hat{\sigma}_{x,i}), \tag{7.3}$$

where $\epsilon_i = I_{p,i}\Phi_0$, with $I_{p,i}$ the circulating current and Φ_0 the superconducting flux quantum, Δ_i are the dimensionless tunneling amplitudes, $q = (\Phi_{ex}/\Phi_0 - \frac{1}{2})$ is the dimensionless applied external magnetic flux and $\hat{\sigma}_{\alpha,i}$ with $\alpha = \{x, y, z\}$ denote the

Pauli matrices of qubit i. The qubits are inductively coupled to each other so that the corresponding interaction takes the form

$$H_{12} = \gamma \hat{\sigma}_{z,1} \hat{\sigma}_{z,2}, \tag{7.4}$$

where $\gamma = 2M_{12} I_{p,1} I_{p,2}$ is the coupling strenght and M_{12} is the mutual inductance between the qubits. In the following, we will consider the condition of identical qubits, i.e., $\epsilon_1 = \epsilon_2 = \epsilon_0$ and $\Delta_1 = \Delta_2 = \Delta$, but we have checked numerically that the following discussion is not significantly affected if one allows for relative differences, up to 10%, of the qubits parameters. As represented schematically in Fig. 7.1, the two qubits are interacting with two distinct heat baths with temperatures T_L (left bath) and T_R (right bath). The dissipative environment can be conveniently modeled as an LC oscillator with a series resistance R_B which inductively couples through the $\hat{\sigma}_{z,i}$ components of the two qubits as depicted in Fig. 7.1 [237, 276]. For uncorrelated baths, the Hamiltonian describing the interaction between our two qubit system S and the bath $B = \{L, R\}$ reads [277, 278]

$$H_{S,B} = M_B I_p (\hat{\sigma}_{z,1} + \hat{\sigma}_{z,2}) \otimes \delta\hat{i}_{n,B}, \tag{7.5}$$

where the current operator $\delta\hat{i}_{n,B}$ for the environment B sets the temperature-dependent Johnson-Nyquist noise through its spectral function S_B

$$S_B(\omega) = \int_{-\infty}^{\infty} dt e^{i\omega(t-t')} \langle \delta\hat{i}_{n,B}(t) \delta\hat{i}_{n,B}(t') \rangle. \tag{6a}$$

The latter can be assessed directly from the impedance of the corresponding environment [20, 237, 276], which in our case reads

$$S_B(\omega) = \frac{2\hbar\omega}{1 - e^{-\hbar\omega/k_B T_B}} \mathrm{Re}\{Y_B(\omega)\}, \tag{6b}$$

with $Y_B(\omega) = 1/R_B[1 + iQ_B(\omega/\omega_{LC,B} - \omega_{LC,B}/\omega)]^{-1}$ being the admittance of the RLC circuit of resistance R_B and quality factor $Q_B = \sqrt{L_B/C_B}/R_B$.

7.3. PHOTONIC HEAT TRANSPORT

Heat transport is crucially determined, among other quantities, by the rate of transitions incurring in the two-qubit system S as a consequence of their coupling to the noisy reservoirs. By assuming a standard weak-coupling regime, transition rates from level k to level l of the coupled qubits system due to the bath B can be evaluated as [233, 239]

$$\Gamma_{k\to l,B} = \frac{(M_B I_p)^2}{\hbar^2} |\langle k|(\hat{\sigma}_{z,1} + \hat{\sigma}_{z,2})|l\rangle|^2 S_B(\omega_{kl}), \tag{7.7}$$

where $|n\rangle$ denotes an eigenstate of H_S, $H_S|n\rangle = E_n|n\rangle$, and $S_B(\omega)$ is the noise spectral function. In order to quantify the thermal power transmitted between the baths, we first need to further evaluate the components of the density matrix ρ of the coupled qubits system. These are governed by the master equation [239, 279, 280]

$$\dot{\rho}_{kl} = -i\omega_{kl}\rho_{kl} + \delta_{kl} \sum_i \rho_{ii}\Gamma_{i\to k} - \frac{1}{2}\rho_{kl} \sum_i (\Gamma_{k\to i} + \Gamma_{l\to i}), \tag{7.8}$$

where $\Gamma_{k\to l} \equiv \Gamma_{k\to l,L} + \Gamma_{k\to l,R}$ are the total transition rates and ρ is written in the instantaneous eigenbasis $|n\rangle$ of the coupled qubits [1]. For weak qubit-bath coupling, we can thus write the thermal power to the bath B in the form [239, 284]

$$P_B = \sum_{i,j} \rho_{ii} E_{ij} \Gamma_{i\to j,B}, \tag{7.9}$$

where $E_{ij} = E_i - E_j$ is the transition energy between eigenstates $|i\rangle$ and $|j\rangle$ and $\Gamma_{i\to j,B}$ is the corresponding transition rate induced by the bath B. We can thus quantify the rectification ratio as

$$\mathcal{R} = \left| \frac{P_B^+}{P_B^-} \right|, \tag{7.10}$$

where $P_B^\pm$ corresponds to the thermal power to the bath B in the direct/reverse thermal bias configurations and such that the absence of heat rectification corresponds to $\mathcal{R} = 1$, while $\mathcal{R} > 1$ or $\mathcal{R} < 1$ indicates a favored or suppressed heat flow to the bath B. In the steady state regime, Eq. (7.10) can be equivalently expressed in terms of the left/right reservoirs $B = \{L, R\}$.

7.4. HEAT RECTIFICATION

In the following we shall assume different qubit-bath coupling strengths for the two environments. This provides the necessary structural asymmetry to observe rectification [260, 285]. For simplicity, we quantify this coupling by the dimensionless parameters

$$g_B = \frac{M_B I_p}{\sqrt{\hbar R_B}}, \tag{7.11}$$

which are set to the values $g_R = 0.25$ and $g_L = 0.75$. Fig. 7.2a depicts the powers $P_R^\pm$ transmitted to the right bath as a function of the applied dimensionless flux q with direct thermal bias (continuous line), and reverse thermal bias (dashed line). In both cases the dimensionless power $\hbar P_R^\pm/\epsilon_0^2$ increases dramatically at $\tilde{\gamma} \equiv \gamma/\epsilon_0 = 0.15$ as a result of the resonance condition matched between the qubits energy levels and the frequency of the LC-oscillators constituting the dissipative environment [239]. More importantly, a notable variation in the intensity of the power transmitted in the direct/reverse bias configurations is observed and anticipates the significant rectifying properties of our heat diode. In Fig. 7.2b we plot $\ln \mathcal{R}$ as a function of q corresponding to the same parameter values as in Fig. 7.2a. When the qubits are non-interacting (blue line), the heat flow is always favored in the reverse thermal bias configuration, which is testified by the fact that $\ln \mathcal{R} < 0$. Moreover, in the simple case of uncoupled qubits, the rectification factor is independent on the number of qubits and depends only on $g_{L,R}$ and $T_{L,R}$ [265]. Instead, when the qubits are interacting (orange and green lines), a remarkable increase of the rectification factor is observed at $q = 0$, with an enhancement for $\mathcal{R}$ of $\sim 230\%$

[1] Note that we are describing our system by a global master equation. This is dictated by the geometry of our system, with the two qubits being directly coupled to both baths. For a configuration with the qubits in series rather than in parallel, special care must be taken in choosing whether local or global master equations should be used, see e.g. [251, 281–283].

at $\tilde{\gamma} = 0.15$ [2]. Moreover, a change in the rectification direction takes place and the system can also be tuned from forward ($\ln \mathcal{R} > 0$) to backward ($\ln \mathcal{R} < 0$) rectification by spanning q. Indeed, it turns out that the non-trivial dependence of the thermal powers on $\tilde{\gamma}$ can eventually balance and reverse the rectification direction of the qubits with respect to the non-interacting case. This feature allows the system to be fully in-situ tunable both in amplitude and direction of rectification. The complete dependence of $\mathcal{R}(q, \tilde{\gamma})$ is displayed in the colorplot in Fig. 7.2c. The dashed black line over the white area corresponds to a region of absence of rectification, while the blue and red areas correspond to regions of finite rectification, respectively with reverse and direct rectification direction. For the considered system, we clearly observe that one direction is more favorable than the other one (note also the scale on the colorbar). We can further characterize the performance of the heat diode by investigating its points of maximal rectification. In this regard, it is useful to plot the quantities $\mathcal{R}_{max}(\tilde{\gamma}) = \max_q \mathcal{R}(\tilde{\gamma})$ and $\mathcal{R}_{min}(\tilde{\gamma}) = \min_q \mathcal{R}(\tilde{\gamma})$, which are shown in Fig. 7.2d with continuous and dashed lines for different T_L at fixed T_R. The maximal rectification, independently of its direction, is then given by

$$\chi_{max}(\tilde{\gamma}) = \max\{\ln \mathcal{R}_{max}(\tilde{\gamma}), -\ln \mathcal{R}_{min}(\tilde{\gamma})\}, \tag{7.12}$$

which is plotted as an highlighted curve in Fig. 2d. We observe that for the range of parameters corresponding to $\mathcal{R}_{min}$, the diode is always rectifying in the reverse thermal bias configuration ($\ln \mathcal{R}_{min} < 0$) and the magnitude of rectification is almost unaffected by $\tilde{\gamma}$. Differently, $\mathcal{R}_{max}$ increases in $\tilde{\gamma}$, starting from a small reverse rectification ($\ln \mathcal{R}_{max} < 0$) at low $\tilde{\gamma}$ up to a direct rectification ($\ln \mathcal{R}_{max} > 0$) at large $\tilde{\gamma}$. Interestingly, the turning points $\tilde{\gamma}_c$ associated with the switch of the rectification direction are followed by a remarkable enhancement of $\mathcal{R}$, as $\tilde{\gamma}$ is increased. To characterize the nature of the correlations giving rise to this evolution, we plot in Fig. 7.2e the amount of entanglement between the two qubits at steady state, as quantified by the entanglement of formation $\mathcal{E}(\rho)$. The latter is standardly defined as $\mathcal{E}(\rho) = -x \log_2(x) - (1 - x) \log_2(1 - x)$, where $x = (1 + \sqrt{1 - C^2})/2$ and $C(\rho)$ is the concurrence associated to the density matrix ρ [286]. Remarkably, the critical values $\tilde{\gamma}_c$ coincide with the values for which the entanglement between the qubits starts to appear, which in turn results to have $\mathcal{E} = 0.4$ at the higher rectification point shown in Fig. 7.2e (red line). Moreover, despite the reduction of the overall temperature gradient $T_L - T_R$, both χ_{max} and the amount of entanglement $\mathcal{E}$ similarly increases for low values of T_L as $\tilde{\gamma}$ increases. We also extended our simulation to higher values $\tilde{\gamma} > 0.2$ which leads to a saturation of χ_{max} with $\mathcal{E}$ keep increasing. For larger values of $\tilde{\gamma}$, $\ln \mathcal{R}$ tends to saturate while $\mathcal{E}$ keeps increasing. Such a high $\tilde{\gamma}$ regime is however less feasible with the use of tunable couplers which allow for an in-situ tuning of the coupling strength [274]. For the regime of parameters where χ_{max} is optimized, the quantum correlations of the system are strong enough to bring the qubits in an entangled state making it possible to envision applications also for quantum information purposes. Although the common features shared between rectification and entanglement veil a deeper connection between the two, an

[2] We have evaluated the increase up to 230% in the rectification in absence of an external flux $q = 0$ and regardless of its direction as $\frac{\max\{\mathcal{R}_{\tilde{\gamma}=0.15}, (1/\mathcal{R}_{\tilde{\gamma}=0.15})\}}{\max\{\mathcal{R}_{\tilde{\gamma}=0}, (1/\mathcal{R}_{\tilde{\gamma}=0})\}}$ and for experimentally feasible bath couplings $g_L = 0.75$ and $g_R = 0.25$

analytical one-to-one correspondence goes beyond the scope of our analysis [251], but might be of interest for further investigations.

7.4.1. DEPENDENCE ON THE BATHS COUPLING AND TEMPERATURE

In the following we characterize the performance of the heat diode depending on the temperatures $T_{L,R}$ and the coupling strengths $g_{L,R}$. In particular, Fig. 7.3a shows the dependence of $\ln \mathcal{R}$ on the left and right bath temperatures at the resonance point ($q = 0$, $\tilde{\gamma} = 0.15$). The rectification ratio is clearly symmetric with respect to the $T_L = T_R$ axis (blue line), in which no rectification is obviously observed. Higher values of $\mathcal{R}$ are obtained in the bottom-left angle of the colorplot, corresponding to lower values of baths temperatures as in agreement with the considerations previously done with regard to Fig. 7.2d. The red cut, corresponding to the condition of fixed left bath temperature T_L and variable right bath temperature T_R, is plotted in Fig. 7.2b. Notably, the condition $\ln \mathcal{R} = 0$, stemming for absence of rectification, is achieved not only in the absence of a temperature gradient ($T_L = T_R$), but also for another value of temperature bias. For this value, the asymmetry given by the bath temperatures compensates the asymmetric qubits-bath coupling resulting in a overall absence of preferential heat flow. This only holds when the qubits are interacting ($\tilde{\gamma} \neq 0$) as displayed by the behavior of $\mathcal{R}$ for $\tilde{\gamma} = \{0, 0.1\}$ with dashed grey lines. Figure 7.3c displays the full dependence of $\mathcal{R}$ on the qubit-bath coupling strengths $g_{L,R}$ at ($q = 0$, $\tilde{\gamma} = 0.15$). The blue line, corresponding to symmetric coupling $g_L = g_R$, highlights the need for a structural asymmetry between the qubits and baths in order to see any rectification effect [260, 285]. The behavior of $\mathcal{R}$ for fixed left bath coupling $g_L = 0.75$ is shown in Fig. 7.3c (red line). The rectification is remarkably sensitive to the coupling strengths when the system approaches the resonance condition at $\tilde{\gamma} = 0.15$. In this case, exceptional high values of rectification can be achieved with an enhancement up to $\sim 230\%$ for $g_R = 0.25$. As Fig. 7.3d shows, even higher rectification can be achieved at lower values of g_R. However they would correspond to values of thermal powers below $\sim$ fW which would not be detectable with current technology and are accordingly not experimentally relevant [233]. Such coupling strengths can be achieved with a proper design of the mutual inductances between qubits and thermal baths. For instance, by assuming a persistent current of $I_p = 50$ nA and a bath resistance $R_B = 1\Omega$, values of $g_B \sim 0.25 - 0.75$ can be easily achieved for $M_B = 50 - 150$ pH. In all our analysis, the bath thermalization times $1/\Gamma_{i\to j,B}$ are much longer than the system's typical timescale h/E_{ij} being $\Gamma_{i\to j,B}/(E_{ij}/h) \sim 10^{-4} - 10^{-1}$ validating the assumption of weak-coupling to the baths.

7.5. CONCLUSIONS

In conclusion, we have investigated the rectification properties of a system composed of two interacting flux qubits asymmetrically coupled to two RLC resonators acting as thermal baths. The system behaves as an efficient photonic heat diode in which rectification of heat currents between the two thermal environments takes place. We exploit quantum correlations between the two qubits to enhance the rectification factor, which would otherwise be constrained by the coupling to the baths and by their temperatures.

[2]For instance, thermal powers $\sim$ fW are expected for $\epsilon_0/h \sim 150$ GHz, $\Delta/h \sim 10$ GHz at ($\tilde{\gamma} = q = 0$) with $g_L = 0.75$ and $g_R = 0.25$

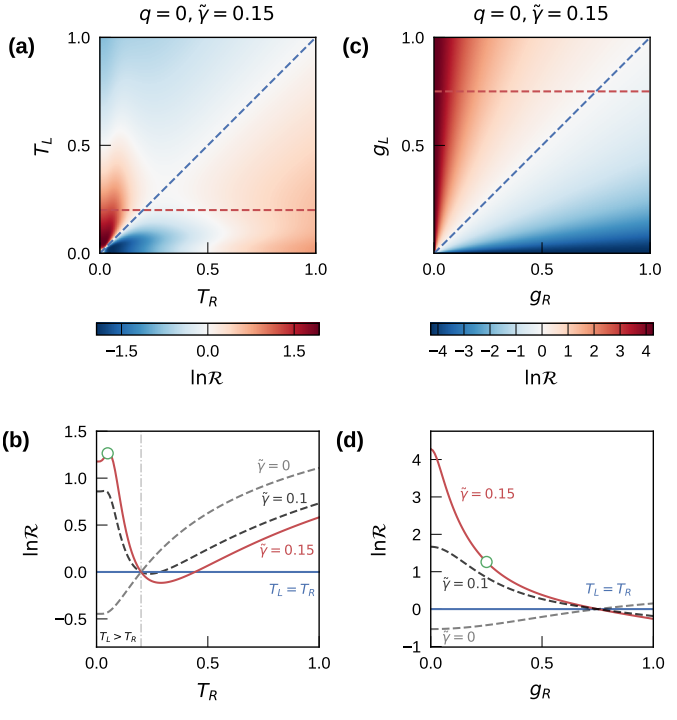

Figure 7.3: a) Dependence of the rectification ratio $\mathcal{R}$ on the left and right bath temperatures $T_{L,R}$ for $g_L = 0.75$ and $g_R = 0.25$. The blue cut corresponds to the axis $T_L = T_R$, while the red one corresponds to fixed left bath temperature $k_B T_L = \epsilon_0/5$. b) The two cuts showed in a) displays the variation of $\mathcal{R}$ as a function of the right temperature T_R. The green circle corresponds to the value $k_B T_R = \epsilon_0/20$ employed in Fig. 7.2. The dashed grey lines corresponds to lower values of interaction $\tilde{\gamma} = \{0, 0.1\}$ at $q = 0$. c) Dependence of $\mathcal{R}$ on the qubit-baths coupling strengths $g_{L,R}$. The blue line corresponds to the symmetric case of identical coupling $g_L = g_R$, while the red line to the condition of fixed $g_L = 0.75$. d) The two cuts displayed in c) showing the dependence of $\mathcal{R}$ on g_R. The green circle corresponds to the condition $g_R = 0.25$ presented in Fig. 7.2. The dashed grey lines corresponds to lower interaction values $\tilde{\gamma} = \{0, 0.1\}$ at $q = 0$. In all plots, $\epsilon_0 = 1$, $\Delta = 0.1, \hbar\omega_{LC} = 10\epsilon_0$, $Q_L = Q_R = 10$, $R_L = R_R = 1\ \Omega$ are employed.

Remarkably high values of rectification ratio up to $\mathcal{R} \sim 3.5$ can be obtained for realistic system parameters, with an enhancement up to $\sim 230\%$ compared to the non-interacting case. The system features the possibility of manipulating both the rectification amplitude and direction, effectively allowing to favor or suppress heat flow to a chosen bath. The directional manipulation of the heat flow in superconducting devices can be applied for efficient heat evacuation [265, 287] or for fast qubit initialisation [288]. Standard nanofabrication techniques can be employed for the experimental realization of similar devices [265, 274]. Our analysis can be easily adapted to other kinds of superconducting qubits, different coupling schemes or increased number of qubits.

8

Conclusions

In this thesis, we have presented four main topics that explore different aspects, both fundamental and applicative, of Josephson junctions based on semiconductor and fully metallic systems. In this chapter, we aim to summarize the main contributions of each work and discuss their implications and limitations. We also suggest possible future directions for further research.

In Chapter 4 we presented the first experimental realization of a Josephson phase battery, a device where the combined action of spin-splitting fields, spin-orbit coupling and superconducting correlation, is capable of generating an anomalous supercurrent. To do that, we realized an Aluminum-based SQUID interferometer with InAs nanowire Josephson junctions. We found that the ferromagnetic polarization of unpaired spin states on the nanowire surface can sustain the anomalous supercurrent even in the absence of external fields. The observed symmetries of the anomalous Josephson effect in the vectorial magnetic field are in agreement with theory. Future works could explore the design and implementation of more complex quantum circuits based on these hybrid elements, including a more desirable control over ferromagnetic coupling by exploit the integration of Al/EuS bilayer and InAs nanowires. Moreover, phase shifters could be employed as circuit elements, similarly to the realization of field-free flux qubits with π-junctions.

In Chapter 5, we investigated half-integer Shapiro steps in highly transmissive InSb nanoflag Josephson junctions. We used the versatile platform of free-standing defect-free InSb nanoflags to fabricate junctions with high transparency and critical currents. InSb is a semiconductor with high electron mobility, strong spin-orbit coupling, and large g-factor. We explored a regime of quantum transport with parallel short and long conducting channels, which may indicate the possible presence of an accumulation layer at the InSb edge(s). Under microwave irradiation, we observed robust half-integer Shapiro steps. Our analysis of temperature and device parameters led us to conclude that the half-integer steps have a non-equilibrium origin, meaning that the non-trivial occupation of the Andreev bound states is realizing an effective $\sin(2\varphi)$ CPR. However, a comprehensive theoretical model accounting for all observed features and explaining

the role of different parameters is lacking. Future research could focus on developing more comprehensive theories, which can be applied to ballistic junctions. Overall, our results demonstrate the potential of ballistic InSb nanoflags Josephson junctions for manipulating Andreev bound states and their dynamics.

In Chapter 6, we investigated the debated gating effect in metallic superconducting Dayem bridges. We provided a historical analysis and development of gating effects in superconducting nanowires. We measured gated superconducting constrictions made of different materials and geometries integrated in microwave resonators, and realized fully metallic gate-tunable resonators whose modulation could be explained by gate leakage current. We observed signatures of non-local gating phenomena, indicating that the leakage is inducing high-energy phonons that can extend across the entire chip. Additionally, we presented a comprehensive review and meta-analysis of gated superconducting wires measured in DC, attempting to elucidate the geometry and material factors that dominate the gating phenomenon in solid-state platforms. Improvements could be made in developing optimal strategies for integrating the gate tuning effects for their potential applications in superconducting quantum devices, for instance, to realize high frequency superconducting switches, frequency-tunable resonators and couplers, and gate-controlled parametric amplifiers while minimizing power dissipation or limiting unwanted cross-talk caused by phonon excitations. This would require optimization of substrates, material choice, and nanowire geometry.

In Chapter 7, we theoretically explored potential applications of superconducting circuits in the context of thermal transport. We focused on the prototypical example of a quantum heat diode based on two interacting flux qubits coupled to two photonic heat baths and studied thermal rectification. We found that the coherent interaction between the qubits could be exploited to enhance the rectification factor, which would otherwise be constrained by the baths' temperatures and couplings. A significant increase in the rectification can be observed for the regime in which a non-vanishing entanglement appears between the qubits, potentially revealing a deeper connection between them. To further advance our understanding of quantum thermal transport, future research could investigate the interplay between quantum correlations and thermal properties. Such investigations could contribute to ongoing experimental efforts aimed at realizing these circuits, including heat valves, engines, and refrigerators.

References

[1] Michael Tinkham. *Introduction to Superconductivity*. Courier Corporation, January 2004. ISBN 978-0-486-13472-7.

[2] A. A. Golubov, M. Yu. Kupriyanov, and E. Il'ichev. The current-phase relation in Josephson junctions. *Reviews of Modern Physics*, 76(2):411–469, April 2004. doi: 10.1103/RevModPhys.76.411.

[3] B. D. Josephson. Possible new effects in superconductive tunnelling. *Physics Letters*, 1(7):251–253, July 1962. ISSN 0031-9163. doi: 10.1016/0031-9163(62)91369-0.

[4] A. F. Andreev. The thermal conductivity of the intermediate state in superconductors. *Zhurnal Eksperimental'noj I Teoreticheskoj Fiziki*, 46(5), 1964. ISSN 0044-4510.

[5] C. W. J. Beenakker. Universal limit of critical-current fluctuations in mesoscopic Josephson junctions. *Physical Review Letters*, 67(27):3836–3839, December 1991. ISSN 0031-9007. doi: 10.1103/PhysRevLett.67.3836.

[6] Chikara Ishii. Josephson Currents through Junctions with Normal Metal Barriers. *Progress of Theoretical Physics*, 44(6):1525–1547, December 1970. ISSN 0033-068X. doi: 10.1143/PTP.44.1525.

[7] T.M. Klapwijk, G.E. Blonder, and M. Tinkham. Explanation of subharmonic energy gap structure in superconducting contacts. *Physica B+C*, 109–110:1657–1664, July 1982. ISSN 03784363. doi: 10.1016/0378-4363(82)90189-9.

[8] F. Zhou, P. Charlat, B. Spivak, and B. Pannetier. Density of States in Superconductor-Normal Metal-Superconductor Junctions. *Journal of Low Temperature Physics*, 110(3):841–850, February 1998. ISSN 1573-7357. doi: 10.1023/A:1022628927203.

[9] Wolfgang Belzig, Frank K Wilhelm, Christoph Bruder, Gerd Schön, and Andrei D Zaikin. Quasiclassical Green's function approach to mesoscopic superconductivity. *Superlattices and Microstructures*, 25(5):1251–1288, May 1999. ISSN 0749-6036. doi: 10.1006/spmi.1999.0710.

[10] Tero T. Heikkilä, Jani Särkkä, and Frank K. Wilhelm. Supercurrent-carrying density of states in diffusive mesoscopic Josephson weak links. *Physical Review B*, 66 (18):184513, November 2002. doi: 10.1103/PhysRevB.66.184513.

[11] P. Dubos, H. Courtois, B. Pannetier, F. K. Wilhelm, A. D. Zaikin, and G. Schön. Josephson critical current in a long mesoscopic S-N-S junction. *Physical Review B*, 63(6):064502, January 2001. doi: 10.1103/PhysRevB.63.064502.

[12] Pauli Virtanen. Usadel1, March 2006.

[13] Pauli Virtanen. Usadelnd, May 2022.

[14] P E Lindelof. Superconducting microbridges exhibiting Josephson properties. *Reports on Progress in Physics*, 44(9):949–1026, September 1981. ISSN 0034-4885, 1361-6633. doi: 10.1088/0034-4885/44/9/001.

[15] K. K. Likharev. Superconducting weak links. *Reviews of Modern Physics*, 51(1): 101–159, January 1979. ISSN 0034-6861. doi: 10.1103/RevModPhys.51.101.

[16] P. Virtanen, A. Ronzani, and F. Giazotto. Spectral characteristics of a fully-superconducting SQUIPT. *Physical Review Applied*, 6(5), November 2016. ISSN 2331-7019. doi: 10.1103/PhysRevApplied.6.054002.

[17] John Clarke and Alex I. Braginski. *The SQUID Handbook: Applications of SQUIDs and SQUID Systems*. John Wiley & Sons, December 2006. ISBN 978-3-527-60950-5.

[18] H. Courtois, M. Meschke, J. T. Peltonen, and J. P. Pekola. Origin of Hysteresis in a Proximity Josephson Junction. *Physical Review Letters*, 101(6):067002, August 2008. doi: 10.1103/PhysRevLett.101.067002.

[19] Michel H. Devoret, John M. Martinis, and John Clarke. Measurements of Macroscopic Quantum Tunneling out of the Zero-Voltage State of a Current-Biased Josephson Junction. *Physical Review Letters*, 55(18):1908–1911, October 1985. doi: 10.1103/PhysRevLett.55.1908.

[20] M. H. Devoret. Quantum Fluctuations in Electrical Circuits. page 351, 1997.

[21] Likharev. *Dynamics of Josephson Junctions and Circuits*. CRC Press, August 1986. ISBN 978-2-88124-042-3.

[22] Athanassios Bardas and Dmitri V. Averin. Electron transport in mesoscopic disordered superconductor–normal-metal–superconductor junctions. *Physical Review B*, 56(14):R8518–R8521, October 1997. doi: 10.1103/PhysRevB.56.R8518.

[23] Pauli Virtanen, Tero T. Heikkilä, F. Sebastián Bergeret, and Juan Carlos Cuevas. Theory of Microwave-Assisted Supercurrent in Diffusive SNS Junctions. *Physical Review Letters*, 104(24):247003, June 2010. ISSN 0031-9007, 1079-7114. doi: 10.1103/PhysRevLett.104.247003.

[24] F. S. Bergeret, P. Virtanen, A. Ozaeta, T. T. Heikkilä, and J. C. Cuevas. Supercurrent and Andreev bound state dynamics in superconducting quantum point contacts under microwave irradiation. *Physical Review B*, 84(5):054504, August 2011. ISSN 1098-0121, 1550-235X. doi: 10.1103/PhysRevB.84.054504.

[25] T.M. Klapwijk and P.J. de Visser. The discovery, disappearance and re-emergence of radiation-stimulated superconductivity. *Annals of Physics*, 417:168104, June 2020. ISSN 00034916. doi: 10.1016/j.aop.2020.168104.

[26] Sidney Shapiro. Josephson Currents in Superconducting Tunneling: The Effect of Microwaves and Other Observations. *Physical Review Letters*, 11(2):80–82, July 1963. ISSN 0031-9007. doi: 10.1103/PhysRevLett.11.80.

[27] Clark A. Hamilton. Josephson voltage standards. *Review of Scientific Instruments*, 71(10):3611–3623, October 2000. ISSN 0034-6748. doi: 10.1063/1.1289507.

[28] P. Russer. Influence of Microwave Radiation on Current-Voltage Characteristic of Superconducting Weak Links. *Journal of Applied Physics*, 43(4):2008–2010, April 1972. ISSN 0021-8979, 1089-7550. doi: 10.1063/1.1661440.

[29] R. L. Kautz. The ac Josephson effect in hysteretic junctions: Range and stability of phase lock. *Journal of Applied Physics*, 52(5):3528–3541, May 1981. ISSN 0021-8979, 1089-7550. doi: 10.1063/1.329132.

[30] P. Joyez, P. Lafarge, A. Filipe, D. Esteve, and M. H. Devoret. Observation of parity-induced suppression of Josephson tunneling in the superconducting single electron transistor. *Physical Review Letters*, 72(15):2458–2461, April 1994. ISSN 0031-9007. doi: 10.1103/PhysRevLett.72.2458.

[31] Pablo Jarillo-Herrero, Jorden A. van Dam, and Leo P. Kouwenhoven. Quantum supercurrent transistors in carbon nanotubes. *Nature*, 439(7079):953–956, February

2006. ISSN 1476-4687. doi: 10.1038/nature04550.

[32] T. W. Larsen, K. D. Petersson, F. Kuemmeth, T. S. Jespersen, P. Krogstrup, J. Nygård, and C. M. Marcus. Semiconductor-Nanowire-Based Superconducting Qubit. *Physical Review Letters*, 115(12):127001, September 2015. doi: 10.1103/PhysRevLett.115.127001.

[33] M. Fuechsle, J. Bentner, D. A. Ryndyk, M. Reinwald, W. Wegscheider, and C. Strunk. Effect of Microwaves on the Current-Phase Relation of Superconductor–Normal-Metal–Superconductor Josephson Junctions. *Physical Review Letters*, 102(12):127001, March 2009. ISSN 0031-9007, 1079-7114. doi: 10.1103/PhysRevLett.102.127001.

[34] Ziwei Dou, Taro Wakamura, Pauli Virtanen, Nian-Jheng Wu, Richard Deblock, Sandrine Autier-Laurent, Kenji Watanabe, Takashi Taniguchi, Sophie Guéron, Hélène Bouchiat, and Meydi Ferrier. Microwave photoassisted dissipation and supercurrent of a phase-biased graphene-superconductor ring. *Physical Review Research*, 3(3):L032009, July 2021. ISSN 2643-1564. doi: 10.1103/PhysRevResearch.3.L032009.

[35] J. C. Cuevas, J. Heurich, A. Martín-Rodero, A. Levy Yeyati, and G. Schön. Subharmonic Shapiro Steps and Assisted Tunneling in Superconducting Point Contacts. *Physical Review Letters*, 88(15):157001, March 2002. ISSN 0031-9007, 1079-7114. doi: 10.1103/PhysRevLett.88.157001.

[36] A. F. G. Wyatt, V. M. Dmitriev, W. S. Moore, and F. W. Sheard. Microwave-Enhanced Critical Supercurrents in Constricted Tin Films. *Physical Review Letters*, 16(25):1166–1169, June 1966. doi: 10.1103/PhysRevLett.16.1166.

[37] F. S. Bergeret and I. V. Tokatly. Theory of diffusive Φ0 Josephson junctions in the presence of spin-orbit coupling. *Europhysics Letters*, 110(5):57005, June 2015. ISSN 0295-5075. doi: 10.1209/0295-5075/110/57005.

[38] F. S. Bergeret, A. F. Volkov, and K. B. Efetov. Odd triplet superconductivity and related phenomena in superconductor-ferromagnet structures. *Reviews of Modern Physics*, 77(4):1321–1373, November 2005. doi: 10.1103/RevModPhys.77.1321.

[39] A. I. Buzdin. Proximity effects in superconductor-ferromagnet heterostructures. *Reviews of Modern Physics*, 77(3):935–976, September 2005. doi: 10.1103/RevModPhys.77.935.

[40] Jacob Linder and Jason W. A. Robinson. Superconducting spintronics. *Nature Physics*, 11(4):307–315, April 2015. ISSN 1745-2481. doi: 10.1038/nphys3242.

[41] W. Guichard, M. Aprili, O. Bourgeois, T. Kontos, J. Lesueur, and P. Gandit. Phase Sensitive Experiments in Ferromagnetic-Based Josephson Junctions. *Physical Review Letters*, 90(16):167001, April 2003. doi: 10.1103/PhysRevLett.90.167001.

[42] A. Bauer, J. Bentner, M. Aprili, M. L. Della Rocca, M. Reinwald, W. Wegscheider, and C. Strunk. Spontaneous Supercurrent Induced by Ferromagnetic $\ensuremath{\pi}$ Junctions. *Physical Review Letters*, 92(21):217001, May 2004. doi: 10.1103/PhysRevLett.92.217001.

[43] V. V. Ryazanov, V. A. Oboznov, A. Yu. Rusanov, A. V. Veretennikov, A. A. Golubov, and J. Aarts. Coupling of Two Superconductors through a Ferromagnet: Evidence for a $\ensuremath{\pi}$ Junction. *Physical Review Letters*, 86(11):2427–2430, March 2001. doi: 10.1103/PhysRevLett.86.2427.

[44] Peter Fulde and Richard A. Ferrell. Superconductivity in a Strong Spin-Exchange

Field. *Physical Review*, 135(3A):A550–A563, August 1964. doi: 10.1103/PhysRev.135.A550.

[45] A. I. Larkin and Yu N. Ovchinnikov. NONUNIFORM STATE OF SUPERCONDUCTORS. *Zh. Eksperim. i Teor. Fiz.*, Vol: 47, September 1964.

[46] Chung Ting Ke, Christian M. Moehle, Folkert K. de Vries, Candice Thomas, Sara Metti, Charles R. Guinn, Ray Kallaher, Mario Lodari, Giordano Scappucci, Tiantian Wang, Rosa E. Diaz, Geoffrey C. Gardner, Michael J. Manfra, and Srijit Goswami. Ballistic superconductivity and tunable π–junctions in InSb quantum wells. *Nature Communications*, 10(1):3764, August 2019. ISSN 2041-1723. doi: 10.1038/s41467-019-11742-4.

[47] D. Razmadze, R. Seoane Souto, L. Galletti, A. Maiani, Y. Liu, P. Krogstrup, C. Schrade, A. Gyenis, C. M. Marcus, and S. Vaitiekėnas. Supercurrent reversal in ferromagnetic hybrid nanowire Josephson junctions. *Physical Review B*, 107(8): L081301, February 2023. doi: 10.1103/PhysRevB.107.L081301.

[48] Yu. A. Bychkov and É. I. Rashba. Properties of a 2D electron gas with lifted spectral degeneracy. *Soviet Journal of Experimental and Theoretical Physics Letters*, 39:78, January 1984. ISSN 0021-3640.

[49] Andrea Iorio, Mirko Rocci, Lennart Bours, Matteo Carrega, Valentina Zannier, Lucia Sorba, Stefano Roddaro, Francesco Giazotto, and Elia Strambini. Vectorial control of the spin-orbit interaction in suspended InAs nanowires. *Nano Letters*, November 2018. ISSN 1530-6984, 1530-6992. doi: 10.1021/acs.nanolett.8b02828.

[50] Manuel Houzet and Julia S. Meyer. Quasiclassical theory of disordered Rashba superconductors. *Physical Review B*, 92(1):014509, July 2015. doi: 10.1103/PhysRevB.92.014509.

[51] Tomohiro Yokoyama, Mikio Eto, and Yuli V. Nazarov. Anomalous Josephson effect induced by spin-orbit interaction and Zeeman effect in semiconductor nanowires. *Phys. Rev. B*, 89(19):195407, 2014. doi: 10.1103/PhysRevB.89.195407. URL http://link.aps.org/doi/10.1103/PhysRevB.89.195407.

[52] Victor M. Edelstein. The Ginzburg - Landau equation for superconductors of polar symmetry. *Journal of Physics: Condensed Matter*, 8(3):339, January 1996. ISSN 0953-8984. doi: 10.1088/0953-8984/8/3/012.

[53] A. Buzdin. Direct Coupling Between Magnetism and Superconducting Current in the Josephson φ 0 Junction. *Physical Review Letters*, 101(10):107005, September 2008. ISSN 0031-9007, 1079-7114. doi: 10.1103/PhysRevLett.101.107005.

[54] François Konschelle, Ilya V. Tokatly, and F. Sebastián Bergeret. Theory of the spin-galvanic effect and the anomalous phase shift ${\ensuremath{\varphi}}_{0}$ in superconductors and Josephson junctions with intrinsic spin-orbit coupling. *Physical Review B*, 92(12):125443, September 2015. doi: 10.1103/PhysRevB.92.125443.

[55] M. I. Dyakonov and V. I. Perel. Current-induced spin orientation of electrons in semiconductors. *Physics Letters A*, 35(6):459–460, July 1971. ISSN 0375-9601. doi: 10.1016/0375-9601(71)90196-4.

[56] V. M. Edelstein. Spin polarization of conduction electrons induced by electric current in two-dimensional asymmetric electron systems. *Solid State Communications*, 73(3):233–235, January 1990. ISSN 0038-1098. doi: 10.1016/0038-1098(90)90963-C.

[57] Victor M. Edelstein. Magnetoelectric Effect in Polar Superconductors. *Physical*

Review Letters, 75(10):2004–2007, September 1995. doi: 10.1103/PhysRevLett.75.2004.

[58] Antonio Barone and Gianfranco Paterno. *Physics and Applications of the Josephson Effect*. Wiley, May 1982. ISBN 978-0-471-01469-0.

[59] J. C. Cuevas and F. S. Bergeret. Magnetic Interference Patterns and Vortices in Diffusive SNS Junctions. *Physical Review Letters*, 99(21):217002, November 2007. doi: 10.1103/PhysRevLett.99.217002.

[60] F. Chiodi, M. Ferrier, S. Guéron, J. C. Cuevas, G. Montambaux, F. Fortuna, A. Kasumov, and H. Bouchiat. Geometry-related magnetic interference patterns in long SNS Josephson junctions. *Physical Review B*, 86(6):064510, August 2012. ISSN 1098-0121, 1550-235X. doi: 10.1103/PhysRevB.86.064510.

[61] L. Angers, F. Chiodi, G. Montambaux, M. Ferrier, S. Guéron, H. Bouchiat, and J. C. Cuevas. Proximity dc squids in the long-junction limit. *Physical Review B*, 77(16):165408, April 2008. ISSN 1098-0121, 1550-235X. doi: 10.1103/PhysRevB.77.165408.

[62] Jonas Zmuidzinas. Superconducting Microresonators: Physics and Applications. *Annual Review of Condensed Matter Physics*, 3(1):169–214, 2012. doi: 10.1146/annurev-conmatphys-020911-125022.

[63] Alexandre Blais, Arne L. Grimsmo, S. M. Girvin, and Andreas Wallraff. Circuit quantum electrodynamics. *Reviews of Modern Physics*, 93(2):025005, May 2021. doi: 10.1103/RevModPhys.93.025005.

[64] Benjamin A. Mazin. *Microwave Kinetic Inductance Detectors*. PhD thesis, California Institute of Technology, 2005.

[65] Frank Pobell. *Matter and Methods at Low Temperatures*. Springer, Berlin, Heidelberg, 1996. ISBN 978-3-540-58572-5 978-3-662-03225-1. doi: 10.1007/978-3-662-03225-1.

[66] S. Krinner, S. Storz, P. Kurpiers, P. Magnard, J. Heinsoo, R. Keller, J. Lütolf, C. Eichler, and A. Wallraff. Engineering cryogenic setups for 100-qubit scale superconducting circuit systems. *EPJ Quantum Technology*, 6(1):1–29, December 2019. ISSN 2196-0763. doi: 10.1140/epjqt/s40507-019-0072-0.

[67] Kurtis Lee Geerlings. *Improving Coherence of Superconducting Qubits and Resonators*. Yale University, 2013.

[68] QCoDeS/Qcodes. QCoDeS, June 2023.

[69] Subhajit Pal and Colin Benjamin. Quantized Josephson phase battery. *EPL*, 126(5):57002, July 2019. ISSN 0295-5075. doi: 10.1209/0295-5075/126/57002. URL https://iopscience.iop.org/article/10.1209/0295-5075/126/57002/meta.

[70] A. Yacoby, R. Schuster, and M. Heiblum. Phase rigidity and h/2e oscillations in a single-ring Aharonov-Bohm experiment. *Phys. Rev. B*, 53(15):9583–9586, April 1996. doi: 10.1103/PhysRevB.53.9583. URL http://link.aps.org/doi/10.1103/PhysRevB.53.9583.

[71] E. Strambini, V. Piazza, G. Biasiol, L. Sorba, and F. Beltram. Impact of classical forces and decoherence in multiterminal Aharonov-Bohm networks. *Phys. Rev. B*, 79(19):195443, 2009. doi: 10.1103/PhysRevB.79.195443. URL http://link.aps.org/doi/10.1103/PhysRevB.79.195443.

[72] V. V. Ryazanov, V. A. Oboznov, A. Yu. Rusanov, A. V. Veretennikov, A. A. Golubov, and J. Aarts. Coupling of Two Superconductors through a Ferromag-

net: Evidence for a π Junction. *Phys. Rev. Lett.*, 86(11):2427–2430, March 2001. doi: 10.1103/PhysRevLett.86.2427. URL http://link.aps.org/doi/10.1103/PhysRevLett.86.2427.

[73] A. A. Golubov, M. Yu. Kupriyanov, and E. Il'ichev. The current-phase relation in Josephson junctions. *Rev. Mod. Phys.*, 76(2):411–469, April 2004. doi: 10.1103/RevModPhys.76.411. URL http://link.aps.org/doi/10.1103/RevModPhys.76.411.

[74] Burm Baek, William H. Rippard, Samuel P. Benz, Stephen E. Russek, and Paul D. Dresselhaus. Hybrid superconducting-magnetic memory device using competing order parameters. *Nature Communications*, 5:3888, May 2014. ISSN 2041-1723. doi: 10.1038/ncomms4888. URL http://www.nature.com/ncomms/2014/140528/ncomms4888/full/ncomms4888.html.

[75] E. C. Gingrich, Bethany M. Niedzielski, Joseph A. Glick, Yixing Wang, D. L. Miller, Reza Loloee, W. P. Pratt Jr, and Norman O. Birge. Controllable 0-π Josephson junctions containing a ferromagnetic spin valve. *Nat Phys*, 12(6):564–567, June 2016. ISSN 1745-2473. doi: 10.1038/nphys3681. URL http://www.nature.com/nphys/journal/v12/n6/full/nphys3681.html.

[76] MA Silaev, IV Tokatly, and FS Bergeret. Anomalous current in diffusive ferromagnetic josephson junctions. *Physical Review B*, 95(18):184508, 2017.

[77] T. Yokoyama and Yu V. Nazarov. Magnetic anisotropy of critical current in nanowire Josephson junction with spin-orbit interaction. *EPL*, 108(4):47009, November 2014. ISSN 0295-5075. doi: 10.1209/0295-5075/108/47009. URL https://doi.org/10.1209%2F0295-5075%2F108%2F47009.

[78] D. B. Szombati, S. Nadj-Perge, D. Car, S. R. Plissard, E. P. a. M. Bakkers, and L. P. Kouwenhoven. Josephson Φ0-junction in nanowire quantum dots. *Nature Physics*, 12(6):568–572, June 2016. ISSN 1745-2481. doi: 10.1038/nphys3742.

[79] Alexandre Assouline, Cheryl Feuillet-Palma, Nicolas Bergeal, Tianzhen Zhang, Alireza Mottaghizadeh, Alexandre Zimmers, Emmanuel Lhuillier, Mahmoud Eddrief, Paola Atkinson, Marco Aprili, and Herve Aubin. Spin-Orbit induced phase-shift in Bi$_{2}$Se$_{3}$ Josephson junctions. *Nature Communications*, 10(1):126, December 2019. ISSN 2041-1723. doi: 10.1038/s41467-018-08022-y.

[80] William Mayer, Matthieu C. Dartiailh, Joseph Yuan, Kaushini S. Wickramasinghe, Enrico Rossi, and Javad Shabani. Gate controlled anomalous phase shift in Al/InAs Josephson junctions. *Nat Commun*, 11(1):1–6, January 2020. ISSN 2041-1723. doi: 10.1038/s41467-019-14094-1. URL https://www.nature.com/articles/s41467-019-14094-1.

[81] Jacob Linder and Jason W. A. Robinson. Superconducting spintronics. *Nat Phys*, 11(4):307–315, April 2015. ISSN 1745-2473. doi: 10.1038/nphys3242. URL http://www.nature.com/nphys/journal/v11/n4/abs/nphys3242.html.

[82] Francesco Giazotto, Panayotis Spathis, Stefano Roddaro, Subhajit Biswas, Fabio Taddei, Michele Governale, and Lucia Sorba. A Josephson quantum electron pump. *Nat. Phys.*, 7(11):857–861, November 2011. ISSN 1745-2473. doi: 10.1038/nphys2053. URL http://www.nature.com/nphys/journal/v7/n11/full/nphys2053.html.

[83] J. Clarke and A. I. Braginski, editors. *The SQUID handbook*. Wiley-VCH, Weinheim,

2004. ISBN 978-3-527-40411-7 978-3-527-40408-7 978-3-527-40229-8.

[84] Keshab R. Sapkota, F. Scott Maloney, and Wenyong Wang. Observations of the Kondo effect and its coexistence with ferromagnetism in a magnetically undoped metal oxide nanostructure. *Phys. Rev. B*, 97(14):144425, April 2018. doi: 10.1103/PhysRevB.97.144425. URL https://link.aps.org/doi/10.1103/PhysRevB.97.144425.

[85] Tomasz Dietl and Hideo Ohno. Engineering magnetism in semiconductors. *Materials Today*, 9(11):18–26, November 2006. ISSN 1369-7021. doi: 10.1016/S1369-7021(06)71691-1. URL http://www.sciencedirect.com/science/article/pii/S1369702106716911.

[86] T. Golod, A. Rydh, and V. M. Krasnov. Detection of the phase shift from a single abrikosov vortex. *Phys. Rev. Lett.*, 104:227003, Jun 2010. doi: 10.1103/PhysRevLett.104.227003. URL https://link.aps.org/doi/10.1103/PhysRevLett.104.227003.

[87] Marta Pita-Vidal, Arno Bargerbos, Chung-Kai Yang, David J. van Woerkom, Wolfgang Pfaff, Nadia Haider, Peter Krogstrup, Leo P. Kouwenhoven, Gijs de Lange, and Angela Kou. A gate-tunable, field-compatible fluxonium. *arXiv:1910.07978 [cond-mat, physics:quant-ph]*, October 2019. URL http://arxiv.org/abs/1910.07978.

[88] T.W. Larsen, K.D. Petersson, F. Kuemmeth, T.S. Jespersen, P. Krogstrup, J. Nygård, and C.M. Marcus. Semiconductor-Nanowire-Based Superconducting Qubit. *Phys. Rev. Lett.*, 115(12):127001, September 2015. doi: 10.1103/PhysRevLett.115.127001. URL http://link.aps.org/doi/10.1103/PhysRevLett.115.127001.

[89] C. Guarcello and F.S. Bergeret. Cryogenic Memory Element Based on an Anomalous Josephson Junction. *Phys. Rev. Applied*, 13(3):034012, March 2020. doi: 10.1103/PhysRevApplied.13.034012. URL https://link.aps.org/doi/10.1103/PhysRevApplied.13.034012.

[90] Andres A. Reynoso, Gonzalo Usaj, C. A. Balseiro, D. Feinberg, and M. Avignon. Spin-orbit-induced chirality of Andreev states in Josephson junctions. *Phys. Rev. B*, 86(21):214519, December 2012. doi: 10.1103/PhysRevB.86.214519. URL https://link.aps.org/doi/10.1103/PhysRevB.86.214519.

[91] P. Virtanen, F. S. Bergeret, E. Strambini, F. Giazotto, and A. Braggio. Majorana bound states in hybrid two-dimensional Josephson junctions with ferromagnetic insulators. *Phys. Rev. B*, 98(2):020501, July 2018. doi: 10.1103/PhysRevB.98.020501. URL https://link.aps.org/doi/10.1103/PhysRevB.98.020501.

[92] J. Tiira, E. Strambini, M. Amado, S. Roddaro, P. San-Jose, R. Aguado, F. S. Bergeret, D. Ercolani, L. Sorba, and F. Giazotto. Magnetically-driven colossal supercurrent enhancement in InAs nanowire Josephson junctions. *Nature Communications*, 8:14984, April 2017. ISSN 2041-1723. doi: 10.1038/ncomms14984. URL http://www.nature.com/ncomms/2017/170412/ncomms14984/full/ncomms14984.html.

[93] Faustino Martelli, Silvia Rubini, Matteo Piccin, Giorgio Bais, Fauzia Jabeen, Silvano De Franceschi, Vincenzo Grillo, Elvio Carlino, Francesco D'Acapito, Federico Boscherini, Stefano Cabrini, Marco Lazzarino, Luca Businaro, Filippo Romanato,

and Alfonso Franciosi. Manganese-Induced Growth of GaAs Nanowires. *Nano Lett.*, 6(9):2130–2134, September 2006. ISSN 1530-6984. doi: 10.1021/nl0607838. URL https://doi.org/10.1021/nl0607838.

[94] E. Strambini, V. N. Golovach, G. De Simoni, J. S. Moodera, F. S. Bergeret, and F. Giazotto. Revealing the magnetic proximity effect in EuS/Al bilayers through superconducting tunneling spectroscopy. *Phys. Rev. Materials*, 1(5):054402, October 2017. doi: 10.1103/PhysRevMaterials.1.054402. URL https://link.aps.org/doi/10.1103/PhysRevMaterials.1.054402.

[95] Yu Liu, Saulius Vaitiekėnas, Sara Martí-Sánchez, Christian Koch, Sean Hart, Zheng Cui, Thomas Kanne, Sabbir A. Khan, Rawa Tanta, Shivendra Upadhyay, Martin Espiñeira Cachaza, Charles M. Marcus, Jordi Arbiol, Kathryn A. Moler, and Peter Krogstrup. Semiconductor–Ferromagnetic Insulator–Superconductor Nanowires: Stray Field and Exchange Field. *Nano Lett.*, 20(1):456–462, January 2020. ISSN 1530-6984. doi: 10.1021/acs.nanolett.9b04187. URL https://doi.org/10.1021/acs.nanolett.9b04187.

[96] U. P. Gomes, D. Ercolani, V. Zannier, F. Beltram, and L. Sorba. Controlling the diameter distribution and density of InAs nanowires grown by Au-assisted methods. *Semicond. Sci. Technol.*, 30(11):115012, 2015. ISSN 0268-1242. doi: 10.1088/0268-1242/30/11/115012. URL http://stacks.iop.org/0268-1242/30/i=11/a=115012.

[97] Jesper Wallentin and Magnus T. Borgström. Doping of semiconductor nanowires. *Journal of Materials Research*, 26(17):2142–2156, September 2011. ISSN 2044-5326, 0884-2914. doi: 10.1557/jmr.2011.214. URL https://www.cambridge.org/core/journals/journal-of-materials-research/article/doping-of-semiconductor-nanowires/3EE82D42A6D504B4B427CB979CC3B8D0.

[98] A. Iorio, M. Rocci, L. Bours, M. Carrega, V. Zannier, L. Sorba, S. Roddaro, F. Giazotto, and E. Strambini. Vectorial Control of the Spin–Orbit Interaction in Suspended InAs Nanowires. *Nano Lett.*, 19(2):652–657, February 2019. ISSN 1530-6984. doi: 10.1021/acs.nanolett.8b02828. URL https://doi.org/10.1021/acs.nanolett.8b02828.

[99] A. Rogachev, T.-C. Wei, D. Pekker, A. T. Bollinger, P. M. Goldbart, and A. Bezryadin. Magnetic-Field Enhancement of Superconductivity in Ultranarrow Wires. *Physical Review Letters*, 97(13):137001, September 2006. doi: 10.1103/PhysRevLett.97.137001. URL https://link.aps.org/doi/10.1103/PhysRevLett.97.137001.

[100] Jun Kondo. Resistance Minimum in Dilute Magnetic Alloys. *Prog. Theor. Phys.*, 32(1):37–49, 1964. doi: 10.1143/PTP.32.37. URL http://ptp.ipap.jp/link?PTP/32/37/.

[101] Aveek Bid, Achyut Bora, and A. K. Raychaudhuri. Temperature dependence of the resistance of metallic nanowires of diameter $\geqslant 15$ nm: Applicability of bloch-grüneisen theorem. *Phys. Rev. B*, 74:035426, Jul 2006. doi: 10.1103/PhysRevB.74.035426. URL https://link.aps.org/doi/10.1103/PhysRevB.74.035426.

[102] D. Goldhaber-Gordon, J. Göres, M. A. Kastner, Hadas Shtrikman, D. Mahalu, and U. Meirav. From the Kondo Regime to the Mixed-Valence Regime in a Single-

Electron Transistor. *Phys. Rev. Lett.*, 81(23):5225–5228, December 1998. doi: 10.1103/PhysRevLett.81.5225. URL https://link.aps.org/doi/10.1103/PhysRevLett.81.5225.

[103] J. J. Parks, A. R. Champagne, T. A. Costi, W. W. Shum, A. N. Pasupathy, E. Neuscamman, S. Flores-Torres, P. S. Cornaglia, A. A. Aligia, C. A. Balseiro, G. K.-L. Chan, H. D. Abruña, and D. C. Ralph. Mechanical control of spin states in spin-1 molecules and the underscreened kondo effect. *Science*, 328(5984): 1370–1373, 2010. ISSN 0036-8075. doi: 10.1126/science.1186874. URL https://science.sciencemag.org/content/328/5984/1370.

[104] F. Mallet, J. Ericsson, D. Mailly, S. Ünlübayir, D. Reuter, A. Melnikov, A. D. Wieck, T. Micklitz, A. Rosch, T. A. Costi, L. Saminadayar, and C. Bäuerle. Scaling of the Low-Temperature Dephasing Rate in Kondo Systems. *Phys. Rev. Lett.*, 97(22): 226804, November 2006. doi: 10.1103/PhysRevLett.97.226804. URL https://link.aps.org/doi/10.1103/PhysRevLett.97.226804.

[105] T. A. Costi, L. Bergqvist, A. Weichselbaum, J. von Delft, T. Micklitz, A. Rosch, P. Mavropoulos, P. H. Dederichs, F. Mallet, L. Saminadayar, and C. Bäuerle. Kondo Decoherence: Finding the Right Spin Model for Iron Impurities in Gold and Silver. *Phys. Rev. Lett.*, 102(5):056802, February 2009. doi: 10.1103/PhysRevLett.102.056802. URL https://link.aps.org/doi/10.1103/PhysRevLett.102.056802.

[106] D. R. Hamann. New Solution for Exchange Scattering in Dilute Alloys. *Phys. Rev.*, 158(3):570–580, June 1967. doi: 10.1103/PhysRev.158.570. URL https://link.aps.org/doi/10.1103/PhysRev.158.570.

[107] FranÃ§ois Konschelle, Ilya V. Tokatly, and F. Sebastian Bergeret. Theory of the spin-galvanic effect and the anomalous phase shift φ_0 in superconductors and Josephson junctions with intrinsic spin-orbit coupling. *Phys. Rev. B*, 92(125443): 125443, 2015. doi: 10.1103/PhysRevB.92.125443.

[108] Sophie D'Ambrosio, Martin Meissner, Christophe Blanc, Alberto Ronzani, and Francesco Giazotto. Normal metal tunnel junction-based superconducting quantum interference proximity transistor. *Applied Physics Letters*, 107(11):113110, September 2015. ISSN 0003-6951, 1077-3118. doi: 10.1063/1.4930934. URL http://scitation.aip.org/content/aip/journal/apl/107/11/10.1063/1.4930934.

[109] I. O. Kulik. Macroscopic Quantization and the Proximity Effect in S-N-S Junctions. *Soviet Journal of Experimental and Theoretical Physics*, 30:944, January 1969. ISSN 1063-7761.

[110] B. Pannetier and H. Courtois. Andreev Reflection and Proximity effect. *Journal of Low Temperature Physics*, 118(5):599–615, March 2000. ISSN 1573-7357. doi: 10.1023/A:1004635226825.

[111] V. E. Calado, S. Goswami, G. Nanda, M. Diez, A. R. Akhmerov, K. Watanabe, T. Taniguchi, T. M. Klapwijk, and L. M. K. Vandersypen. Ballistic Josephson junctions in edge-contacted graphene. *Nature Nanotechnology*, 10(9):761–764, September 2015. ISSN 1748-3395. doi: 10.1038/nnano.2015.156.

[112] K. W. Lehnert, N. Argaman, H.-R. Blank, K. C. Wong, S. J. Allen, E. L. Hu, and H. Kroemer. Nonequilibrium ac Josephson Effect in Mesoscopic Nb-InAs-Nb Junctions. *Physical Review Letters*, 82(6):1265–1268, February 1999. doi:

10.1103/PhysRevLett.82.1265.

[113] F. Giazotto, K. Grove-Rasmussen, R. Fazio, F. Beltram, E. H. Linfield, and D. A. Ritchie. Josephson Current in Nb/InAs/Nb Highly Transmissive Ballistic Junctions. *Journal of Superconductivity*, 17(2):317–321, April 2004. ISSN 0896-1107. doi: 10.1023/B:JOSC.0000021231.01260.94.

[114] Hermann Sellier, Claire Baraduc, François Lefloch, and Roberto Calemczuk. Half-Integer Shapiro Steps at the 0 - π Crossover of a Ferromagnetic Josephson Junction. *Physical Review Letters*, 92(25):257005, June 2004. ISSN 0031-9007, 1079-7114. doi: 10.1103/PhysRevLett.92.257005.

[115] S. M. Frolov, D. J. Van Harlingen, V. V. Bolginov, V. A. Oboznov, and V. V. Ryazanov. Josephson interferometry and Shapiro step measurements of superconductor-ferromagnet-superconductor $0\text{\ensuremath{-}}\ensuremath{\pi}$ junctions. *Physical Review B*, 74(2):020503, July 2006. doi: 10.1103/PhysRevB.74.020503.

[116] M. Veldhorst, M. Snelder, M. Hoek, T. Gang, V. K. Guduru, X. L. Wang, U. Zeitler, W. G. van der Wiel, A. A. Golubov, H. Hilgenkamp, and A. Brinkman. Josephson supercurrent through a topological insulator surface state. *Nature Materials*, 11 (5):417–421, May 2012. ISSN 1476-4660. doi: 10.1038/nmat3255.

[117] Sean Hart, Hechen Ren, Timo Wagner, Philipp Leubner, Mathias Mühlbauer, Christoph Brüne, Hartmut Buhmann, Laurens W. Molenkamp, and Amir Yacoby. Induced superconductivity in the quantum spin Hall edge. *Nature Physics*, 10(9): 638–643, September 2014. ISSN 1745-2481. doi: 10.1038/nphys3036.

[118] Vlad S. Pribiag, Arjan J. A. Beukman, Fanming Qu, Maja C. Cassidy, Christophe Charpentier, Werner Wegscheider, and Leo P. Kouwenhoven. Edge-mode Superconductivity in a Two Dimensional Topological Insulator. *Nature Nanotechnology*, 10(7):593–597, July 2015. ISSN 1748-3387, 1748-3395. doi: 10.1038/nnano.2015.86.

[119] Fanming Qu, Jasper van Veen, Folkert K. de Vries, Arjan J. A. Beukman, Michael Wimmer, Wei Yi, Andrey A. Kiselev, Binh-Minh Nguyen, Marko Sokolich, Michael J. Manfra, Fabrizio Nichele, Charles M. Marcus, and Leo P. Kouwenhoven. Quantized Conductance and Large g-Factor Anisotropy in InSb Quantum Point Contacts. *Nano Letters*, 16(12):7509–7513, December 2016. ISSN 1530-6984. doi: 10.1021/acs.nanolett.6b03297.

[120] William Mayer, William F. Schiela, Joseph Yuan, Mehdi Hatefipour, Wendy L. Sarney, Stefan P. Svensson, Asher C. Leff, Tiago Campos, Kaushini S. Wickramasinghe, Matthieu C. Dartiailh, Igor Žutić, and Javad Shabani. Superconducting Proximity Effect in InAsSb Surface Quantum Wells with In Situ Al Contacts. *ACS Applied Electronic Materials*, 2(8):2351–2356, August 2020. doi: 10.1021/acsaelm.0c00269.

[121] Christian M. Moehle, Chung Ting Ke, Qingzhen Wang, Candice Thomas, Di Xiao, Saurabh Karwal, Mario Lodari, Vincent van de Kerkhof, Ruben Termaat, Geoffrey C. Gardner, Giordano Scappucci, Michael J. Manfra, and Srijit Goswami. InSbAs Two-Dimensional Electron Gases as a Platform for Topological Superconductivity. *Nano Letters*, 21(23):9990–9996, December 2021. ISSN 1530-6984. doi: 10.1021/acs.nanolett.1c03520.

[122] Zijin Lei, Christian A. Lehner, Erik Cheah, Christopher Mittag, Matija Karalic, Werner Wegscheider, Klaus Ensslin, and Thomas Ihn. Gate-defined quantum point

contact in an InSb two-dimensional electron gas. *Physical Review Research*, 3(2): 023042, April 2021. doi: 10.1103/PhysRevResearch.3.023042.

[123] Yuanjie Chen, Shaoyun Huang, Jingwei Mu, Dong Pan, Jianhua Zhao, and Hong-Qi Xu. A double quantum dot defined by top gates in a single crystalline InSb nanosheet*. *Chinese Physics B*, 30(12):128501, December 2021. ISSN 1674-1056. doi: 10.1088/1674-1056/abff2e.

[124] María de la Mata, Renaud Leturcq, Sébastien R. Plissard, Chloé Rolland, César Magén, Jordi Arbiol, and Philippe Caroff. Twin-Induced InSb Nanosails: A Convenient High Mobility Quantum System. *Nano Letters*, 16(2):825–833, February 2016. ISSN 1530-6984. doi: 10.1021/acs.nanolett.5b05125.

[125] Folkert K. de Vries, Martijn L. Sol, Sasa Gazibegovic, Roy L. M. op het Veld, Stijn C. Balk, Diana Car, Erik P. A. M. Bakkers, Leo P. Kouwenhoven, and Jie Shen. Crossed Andreev reflection in InSb flake Josephson junctions. *Physical Review Research*, 1 (3):032031, December 2019. doi: 10.1103/PhysRevResearch.1.032031.

[126] D. Pan, D. X. Fan, N. Kang, J. H. Zhi, X. Z. Yu, H. Q. Xu, and J. H. Zhao. Free-Standing Two-Dimensional Single-Crystalline InSb Nanosheets. *Nano Letters*, 16 (2):834–841, February 2016. ISSN 1530-6984. doi: 10.1021/acs.nanolett.5b04845.

[127] Jinhua Zhi, Ning Kang, Sen Li, Dingxun Fan, Feifan Su, Dong Pan, Shiping Zhao, Jianhua Zhao, and Hongqi Xu. Supercurrent and Multiple Andreev Reflections in InSb Nanosheet SNS Junctions. *physica status solidi (b)*, 256(6):1800538, 2019. ISSN 1521-3951. doi: 10.1002/pssb.201800538.

[128] Jinhua Zhi, Ning Kang, Feifan Su, Dingxun Fan, Sen Li, Dong Pan, S. P. Zhao, Jianhua Zhao, and H. Q. Xu. Coexistence of induced superconductivity and quantum Hall states in InSb nanosheets. *Physical Review B*, 99(24):245302, June 2019. doi: 10.1103/PhysRevB.99.245302.

[129] Isha Verma, Valentina Zannier, Francesca Rossi, Daniele Ercolani, Fabio Beltram, and Lucia Sorba. Morphology control of single-crystal InSb nanostructures by tuning the growth parameters. *Nanotechnology*, 31(38):384002, July 2020. ISSN 0957-4484. doi: 10.1088/1361-6528/ab9aee.

[130] Ning Kang, Dingxun Fan, Jinhua Zhi, Dong Pan, Sen Li, Cheng Wang, Jingkun Guo, Jianhua Zhao, and Hongqi Xu. Two-Dimensional Quantum Transport in Free-Standing InSb Nanosheets. *Nano Letters*, 19(1):561–569, January 2019. ISSN 1530-6984. doi: 10.1021/acs.nanolett.8b04556.

[131] Jianhong Xue, Yuanjie Chen, Dong Pan, Ji-Yin Wang, Jianhua Zhao, Shaoyun Huang, and H. Q. Xu. Gate defined quantum dot realized in a single crystalline InSb nanosheet. *Applied Physics Letters*, 114(2):023108, January 2019. ISSN 0003-6951. doi: 10.1063/1.5064368.

[132] Yuanjie Chen, Shaoyun Huang, Dong Pan, Jianhong Xue, Li Zhang, Jianhua Zhao, and H. Q. Xu. Strong and tunable spin–orbit interaction in a single crystalline InSb nanosheet. *npj 2D Materials and Applications*, 5(1):1–8, January 2021. ISSN 2397-7132. doi: 10.1038/s41699-020-00184-y.

[133] Sasa Gazibegovic, Ghada Badawy, Thijs L. J. Buckers, Philipp Leubner, Jie Shen, Folkert K. de Vries, Sebastian Koelling, Leo P. Kouwenhoven, Marcel A. Verheijen, and Erik P. A. M. Bakkers. Bottom-Up Grown 2D InSb Nanostructures. *Advanced Materials*, 31(14):1808181, 2019. ISSN 1521-4095. doi: 10.1002/adma.201808181.

[134] Isha Verma, Sedighe Salimian, Valentina Zannier, Stefan Heun, Francesca Rossi,

Daniele Ercolani, Fabio Beltram, and Lucia Sorba. High-Mobility Free-Standing InSb Nanoflags Grown on InP Nanowire Stems for Quantum Devices. *ACS Applied Nano Materials*, 4(6):5825–5833, June 2021. doi: 10.1021/acsanm.1c00734.

[135] Marco Rossi, Ghada Badawy, Zhi-Yuan Zhang, Guang Yang, Guo-An Li, Jia-Yu Shi, Roy L. M. Op het Veld, Sasa Gazibegovic, Lu Li, Jie Shen, Marcel A. Verheijen, and Erik P. A. M. Bakkers. Merging Nanowires and Formation Dynamics of Bottom-Up Grown InSb Nanoflakes. *Advanced Functional Materials*, n/a(n/a):2212029. ISSN 1616-3028. doi: 10.1002/adfm.202212029.

[136] Sedighe Salimian, Matteo Carrega, Isha Verma, Valentina Zannier, Michał P. Nowak, Fabio Beltram, Lucia Sorba, and Stefan Heun. Gate-controlled supercurrent in ballistic InSb nanoflag Josephson junctions. *Applied Physics Letters*, 119 (21):214004, November 2021. ISSN 0003-6951. doi: 10.1063/5.0071218.

[137] Bianca Turini, Sedighe Salimian, Matteo Carrega, Andrea Iorio, Elia Strambini, Francesco Giazotto, Valentina Zannier, Lucia Sorba, and Stefan Heun. Josephson Diode Effect in High-Mobility InSb Nanoflags. *Nano Letters*, October 2022. ISSN 1530-6984. doi: 10.1021/acs.nanolett.2c02899.

[138] Antonio Fornieri, Alexander M. Whiticar, F. Setiawan, Elías Portolés, Asbjørn C. C. Drachmann, Anna Keselman, Sergei Gronin, Candice Thomas, Tian Wang, Ray Kallaher, Geoffrey C. Gardner, Erez Berg, Michael J. Manfra, Ady Stern, Charles M. Marcus, and Fabrizio Nichele. Evidence of topological superconductivity in planar Josephson junctions. *Nature*, 569(7754):89–92, May 2019. ISSN 1476-4687. doi: 10.1038/s41586-019-1068-8.

[139] Elsa Prada, Pablo San-Jose, Michiel W. A. de Moor, Attila Geresdi, Eduardo J. H. Lee, Jelena Klinovaja, Daniel Loss, Jesper Nygård, Ramón Aguado, and Leo P. Kouwenhoven. From Andreev to Majorana bound states in hybrid superconductor–semiconductor nanowires. *Nature Reviews Physics*, 2(10):575–594, October 2020. ISSN 2522-5820. doi: 10.1038/s42254-020-0228-y.

[140] Lucas Casparis, Malcolm R. Connolly, Morten Kjaergaard, Natalie J. Pearson, Anders Kringhøj, Thorvald W. Larsen, Ferdinand Kuemmeth, Tiantian Wang, Candice Thomas, Sergei Gronin, Geoffrey C. Gardner, Michael J. Manfra, Charles M. Marcus, and Karl D. Petersson. Superconducting gatemon qubit based on a proximitized two-dimensional electron gas. *Nature Nanotechnology*, 13(10):915–919, October 2018. ISSN 1748-3395. doi: 10.1038/s41565-018-0207-y.

[141] M. Hays, V. Fatemi, D. Bouman, J. Cerrillo, S. Diamond, K. Serniak, T. Connolly, P. Krogstrup, J. Nygård, A. Levy Yeyati, A. Geresdi, and M. H. Devoret. Coherent manipulation of an Andreev spin qubit. *Science*, 373(6553):430–433, July 2021. doi: 10.1126/science.abf0345.

[142] J. Basset, M. Kuzmanović, P. Virtanen, T. T. Heikkilä, J. Estève, J. Gabelli, C. Strunk, and M. Aprili. Nonadiabatic dynamics in strongly driven diffusive Josephson junctions. *Physical Review Research*, 1(3):032009, October 2019. doi: 10.1103/PhysRevResearch.1.032009.

[143] Gianluigi Catelani and Denis Basko. Non-equilibrium quasiparticles in superconducting circuits: Photons vs. phonons. *SciPost Physics*, 6(1):013, January 2019. ISSN 2542-4653. doi: 10.21468/SciPostPhys.6.1.013.

[144] M. Kjaergaard, H. J. Suominen, M. P. Nowak, A. R. Akhmerov, J. Shabani, C. J. Palmstrøm, F. Nichele, and C. M. Marcus. Transparent Semiconductor-

Superconductor Interface and Induced Gap in an Epitaxial Heterostructure Josephson Junction. *Physical Review Applied*, 7(3):034029, March 2017. ISSN 2331-7019. doi: 10.1103/PhysRevApplied.7.034029.

[145] Trevyn F. Q. Larson, Lingfei Zhao, Ethan G. Arnault, Ming-Tso Wei, Andrew Seredinski, Henming Li, Kenji Watanabe, Takashi Taniguchi, François Amet, and Gleb Finkelstein. Zero Crossing Steps and Anomalous Shapiro Maps in Graphene Josephson Junctions. *Nano Letters*, 20(10):6998–7003, October 2020. ISSN 1530-6984, 1530-6992. doi: 10.1021/acs.nanolett.0c01598.

[146] D. S. Antonenko and M. A. Skvortsov. Quantum decay of the supercurrent and intrinsic capacitance of Josephson junctions beyond the tunnel limit. *Physical Review B*, 92(21):214513, December 2015. ISSN 1098-0121, 1550-235X. doi: 10.1103/PhysRevB.92.214513.

[147] D. Massarotti, N. Banerjee, R. Caruso, G. Rotoli, M. G. Blamire, and F. Tafuri. Electrodynamics of Josephson junctions containing strong ferromagnets. *Physical Review B*, 98(14):144516, October 2018. ISSN 2469-9950, 2469-9969. doi: 10.1103/PhysRevB.98.144516.

[148] Ralf Fischer, Jordi Picó-Cortés, Wolfgang Himmler, Gloria Platero, Milena Grifoni, Dmitriy A. Kozlov, N. N. Mikhailov, Sergey A. Dvoretsky, Christoph Strunk, and Dieter Weiss. 4π -periodic supercurrent tuned by an axial magnetic flux in topological insulator nanowires. *Physical Review Research*, 4(1):013087, February 2022. ISSN 2643-1564. doi: 10.1103/PhysRevResearch.4.013087.

[149] I. V. Borzenets, U. C. Coskun, S. J. Jones, and G. Finkelstein. Phase Diffusion in Graphene-Based Josephson Junctions. *Physical Review Letters*, 107(13):137005, September 2011. doi: 10.1103/PhysRevLett.107.137005.

[150] I. V. Borzenets, F. Amet, C. T. Ke, A. W. Draelos, M. T. Wei, A. Seredinski, K. Watanabe, T. Taniguchi, Y. Bomze, M. Yamamoto, S. Tarucha, and G. Finkelstein. Ballistic Graphene Josephson Junctions from the Short to the Long Junction Regimes. *Physical Review Letters*, 117(23):237002, December 2016. ISSN 0031-9007, 1079-7114. doi: 10.1103/PhysRevLett.117.237002.

[151] Bernhard Mühlschlegel. Die thermodynamischen Funktionen des Supraleiters. *Zeitschrift für Physik*, 155(3):313–327, June 1959. ISSN 0044-3328. doi: 10.1007/BF01332932.

[152] Morteza Kayyalha, Mehdi Kargarian, Aleksandr Kazakov, Ireneusz Miotkowski, Victor M. Galitski, Victor M. Yakovenko, Leonid P. Rokhinson, and Yong P. Chen. Anomalous Low-Temperature Enhancement of Supercurrent in Topological-Insulator Nanoribbon Josephson Junctions: Evidence for Low-Energy Andreev Bound States. *Physical Review Letters*, 122(4):047003, February 2019. doi: 10.1103/PhysRevLett.122.047003.

[153] Peter Schüffelgen, Daniel Rosenbach, Chuan Li, Tobias W. Schmitt, Michael Schleenvoigt, Abdur R. Jalil, Sarah Schmitt, Jonas Kölzer, Meng Wang, Benjamin Bennemann, Umut Parlak, Lidia Kibkalo, Stefan Trellenkamp, Thomas Grap, Doris Meertens, Martina Luysberg, Gregor Mussler, Erwin Berenschot, Niels Tas, Alexander A. Golubov, Alexander Brinkman, Thomas Schäpers, and Detlev Grützmacher. Selective area growth and stencil lithography for in situ fabricated quantum devices. *Nature Nanotechnology*, 14(9):825–831, September 2019. ISSN 1748-3395. doi: 10.1038/s41565-019-0506-y.

[154] Vasily S. Stolyarov, Dmitry S. Yakovlev, Sergei N. Kozlov, Olga V. Skryabina, Dmitry S. Lvov, Amir I. Gumarov, Olga V. Emelyanova, Pavel S. Dzhumaev, Igor V. Shchetinin, Razmik A. Hovhannisyan, Sergey V. Egorov, Andrey M. Kokotin, Walter V. Pogosov, Valery V. Ryazanov, Mikhail Yu Kupriyanov, Alexander A. Golubov, and Dimitri Roditchev. Josephson current mediated by ballistic topological states in Bi2Te2.3Se0.7 single nanocrystals. *Communications Materials*, 1(1):1–11, July 2020. ISSN 2662-4443. doi: 10.1038/s43246-020-0037-y.

[155] Daniel Rosenbach, Tobias W. Schmitt, Peter Schüffelgen, Martin P. Stehno, Chuan Li, Michael Schleenvoigt, Abdur R. Jalil, Gregor Mussler, Elmar Neumann, Stefan Trellenkamp, Alexander A. Golubov, Alexander Brinkman, Detlev Grützmacher, and Thomas Schäpers. Reappearance of first Shapiro step in narrow topological Josephson junctions. *Science Advances*, 7(26):eabf1854, June 2021. ISSN 2375-2548. doi: 10.1126/sciadv.abf1854.

[156] Tobias W. Schmitt, Benedikt Frohn, Wilhelm Wittl, Abdur R. Jalil, Michael Schleenvoigt, Erik Zimmermann, Anne Schmidt, Thomas Schäpers, Juan Carlos Cuevas, Alexander Brinkman, Detlev Grützmacher, and Peter Schüffelgen. Anomalous temperature dependence of multiple Andreev reflections in a topological insulator Josephson junction. *Superconductor Science and Technology*, 36 (2):024002, December 2022. ISSN 0953-2048. doi: 10.1088/1361-6668/aca4fe.

[157] Victor Barzykin and Alexandre M. Zagoskin. Coherent transport and nonlocality in mesoscopic SNS junctions: Anomalous magnetic interference patterns. *Superlattices and Microstructures*, 25(5):797–807, May 1999. ISSN 0749-6036. doi: 10.1006/spmi.1999.0731.

[158] Tycho J. Blom, Thomas W. Mechielsen, Remko Fermin, Marcel B. S. Hesselberth, Jan Aarts, and Kaveh Lahabi. Direct-Write Printing of Josephson Junctions in a Scanning Electron Microscope. *ACS Nano*, 15(1):322–329, January 2021. ISSN 1936-0851. doi: 10.1021/acsnano.0c03656.

[159] A. I. Gubin, K. S. Il'in, S. A. Vitusevich, M. Siegel, and N. Klein. Dependence of magnetic penetration depth on the thickness of superconducting Nb thin films. *Physical Review B*, 72(6):064503, August 2005. doi: 10.1103/PhysRevB.72.064503.

[160] A. D. Zaikin. Nonstationary Josephson effect and nonequilibrium properties of SNS junctions. *Zh. Eksp. Teor. Fiz*, 84:1560–1573, 1983.

[161] Nathan Argaman. Nonequilibrium Josephson-like effects in wide mesoscopic SNS junctions. *Superlattices and Microstructures*, 25(5):861–875, May 1999. ISSN 0749-6036. doi: 10.1006/spmi.1999.0724.

[162] P. Dubos, H. Courtois, O. Buisson, and B. Pannetier. Coherent Low-Energy Charge Transport in a Diffusive S-N-S Junction. *Physical Review Letters*, 87(20):206801, October 2001. ISSN 0031-9007, 1079-7114. doi: 10.1103/PhysRevLett.87.206801.

[163] B. Dassonneville, A. Murani, M. Ferrier, S. Guéron, and H. Bouchiat. Coherence-enhanced phase-dependent dissipation in long SNS Josephson junctions: Revealing Andreev bound state dynamics. *Physical Review B*, 97(18):184505, May 2018. ISSN 2469-9950, 2469-9969. doi: 10.1103/PhysRevB.97.184505.

[164] Kento Ueda, Sadashige Matsuo, Hiroshi Kamata, Yosuke Sato, Yuusuke Takeshige, Kan Li, Lars Samuelson, Hongqi Xu, and Seigo Tarucha. Evidence of half-integer Shapiro steps originated from nonsinusoidal current phase relation in a short ballistic InAs nanowire Josephson junction. *Physical Review Research*, 2(3):033435,

September 2020. ISSN 2643-1564. doi: 10.1103/PhysRevResearch.2.033435.

[165] J. Pfeiffer, M. Kemmler, D. Koelle, R. Kleiner, E. Goldobin, M. Weides, A. K. Feofanov, J. Lisenfeld, and A. V. Ustinov. Static and dynamic properties of 0, $\ensuremath{\pi}$, and $0\text{\ensuremath{-}}\ensuremath{\pi}$ ferromagnetic Josephson tunnel junctions. *Physical Review B*, 77(21):214506, June 2008. doi: 10.1103/PhysRevB.77.214506.

[166] M. J. A. Stoutimore, A. N. Rossolenko, V. V. Bolginov, V. A. Oboznov, A. Y. Rusanov, D. S. Baranov, N. Pugach, S. M. Frolov, V. V. Ryazanov, and D. J. Van Harlingen. Second-Harmonic Current-Phase Relation in Josephson Junctions with Ferromagnetic Barriers. *Physical Review Letters*, 121(17):177702, October 2018. ISSN 0031-9007, 1079-7114. doi: 10.1103/PhysRevLett.121.177702.

[167] O. O. Shvetsov, A. Kononov, A. V. Timonina, N. N. Kolesnikov, and E. V. Deviatov. Subharmonic Shapiro steps in the a.c. Josephson effect for a three-dimensional Weyl semimetal WTe $_2$. *EPL (Europhysics Letters)*, 124(4):47003, December 2018. ISSN 1286-4854. doi: 10.1209/0295-5075/124/47003.

[168] C. J. Trimble, M. T. Wei, N. F. Q. Yuan, S. S. Kalantre, P. Liu, H.-J. Han, M.-G. Han, Y. Zhu, J. J. Cha, L. Fu, and J. R. Williams. Josephson detection of time-reversal symmetry broken superconductivity in SnTe nanowires. *npj Quantum Materials*, 6(1):1–6, June 2021. ISSN 2397-4648. doi: 10.1038/s41535-021-00359-w.

[169] Ulrich Eckern, Gerd Schön, and Vinay Ambegaokar. Quantum dynamics of a superconducting tunnel junction. *Physical Review B*, 30(11):6419–6431, December 1984. doi: 10.1103/PhysRevB.30.6419.

[170] C.A. Hamilton and E.G. Johnson. Analog computer studies of subharmonic steps in superconducting weak links. *Physics Letters A*, 41(4):393–394, October 1972. ISSN 03759601. doi: 10.1016/0375-9601(72)90945-0.

[171] Trevyn F. Q. Larson, Lingfei Zhao, Ethan G. Arnault, Ming-Tso Wei, Andrew Seredinski, Hengming Li, Kenji Watanabe, Takashi Tanaguchi, François Amet, and Gleb Finkelstein. Noise-induced stabilization of dynamical states in a non-Markovian system, December 2022.

[172] K. H. Lee, D. Stroud, and J. S. Chung. Calculation of giant fractional Shapiro steps in Josephson-junction arrays. *Physical Review Letters*, 64(8):962–965, February 1990. doi: 10.1103/PhysRevLett.64.962.

[173] Hyun C. Lee, R. S. Newrock, D. B. Mast, S. E. Hebboul, J. C. Garland, and C. J. Lobb. Subharmonic Shapiro steps in Josephson-junction arrays. *Physical Review B*, 44 (2):921–924, July 1991. ISSN 0163-1829, 1095-3795. doi: 10.1103/PhysRevB.44.921.

[174] Erik Heinz and Paul Seidel. Microwave-induced steps in Josephson junctions, DC-SQUIDs and parallel arrays. *Journal of Low Temperature Physics*, 106(3-4):233–242, February 1997. ISSN 0022-2291, 1573-7357. doi: 10.1007/BF02399620.

[175] A. Valizadeh, M. R. Kolahchi, and J. P. Straley. Fractional Shapiro steps in a triangular single-plaquette Josephson-junction array. *Physical Review B*, 76(21):214511, December 2007. ISSN 1098-0121, 1550-235X. doi: 10.1103/PhysRevB.76.214511.

[176] R. Panghotra, B. Raes, Clécio C. de Souza Silva, I. Cools, W. Keijers, J. E. Scheerder, V. V. Moshchalkov, and J. Van de Vondel. Giant fractional Shapiro steps in anisotropic Josephson junction arrays. *Communications Physics*, 3(1):1–8, March 2020. ISSN 2399-3650. doi: 10.1038/s42005-020-0315-5.

[177] François Amet, Sara Idris, Aeron McConnell, Brian Opatosky, and Ethan Arnault.

Phase dynamics in an AC-driven multiterminal Josephson junction analog. *Physical Review B*, 106(17):174509, November 2022. doi: 10.1103/PhysRevB.106.174509.

[178] C. Vanneste, C. C. Chi, W. J. Gallagher, A. W. Kleinsasser, S. I. Raider, and R. L. Sandstrom. Shapiro steps on current-voltage curves of dc SQUIDs. *Journal of Applied Physics*, 64(1):242–245, July 1988. ISSN 0021-8979. doi: 10.1063/1.341471.

[179] E. A. Early, A. F. Clark, and C. J. Lobb. Physical basis for half-integral Shapiro steps in a DC SQUID. *Physica C: Superconductivity*, 245(3):308–320, April 1995. ISSN 0921-4534. doi: 10.1016/0921-4534(95)00126-3.

[180] E. A. Early, A. F. Clark, and K. Char. Half-integral constant voltage steps in high- T_c grain boundary junctions. *Applied Physics Letters*, 62(25):3357–3359, June 1993. ISSN 0003-6951, 1077-3118. doi: 10.1063/1.109070.

[181] D. Terpstra, R. P. J. IJsselsteijn, and H. Rogalla. Subharmonic Shapiro steps in high- T_c Josephson junctions. *Applied Physics Letters*, 66(17):2286–2288, April 1995. ISSN 0003-6951, 1077-3118. doi: 10.1063/1.113194.

[182] L.C. Ku, H.M. Cho, and S.W. Wang. The origin of the half-integral constant voltage steps in high-Tc grain-boundary junction. *Physica C: Superconductivity*, 243(1-2): 187–190, February 1995. ISSN 09214534. doi: 10.1016/0921-4534(94)02457-X.

[183] H. C. Yang, L. C. Ku, H. M. Cho, J. H. Lu, and H. E. Horng. Observation of half-integer Shapiro steps in step-edge YBa2Cu3Oy Josephson junctions. *Physica C: Superconductivity*, 235–240:3341–3342, December 1994. ISSN 0921-4534. doi: 10.1016/0921-4534(94)91197-5.

[184] Herbert Kroemer. Quasiparticle dynamics in ballistic weak links under weak voltage bias: An elementary treatment. *Superlattices and Microstructures*, 25(5):877–889, May 1999. ISSN 0749-6036. doi: 10.1006/spmi.1999.0704.

[185] K. Biedermann, A. Chrestin, T. Matsuyama, and U. Merkt. Ac Josephson effects in Nb/InAs/Nb junctions with integrated resonators. *Physical Review B*, 63 (14):144512, March 2001. ISSN 0163-1829, 1095-3795. doi: 10.1103/PhysRevB.63.144512.

[186] J. J. A. Baselmans, T. T. Heikkilä, B. J. van Wees, and T. M. Klapwijk. Direct Observation of the Transition from the Conventional Superconducting State to the π State in a Controllable Josephson Junction. *Physical Review Letters*, 89(20):207002, October 2002. ISSN 0031-9007, 1079-7114. doi: 10.1103/PhysRevLett.89.207002.

[187] Arne Jacobs and Reiner Kümmel. Andreev scattering, Zener tunneling, and anomalous ac Josephson effect in near-ballistic quasi-two-dimensional weak links. *Physical Review B*, 71(18):184504, May 2005. ISSN 1098-0121, 1550-235X. doi: 10.1103/PhysRevB.71.184504.

[188] D. Z. Haxell, M. Coraiola, D. Sabonis, M. Hinderling, S. C. ten Kate, E. Cheah, F. Krizek, R. Schott, W. Wegscheider, W. Belzig, J. C. Cuevas, and F. Nichele. Microwave-induced conductance replicas in hybrid Josephson junctions without Floquet-Andreev states, December 2022.

[189] K. Flensberg, J. Bindslev Hansen, and M. Octavio. Subharmonic energy-gap structure in superconducting weak links. *Physical Review B*, 38(13):8707–8711, November 1988. doi: 10.1103/PhysRevB.38.8707.

[190] B. A. Aminov, A. A. Golubov, and M. Yu. Kupriyanov. Quasiparticle current in ballistic constrictions with finite transparencies of interfaces. *Physical Review B*, 53(1):365–373, January 1996. doi: 10.1103/PhysRevB.53.365.

[191] J. C. Cuevas and A. Levy Yeyati. Subharmonic gap structure in short ballistic graphene junctions. *Physical Review B*, 74(18):180501, November 2006. doi: 10.1103/PhysRevB.74.180501.

[192] G. De Simoni, F. Paolucci, P. Solinas, E. Strambini, and F. Giazotto. Metallic supercurrent field-effect transistor. *Nature Nanotechnology*, 13(9):802–805, September 2018. ISSN 1748-3387, 1748-3395. doi: 10.1038/s41565-018-0190-3.

[193] Federico Paolucci, Giorgio De Simoni, Elia Strambini, Paolo Solinas, and Francesco Giazotto. Ultra-efficient superconducting Dayem bridge field-effect transistor. *Nano Letters*, 18(7):4195–4199, July 2018. ISSN 1530-6984, 1530-6992. doi: 10.1021/acs.nanolett.8b01010.

[194] Federico Paolucci, Francesco Vischi, Giorgio De Simoni, Claudio Guarcello, Paolo Solinas, and Francesco Giazotto. Field-Effect Controllable Metallic Josephson Interferometer. *Nano Letters*, 19(9):6263–6269, September 2019. ISSN 1530-6984, 1530-6992. doi: 10.1021/acs.nanolett.9b02369.

[195] Giorgio De Simoni, Federico Paolucci, Claudio Puglia, and Francesco Giazotto. Josephson Field-Effect Transistors Based on All-Metallic Al/Cu/Al Proximity Nanojunctions. *ACS Nano*, 13(7):7871–7876, July 2019. ISSN 1936-0851, 1936-086X. doi: 10.1021/acsnano.9b02209.

[196] C. Puglia, G. De Simoni, and F. Giazotto. Electrostatic control of phase slips in Ti Josephson nanotransistors. *Physical Review Applied*, 13(5):054026, May 2020. ISSN 2331-7019. doi: 10.1103/PhysRevApplied.13.054026.

[197] Lennart Bours, Björn Sothmann, Matteo Carrega, Elia Strambini, Alessandro Braggio, Ewelina M. Hankiewicz, Laurens W. Molenkamp, and Francesco Giazotto. Phase-tunable thermal rectification in the topological SQUIPT. *Physical Review Applied*, 11(4):044073, April 2019. ISSN 2331-7019. doi: 10.1103/PhysRevApplied.11.044073.

[198] Maria Teresa Mercaldo, Paolo Solinas, Francesco Giazotto, and Mario Cuoco. Electrically Tunable Superconductivity Through Surface Orbital Polarization. *Physical Review Applied*, 14(3):034041, September 2020. doi: 10.1103/PhysRevApplied.14.034041.

[199] Paolo Solinas, Andrea Amoretti, and Francesco Giazotto. Schwinger effect in a Bardeen-Cooper-Schrieffer superconductor. *Physical Review Letters*, 126(11):117001, March 2021. ISSN 0031-9007, 1079-7114. doi: 10.1103/PhysRevLett.126.117001.

[200] Andrea Amoretti, Daniel K. Brattan, Nicodemo Magnoli, Luca Martinoia, Ioannis Matthaiakakis, and Paolo Solinas. Destroying superconductivity in thin films with an electric field. *Physical Review Research*, 4(3):033211, September 2022. ISSN 2643-1564. doi: 10.1103/PhysRevResearch.4.033211.

[201] Maria Teresa Mercaldo, Carmine Ortix, Francesco Giazotto, and Mario Cuoco. Zero magnetic-field orbital vortices in s-wave spin-singlet superconductors. *Physical Review B*, 105(14):L140507, April 2022. ISSN 2469-9950, 2469-9969. doi: 10.1103/PhysRevB.105.L140507.

[202] Loren D. Alegria, Charlotte G. Bøttcher, Andrew K. Saydjari, Andrew T. Pierce, Seung H. Lee, Shannon P. Harvey, Uri Vool, and Amir Yacoby. High-Energy Quasiparticle Injection into Mesoscopic Superconductors. *Nature Nanotechnology*, 16(4):404–408, April 2021. ISSN 1748-3387, 1748-3395. doi: 10.1038/s41565-020-00834-8.

[203] Ilia Golokolenov, Andrew Guthrie, Sergey Kafanov, Yuri Pashkin, and Viktor Tsepelin. On the origin of the controversial electrostatic field effect in superconductors. *Nature Communications*, 12(1):2747, May 2021. ISSN 2041-1723. doi: 10.1038/s41467-021-22998-0.

[204] Julien Basset, Ognjen Stanisavljević, Marko Kuzmanović, Julien Gabelli, Charis Quay, Jérôme Estève, and Marco Aprili. Gate-Assisted Phase Fluctuations in All-Metallic Josephson Junctions, July 2021.

[205] M. F. Ritter, A. Fuhrer, D. Z. Haxell, S. Hart, P. Gumann, H. Riel, and F. Nichele. A superconducting switch actuated by injection of high energy electrons. *Nature Communications*, 12(1):1266, February 2021. ISSN 2041-1723. doi: 10.1038/s41467-021-21231-2.

[206] M. F. Ritter, N. Crescini, D. Z. Haxell, M. Hinderling, H. Riel, C. Bruder, A. Fuhrer, and F. Nichele. On the Role of Out-of-Equilibrium Phonons in Gated Superconducting Switches. *Nature Electronics*, 5(2):71–77, February 2022. ISSN 2520-1131. doi: 10.1038/s41928-022-00721-1.

[207] Tosson Elalaily, Martin Berke, Máté Kedves, Gergő Fülöp, Zoltán Scherübl, Thomas Kanne, Jesper Nygård, Péter Makk, and Szabolcs Csonka. Signatures of gate-driven out of equilibrium superconductivity in Ta/InAs nanowires, October 2022.

[208] Giorgio De Simoni, Sebastiano Battisti, Nadia Ligato, Maria Teresa Mercaldo, Mario Cuoco, and Francesco Giazotto. Gate-control of the current-flux relation of a Josephson quantum interferometer based on proximitized metallic nanojunctions. *ACS Applied Electronic Materials*, 3(9):3927–3935, September 2021. ISSN 2637-6113, 2637-6113. doi: 10.1021/acsaelm.1c00508.

[209] Mirko Rocci, Giorgio De Simoni, Claudio Puglia, Davide Degli Esposti, Elia Strambini, Valentina Zannier, Lucia Sorba, and Francesco Giazotto. Gate-Controlled Suspended Titanium Nanobridge Supercurrent Transistor. *ACS Nano*, August 2020. ISSN 1936-0851. doi: 10.1021/acsnano.0c05355.

[210] Federico Paolucci, Francesco Crisà, Giorgio De Simoni, Lennart Bours, Claudio Puglia, Elia Strambini, Stefano Roddaro, and Francesco Giazotto. Electrostatic field-driven supercurrent suppression in ionic-gated metallic Josephson nanotransistors. *Nano Letters*, 21(24):10309–10314, December 2021. ISSN 1530-6984, 1530-6992. doi: 10.1021/acs.nanolett.1c03481.

[211] Luca Chirolli, Tommaso Cea, and Francesco Giazotto. Impact of electrostatic fields in layered crystalline BCS superconductors. *Physical Review Research*, 3(2):023135, May 2021. ISSN 2643-1564. doi: 10.1103/PhysRevResearch.3.023135.

[212] A. M. Kadin and M. W. Johnson. Nonequilibrium photon-induced hotspot: A new mechanism for photodetection in ultrathin metallic films. *Applied Physics Letters*, 69(25):3938–3940, December 1996. ISSN 0003-6951. doi: 10.1063/1.117576.

[213] G. N. Gol'tsman, O. Okunev, G. Chulkova, A. Lipatov, A. Semenov, K. Smirnov, B. Voronov, A. Dzardanov, C. Williams, and Roman Sobolewski. Picosecond superconducting single-photon optical detector. *Applied Physics Letters*, 79(6):705–707, August 2001. ISSN 0003-6951. doi: 10.1063/1.1388868.

[214] K. Karatsu, A. Endo, J. Bueno, P. J. de Visser, R. Barends, D. J. Thoen, V. Murugesan, N. Tomita, and J. J. A. Baselmans. Mitigation of cosmic ray effect on microwave kinetic inductance detector arrays. *Applied Physics Letters*, 114(3):032601, January

2019. ISSN 0003-6951. doi: 10.1063/1.5052419.

[215] Matt McEwen, Lara Faoro, Kunal Arya, Andrew Dunsworth, Trent Huang, Seon Kim, Brian Burkett, Austin Fowler, Frank Arute, Joseph C. Bardin, Andreas Bengtsson, Alexander Bilmes, Bob B. Buckley, Nicholas Bushnell, Zijun Chen, Roberto Collins, Sean Demura, Alan R. Derk, Catherine Erickson, Marissa Giustina, Sean D. Harrington, Sabrina Hong, Evan Jeffrey, Julian Kelly, Paul V. Klimov, Fedor Kostritsa, Pavel Laptev, Aditya Locharla, Xiao Mi, Kevin C. Miao, Shirin Montazeri, Josh Mutus, Ofer Naaman, Matthew Neeley, Charles Neill, Alex Opremcak, Chris Quintana, Nicholas Redd, Pedram Roushan, Daniel Sank, Kevin J. Satzinger, Vladimir Shvarts, Theodore White, Z. Jamie Yao, Ping Yeh, Juhwan Yoo, Yu Chen, Vadim Smelyanskiy, John M. Martinis, Hartmut Neven, Anthony Megrant, Lev Ioffe, and Rami Barends. Resolving catastrophic error bursts from cosmic rays in large arrays of superconducting qubits. *Nature Physics*, 18(1): 107–111, January 2022. ISSN 1745-2481. doi: 10.1038/s41567-021-01432-8.

[216] Tosson Elalaily, Olivér Kürtössy, Zoltán Scherübl, Martin Berke, Gergő Fülöp, István Endre Lukács, Thomas Kanne, Jesper Nygård, Kenji Watanabe, Takashi Taniguchi, Péter Makk, and Szabolcs Csonka. Gate-controlled supercurrent in epitaxial Al/InAs nanowires. *Nano Letters*, 21(22):9684–9690, November 2021. ISSN 1530-6984, 1530-6992. doi: 10.1021/acs.nanolett.1c03493.

[217] W. Eisenmenger and A. H. Dayem. Quantum Generation and Detection of Incoherent Phonons in Superconductors. *Physical Review Letters*, 18(4):125–127, January 1967. ISSN 0031-9007. doi: 10.1103/PhysRevLett.18.125.

[218] M. Welte, K. Lassmann, and W. Eisenmenger. EMISSION OF HIGH FREQUENCY RELAXATION PHONONS BY SUPERCONDUCTING ALUMINIUM TUNNELLING JUNCTIONS. *Le Journal de Physique Colloques*, 33(C4):C4–25–C4–27, October 1972. ISSN 0449-1947. doi: 10.1051/jphyscol:1972406.

[219] J. Wenner, Yi Yin, Erik Lucero, R. Barends, Yu Chen, B. Chiaro, J. Kelly, M. Lenander, Matteo Mariantoni, A. Megrant, C. Neill, P. J. J. O'Malley, D. Sank, A. Vainsencher, H. Wang, T. C. White, A. N. Cleland, and John M. Martinis. Excitation of Superconducting Qubits from Hot Nonequilibrium Quasiparticles. *Physical Review Letters*, 110(15):150502, April 2013. ISSN 0031-9007, 1079-7114. doi: 10.1103/PhysRevLett.110.150502.

[220] Arno Bargerbos, Lukas Johannes Splitthoff, Marta Pita-Vidal, Jaap J. Wesdorp, Yu Liu, Peter Krogstrup, Leo P. Kouwenhoven, Christian Kraglund Andersen, and Lukas Grünhaupt. Mitigation of Quasiparticle Loss in Superconducting Qubits by Phonon Scattering. *Physical Review Applied*, 19(2):024014, February 2023. doi: 10.1103/PhysRevApplied.19.024014.

[221] Bernard Yurke and Eyal Buks. Performance of Cavity-Parametric Amplifiers, Employing Kerr Nonlinearites, in the Presence of Two-Photon Loss. *Journal of Lightwave Technology*, 24(12):5054–5066, December 2006. ISSN 1558-2213. doi: 10.1109/JLT.2006.884490.

[222] Erik A. Tholén, Adem Ergül, Evelyn M. Doherty, Frank M. Weber, Fabien Grégis, and David B. Haviland. Nonlinearities and parametric amplification in superconducting coplanar waveguide resonators. *Applied Physics Letters*, 90(25):253509, June 2007. ISSN 0003-6951. doi: 10.1063/1.2750520.

[223] A. Eichler, R. Deblock, M. Weiss, C. Karrasch, V. Meden, C. Schönenberger, and

H. Bouchiat. Tuning the Josephson current in carbon nanotubes with the Kondo effect. *Physical Review B*, 79(16):161407, April 2009. ISSN 1098-0121, 1550-235X. doi: 10.1103/PhysRevB.79.161407.

[224] Jukka P. Pekola. Towards quantum thermodynamics in electronic circuits. *Nature Physics*, 11(2):118–123, February 2015. ISSN 1745-2481. doi: 10.1038/nphys3169.

[225] Janet Anders and Massimiliano Esposito. Focus on quantum thermodynamics. *New Journal of Physics*, 19(1):010201, January 2017. ISSN 1367-2630. doi: 10.1088/1367-2630/19/1/010201.

[226] Antonio Fornieri and Francesco Giazotto. Towards phase-coherent caloritronics in superconducting circuits. *Nature Nanotechnology*, 12(10):944–952, October 2017. ISSN 1748-3387, 1748-3395. doi: 10.1038/nnano.2017.204.

[227] Felix Binder, Luis A. Correa, Christian Gogolin, Janet Anders, and Gerardo Adesso, editors. *Thermodynamics in the Quantum Regime: Fundamental Aspects and New Directions*. Fundamental Theories of Physics. Springer International Publishing, 2018. ISBN 978-3-319-99045-3. doi: 10.1007/978-3-319-99046-0.

[228] Francesco Vischi, Matteo Carrega, Pauli Virtanen, Elia Strambini, Alessandro Braggio, and Francesco Giazotto. Coherent Josephson thermodynamic cycles. *Scientific Reports*, 9(1):3238, December 2019. ISSN 2045-2322. doi: 10.1038/s41598-019-40202-8.

[229] M. J. Martinez-Perez and F. Giazotto. Fully-Balanced Heat Interferometer. *Applied Physics Letters*, 102(9):092602, March 2013. ISSN 0003-6951, 1077-3118. doi: 10.1063/1.4794412.

[230] Claudio Guarcello, Paolo Solinas, Massimiliano Di Ventra, and Francesco Giazotto. Hysteretic superconducting heat-flux quantum modulator. *Physical Review Applied*, 7(4), April 2017. ISSN 2331-7019. doi: 10.1103/PhysRevApplied.7.044021.

[231] Sun-Yong Hwang, Francesco Giazotto, and Björn Sothmann. Phase-coherent heat circulator based on multi-terminal Josephson junctions. *Physical Review Applied*, 10(4), October 2018. ISSN 2331-7019. doi: 10.1103/PhysRevApplied.10.044062.

[232] Claudio Guarcello, Paolo Solinas, Alessandro Braggio, and Francesco Giazotto. Phase-coherent solitonic Josephson heat oscillator. *Scientific Reports*, 8(1), December 2018. ISSN 2045-2322. doi: 10.1038/s41598-018-30268-1.

[233] A. O. Niskanen, Y. Nakamura, and J. P. Pekola. Information entropic superconducting microcooler. *Physical Review B*, 76(17):174523, November 2007. ISSN 1098-0121, 1550-235X. doi: 10.1103/PhysRevB.76.174523.

[234] P. Solinas, M. Möttönen, J. Salmilehto, and J. P. Pekola. Cooper-pair current in the presence of flux noise. *Physical Review B*, 85(2):024527, January 2012. ISSN 1098-0121, 1550-235X. doi: 10.1103/PhysRevB.85.024527.

[235] Nicolas Brunner, Marcus Huber, Noah Linden, Sandu Popescu, Ralph Silva, and Paul Skrzypczyk. Entanglement enhances cooling in microscopic quantum refrigerators. *Physical Review E*, 89(3):032115, March 2014. doi: 10.1103/PhysRevE.89.032115.

[236] Paolo Solinas, Riccardo Bosisio, and Francesco Giazotto. A Microwave Josephson Refrigerator. *Physical Review B*, 93(22), June 2016. ISSN 2469-9950, 2469-9969. doi: 10.1103/PhysRevB.93.224521.

[237] Teemu Ojanen and Antti-Pekka Jauho. Mesoscopic Photon Heat Transistor. *Physical Review Letters*, 100(15):155902, April 2008. ISSN 0031-9007, 1079-7114. doi:

10.1103/PhysRevLett.100.155902.

[238] Björn Sothmann, Francesco Giazotto, and Ewelina M. Hankiewicz. High efficiency thermal switch based on topological Josephson junctions. *New Journal of Physics*, 19(2):023056, February 2017. ISSN 1367-2630. doi: 10.1088/1367-2630/aa60d4.

[239] Bayan Karimi and Jukka P. Pekola. Correlated vs. uncorrelated noise acting on a quantum refrigerator. *Physical Review B*, 96(11):115408, September 2017. ISSN 2469-9950, 2469-9969. doi: 10.1103/PhysRevB.96.115408.

[240] Alberto Ronzani, Bayan Karimi, Jorden Senior, Yu-Cheng Chang, Joonas T. Peltonen, ChiiDong Chen, and Jukka P. Pekola. Tunable photonic heat transport in a quantum heat valve. *Nature Physics*, 14(10):991–995, October 2018. ISSN 1745-2473, 1745-2481. doi: 10.1038/s41567-018-0199-4.

[241] B. Dutta, D. Majidi, N. W. Talarico, N. Lo Gullo, H. Courtois, and C. B. Winkelmann. Single-Quantum-Dot Heat Valve. *Physical Review Letters*, 125(23):237701, December 2020. doi: 10.1103/PhysRevLett.125.237701.

[242] Patrick P. Hofer and Björn Sothmann. Quantum heat engines based on electronic Mach-Zehnder interferometers. *Physical Review B*, 91(19):195406, May 2015. doi: 10.1103/PhysRevB.91.195406.

[243] G. Marchegiani, P. Virtanen, F. Giazotto, and M. Campisi. Self-Oscillating Josephson Quantum Heat Engine. *Physical Review Applied*, 6(5):054014, November 2016. doi: 10.1103/PhysRevApplied.6.054014.

[244] Peter Samuelsson, Sara Kheradsoud, and Björn Sothmann. Optimal Quantum Interference Thermoelectric Heat Engine with Edge States. *Physical Review Letters*, 118(25):256801, June 2017. doi: 10.1103/PhysRevLett.118.256801.

[245] Géraldine Haack and Francesco Giazotto. Efficient and tunable Aharonov-Bohm quantum heat engine. *Physical Review B*, 100(23):235442, December 2019. doi: 10.1103/PhysRevB.100.235442.

[246] P A Erdman, V Cavina, R Fazio, F Taddei, and V Giovannetti. Maximum power and corresponding efficiency for two-level heat engines and refrigerators: Optimality of fast cycles. *New Journal of Physics*, 21(10):103049, October 2019. ISSN 1367-2630. doi: 10.1088/1367-2630/ab4dca.

[247] Benedikt Scharf, Alessandro Braggio, Elia Strambini, Francesco Giazotto, and Ewelina M. Hankiewicz. Topological Josephson Heat Engine. *arXiv:2002.05492 [cond-mat]*, February 2020.

[248] G. Marchegiani, A. Braggio, and F. Giazotto. Highly efficient phase-tunable photonic thermal diode. *Applied Physics Letters*, 118(2):022602, January 2021. ISSN 0003-6951, 1077-3118. doi: 10.1063/5.0036485.

[249] Lorenzo Buffoni and Michele Campisi. Thermodynamics of a quantum annealer. *Quantum Science and Technology*, 5(3):035013, June 2020. ISSN 2058-9565. doi: 10.1088/2058-9565/ab9755.

[250] Jonatan Bohr Brask, Géraldine Haack, Nicolas Brunner, and Marcus Huber. Autonomous quantum thermal machine for generating steady-state entanglement. *New Journal of Physics*, 17(11):113029, November 2015. ISSN 1367-2630. doi: 10.1088/1367-2630/17/11/113029.

[251] Shishir Khandelwal, Nicolas Palazzo, Nicolas Brunner, and Géraldine Haack. Critical heat current for operating an entanglement engine. *New Journal of Physics*, 22(7):073039, July 2020. ISSN 1367-2630. doi: 10.1088/1367-2630/ab9983.

[252] Milton Aguilar, Nahuel Freitas, and Juan Pablo Paz. Entanglement generation in quantum thermal machines. *Physical Review A*, 102(6):062422, December 2020. ISSN 2469-9926, 2469-9934. doi: 10.1103/PhysRevA.102.062422.

[253] F. Giazotto and F. S. Bergeret. Thermal rectification of electrons in hybrid normal metal-superconductor nanojunctions. *Applied Physics Letters*, 103(24):242602, December 2013. ISSN 0003-6951, 1077-3118. doi: 10.1063/1.4846375.

[254] M. J. Martinez-Perez and F. Giazotto. Efficient phase-tunable Josephson thermal rectifier. *Applied Physics Letters*, 102(18):182602, May 2013. ISSN 0003-6951, 1077-3118. doi: 10.1063/1.4804550.

[255] A. Fornieri, M. J. Martinez-Perez, and F. Giazotto. A normal metal tunnel-junction heat diode. *Applied Physics Letters*, 104(18):183108, May 2014. ISSN 0003-6951, 1077-3118. doi: 10.1063/1.4875917.

[256] M. J. Martínez-Pérez, A. Fornieri, and F. Giazotto. Rectification of electronic heat current by a hybrid thermal diode. *Nature Nanotechnology*, 10(4):303–307, May 2015. ISSN 1748-3387, 1748-3395. doi: 10.1038/nnano.2015.11.

[257] F. Giazotto and F. S. Bergeret. Very large thermal rectification in ferromagnetic insulator-based superconducting tunnel junctions. *Applied Physics Letters*, 116 (19):192601, May 2020. ISSN 0003-6951, 1077-3118. doi: 10.1063/5.0010148.

[258] D. R. Schmidt, R. J. Schoelkopf, and A. N. Cleland. Photon-Mediated Thermal Relaxation of Electrons in Nanostructures. *Physical Review Letters*, 93(4):045901, July 2004. doi: 10.1103/PhysRevLett.93.045901.

[259] Matthias Meschke, Wiebke Guichard, and Jukka P. Pekola. Single-mode heat conduction by photons. *Nature*, 444(7116):187–190, November 2006. ISSN 1476-4687. doi: 10.1038/nature05276.

[260] Tomi Ruokola, Teemu Ojanen, and Antti-Pekka Jauho. Thermal rectification in nonlinear quantum circuits. *Physical Review B*, 79(14):144306, April 2009. ISSN 1098-0121, 1550-235X. doi: 10.1103/PhysRevB.79.144306.

[261] R. Bosisio, P. Solinas, A. Braggio, and F. Giazotto. Photonic heat conduction in Josephson-coupled Bardeen-Cooper-Schrieffer superconductors. *Physical Review B*, 93(14):144512, April 2016. doi: 10.1103/PhysRevB.93.144512.

[262] Michele Campisi, Ralf Blattmann, Sigmund Kohler, David Zueco, and Peter Hänggi. Employing circuit QED to measure non-equilibrium work fluctuations. *New Journal of Physics*, 15(10):105028, October 2013. ISSN 1367-2630. doi: 10.1088/1367-2630/15/10/105028.

[263] Jukka P. Pekola and Bayan Karimi. Qubit decay in circuit quantum thermodynamics. *arXiv:2010.11122 [cond-mat, physics:quant-ph]*, October 2020.

[264] Matti Partanen, Kuan Yen Tan, Joonas Govenius, Russell E. Lake, Miika K. Mäkelä, Tuomo Tanttu, and Mikko Möttönen. Quantum-limited heat conduction over macroscopic distances. *Nature Physics*, 12(5):460–464, May 2016. ISSN 1745-2481. doi: 10.1038/nphys3642.

[265] Jorden Senior, Azat Gubaydullin, Bayan Karimi, Joonas T. Peltonen, Joachim Ankerhold, and Jukka P. Pekola. Heat rectification via a superconducting artificial atom. *Communications Physics*, 3(1):40, December 2020. ISSN 2399-3650. doi: 10.1038/s42005-020-0307-5.

[266] Michele Campisi, Jukka Pekola, and Rosario Fazio. Nonequilibrium fluctuations in quantum heat engines: Theory, example, and possible solid state experiments.

New Journal of Physics, 17(3):035012, March 2015. ISSN 1367-2630. doi: 10.1088/1367-2630/17/3/035012.

[267] Vinitha Balachandran, Giuliano Benenti, Emmanuel Pereira, Giulio Casati, and Dario Poletti. Perfect Diode in Quantum Spin Chains. *Physical Review Letters*, 120 (20):200603, May 2018. doi: 10.1103/PhysRevLett.120.200603.

[268] Marzie Jamshidi Farsani and Rosario Fazio. Quantum heat switch with multiple qubits. *Physics Letters A*, 383(15):1722–1727, May 2019. ISSN 0375-9601. doi: 10.1016/j.physleta.2019.02.045.

[269] Fabien Clivaz, Ralph Silva, Géraldine Haack, Jonatan Bohr Brask, Nicolas Brunner, and Marcus Huber. Unifying Paradigms of Quantum Refrigeration: A Universal and Attainable Bound on Cooling. *Physical Review Letters*, 123(17):170605, October 2019. doi: 10.1103/PhysRevLett.123.170605.

[270] Armin Tavakoli, Géraldine Haack, Nicolas Brunner, and Jonatan Bohr Brask. Autonomous multipartite entanglement engines. *Physical Review A*, 101(1):012315, January 2020. doi: 10.1103/PhysRevA.101.012315.

[271] Antoine Rignon-Bret, Giacomo Guarnieri, John Goold, and Mark T. Mitchison. Thermodynamics of precision in quantum nano-machines. *arXiv:2009.11303 [cond-mat, physics:quant-ph]*, November 2020.

[272] Bibek Bhandari, Paolo Andrea Erdman, Rosario Fazio, Elisabetta Paladino, and Fabio Taddei. Thermal rectification through a multi-level quantum system. *arXiv:2101.10732 [cond-mat, physics:quant-ph]*, January 2021.

[273] Kang Hao Lee, Vinitha Balachandran, and Dario Poletti. Giant rectification in segmented, strongly interacting, spin chains despite the presence of perturbations. *arXiv:2103.06750 [cond-mat]*, March 2021.

[274] Steven J. Weber, Gabriel O. Samach, David Hover, Simon Gustavsson, David K. Kim, Alexander Melville, Danna Rosenberg, Adam P. Sears, Fei Yan, Jonilyn L. Yoder, William D. Oliver, and Andrew J. Kerman. Coherent Coupled Qubits for Quantum Annealing. *Physical Review Applied*, 8(1):014004, July 2017. doi: 10.1103/PhysRevApplied.8.014004.

[275] T. P. Orlando, J. E. Mooij, Lin Tian, Caspar H. van der Wal, L. S. Levitov, Seth Lloyd, and J. J. Mazo. Superconducting persistent-current qubit. *Physical Review B*, 60(22):15398–15413, December 1999. ISSN 0163-1829, 1095-3795. doi: 10.1103/PhysRevB.60.15398.

[276] Markus J. Storcz and Frank K. Wilhelm. Decoherence and gate performance of coupled solid-state qubits. *Physical Review A*, 67(4):042319, April 2003. ISSN 1050-2947, 1094-1622. doi: 10.1103/PhysRevA.67.042319.

[277] F. K. Wilhelm, M. J. Storcz, C. H. van der Wal, C. J. P. M. Harmans, and J. E. Mooij. Decoherence of Flux Qubits Coupled to Electronic Circuits. *arXiv:cond-mat/0305349*, 43:763–780, July 2003. doi: 10.1007/978-3-540-44838-9_54.

[278] John M. Martinis, S. Nam, J. Aumentado, K. M. Lang, and C. Urbina. Decoherence of a superconducting qubit due to bias noise. *Physical Review B*, 67(9):094510, March 2003. ISSN 0163-1829, 1095-3795. doi: 10.1103/PhysRevB.67.094510.

[279] Heinz-Peter Breuer and Francesco Petruccione. *The Theory of Open Quantum Systems*. Oxford University Press, January 2007. ISBN 978-0-19-921390-0. doi: 10.1093/acprof:oso/9780199213900.001.0001.

[280] Karl Blum. *Density Matrix Theory and Applications*. Springer Series on Atomic, Op-

tical, and Plasma Physics. Springer-Verlag, Berlin Heidelberg, third edition, 2012. ISBN 978-3-642-20560-6. doi: 10.1007/978-3-642-20561-3.

[281] Patrick P. Hofer, Martí Perarnau-Llobet, L. David M. Miranda, Géraldine Haack, Ralph Silva, Jonatan Bohr Brask, and Nicolas Brunner. Markovian master equations for quantum thermal machines: Local versus global approach. *New Journal of Physics*, 19(12):123037, December 2017. ISSN 1367-2630. doi: 10.1088/1367-2630/aa964f.

[282] Mark T. Mitchison and Martin B. Plenio. Non-additive dissipation in open quantum networks out of equilibrium. *New Journal of Physics*, 20(3):033005, March 2018. ISSN 1367-2630. doi: 10.1088/1367-2630/aa9f70.

[283] Marco Cattaneo, Gian Luca Giorgi, Sabrina Maniscalco, and Roberta Zambrini. Local vs global master equation with common and separate baths: Superiority of the global approach in partial secular approximation. *arXiv:1906.08893 [quant-ph]*, September 2020. doi: 10.1088/1367-2630/ab54ac.

[284] Erik Aurell and Federica Montana. Thermal power of heat flow through a qubit. *Physical Review E*, 99(4):042130, April 2019. ISSN 2470-0045, 2470-0053. doi: 10.1103/PhysRevE.99.042130.

[285] Dvira Segal and Abraham Nitzan. Spin-Boson Thermal Rectifier. *Physical Review Letters*, 94(3):034301, January 2005. ISSN 0031-9007, 1079-7114. doi: 10.1103/PhysRevLett.94.034301.

[286] William K. Wootters. Entanglement of Formation of an Arbitrary State of Two Qubits. *Physical Review Letters*, 80(10):2245–2248, March 1998. doi: 10.1103/PhysRevLett.80.2245.

[287] M. Partanen, K. Y. Tan, S. Masuda, J. Govenius, R. E. Lake, M. Jenei, L. Grönberg, J. Hassel, S. Simbierowicz, V. Vesterinen, J. Tuorila, T. Ala-Nissila, and M. Möttönen. Flux-tunable heat sink for quantum electric circuits. *Scientific Reports*, 8(1):6325, April 2018. ISSN 2045-2322. doi: 10.1038/s41598-018-24449-1.

[288] Jani Tuorila, Matti Partanen, Tapio Ala-Nissila, and Mikko Möttönen. Efficient protocol for qubit initialization with a tunable environment. *npj Quantum Information*, 3(1):1–12, July 2017. ISSN 2056-6387. doi: 10.1038/s41534-017-0027-1.